Towards high resolution operando electron microscopy of a working catalyst

Puspitasari, Indra

DOI
10.4233/uuid:30fe9aa3-1250-4470-99b1-6d3990d81bb8

Publication date
2016

Document Version
Final published version

Citation (APA)
Puspitasari, I. (2016). *Towards high resolution operando electron microscopy of a working catalyst*. [Dissertation (TU Delft), Delft University of Technology]. https://doi.org/10.4233/uuid:30fe9aa3-1250-4470-99b1-6d3990d81bb8

Towards high resolution operando electron microscopy of a working catalyst

Proefschrift

ter verkrijging van de graad van doctor
aan de Technische Universiteit Delft,
op gezag van de Rector Magnificus Prof.ir. K.C.A.M. Luyben;
voorzitter van het College voor Promoties,
in het openbaar te verdedigen op
maandag 10 oktober 2016 om 10.00 uur

door
Indra PUSPITASARI
Master of Chemical Engineering
University of Science and Technology, South Korea
geboren te Blitar, Indonesië

This thesis has been approved by the promotores:
Prof. dr. F. Kapteijn
Prof. dr. P.J. Kooyman

Composition of the doctoral committee:

Rector Magnificus	Chairman
Prof. dr. F. Kapteijn	Delft University of Technology, promotor
Prof. dr. P. J. Kooyman	University of Cape Town, promotor
Independent committee:	
Prof. dr. ir. P. M. Sarro	Delft University of Technology
Porf. dr. U. Staufer	Delft University of Technology
Prof. dr. J. W. M. Frenken	Advanced Research Center for Nanolithography / UvA
Prof. dr. J. A. Moulijn	Delft University of Technology
Dr. ir. B. L. M. Hendriksen	FEI Company
Reserve committee member	
Prof. dr. J. Gascon	Delft University of Technology

Keywords: Transmission electron microscopy, in-situ and operando experiments, catalysis.
The work described in this thesis was financially supported by the NIMIC consortium (Nano Imaging under Industrial Conditions).

Printed by: Ipskamp drukkers BV, Enschede
Cover design: I. Puspitasari (TEM images were taken by S. Vendelbo).

ISBN 978-94-028-0322-8
An electronic version of this thesis is available at: http://repository.tudelft.nl

To my beloved family and friends

Table of Contents

1 Introduction

1.1 The study of heterogeneous catalysts

In 1836, the Swedish scientist J.J. Berzelius introduced the word 'catalysis' to the chemical world. Catalysis is a Greek word meaning a breaking down which can be used to describe the phenomenon where the normal barriers of chemical reactions are removed. Then in 1894, a German physical chemist, F.W. Ostwald, gave the modern definition of a catalyst; a substance that increases the rate at which a chemical system approaches equilibrium, without being changed in the process[1]. The first application of catalysis in the industry was the large-scale production of sulphuric acid using platinum catalysts by P. Peregrine in 1875[2]. It was followed by ammonia oxidation on Pt gauze by Ostwald in 1903[3]. The discovery of supported iron for ammonia synthesis by A. Mittasch[4] was the key to the ammonia synthesis process developed by F. Haber and C. Bosch in the period of 1908-1914[5]. In the early 1900s, Germany used catalyst technology to process synthesis gas from natural gas or coal to produce liquid fuels and chemicals. Other developments in catalyst technology included ethanol synthesis using Cu/ZnO in 1923[5,6], catalytic naphta reforming, dehydrogenation and isomerization using Pt/Al_2O_3 in 1950[5,7], exhaust gas emission control and NO reduction using Pt, Pd/Al_2O_3 and Rh/Al_2O_3 in 1976[5,8-10].

After decades of research and development, catalysis products and technology have been applied in many parts of daily life. Taking into account recent catalyst research and publications, C.H. Bartholomew and R.J. Farrauto have outlined some important trends in the development and innovation of catalyst technology[11]:

1. Milder reaction conditions, such as reactions using lower temperatures and pressures.
2. Improved selectivity for the desired products, such as the synthesis of more active and selective catalysts that work at lower temperatures and produce fewer undesirable side reactions.

3. Synthesis of new catalysts, such as enantio-selective catalysts, multifunctional bimetallic catalysts, enzymes, chemzymes[*,12] zeozymes[♣,13] and metal organic frameworks[14].
4. The emergence of new materials, such as new zeolites, new tailored supports and catalysts designed at the nanoscale and even at the molecular level.
5. Greater use of sophisticated tools to study and characterise catalytic materials.
6. Innovations of the reactor design, such as using microchannel- and membrane reactors and more sophisticated modelling methods.

1.2 Fundamental catalysis

The normal barrier that must be overcome in order for a chemical reaction to occur was defined as the activation energy by S. Arrhenius, a Swedish scientist, in 1889[11]. He formulated Arrhenius' law, which states that the reaction rate (r) depends on the collision frequency of the molecules (A) and increases exponentially with activation energy E and the reciprocal temperature times the Boltzmann distribution constant ($R=N_A * k_B$). The law is described with Eq. 1.1.

$$r = Ae^{-(\frac{E}{RT})} \qquad \text{(Eq. 1.1)}$$

The presence of a catalyst will lower the barrier (E_1) by creating an alternative pathway with a lower activation energy (E_2) that is easier to overcome as described in Fig. 1.1.

[*] Chemzymes are artificial enzymes that act like real enzymes.

[♣] Zeozymes are zeolites that mimic the properties of real enzymes.

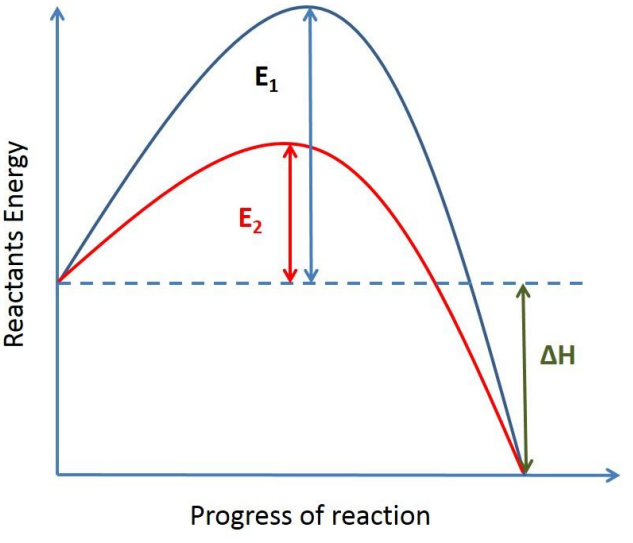

Figure 1.1 Activation energy barriers for a chemical reaction and a catalysed pathway.

Based on its phase, a catalyst can be either homogeneous or heterogeneous. When the catalyst is molecularly dissolved in the same phase as the reactant, the catalyst is called a homogeneous catalyst, e.g., reactions catalysed by dissolved salts, organometallics and enzymes[15-19]. But when the catalyst and reactants have a different phase (solid and gas or liquid), the catalyst is called a heterogeneous catalyst and the reaction is known as a heterogeneously catalysed reaction. The heterogeneous catalyst can be a single metal, alloy or metal oxide, and can also be supported to improve its interfacial area[20-25].

For a heterogeneous catalytic reaction to occur, the reactants have to adsorb on the surface of the catalyst. Then the catalytic conversion occurs, resulting in products that subsequently desorb from the catalyst surface. These steps are known as the elementary reaction steps and the knowledge of these steps is the basis of the Sabatier principle[26]. According to this principle, the interaction of the reactants with the catalyst surface (adsorption strength) must be strong enough to activate the reactants for the reaction to take place, but has to be weak enough for the products to allow them to leave the surface, liberating the sites for further turnovers at that site[27]. Figure 1.2 shows the CO oxidation mechanism as an example of the elementary reaction steps. This reaction has been studied by many scientists using different metal catalysts such as Pt, Pd, Au and Cu[28-34].

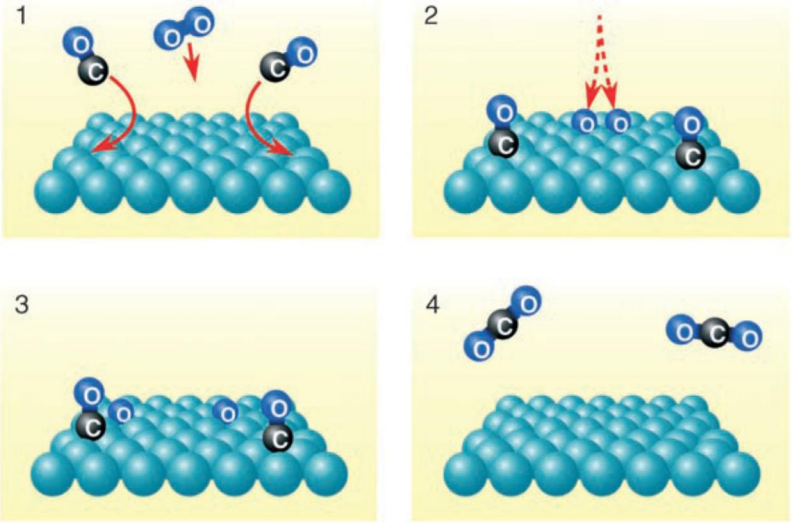

Figure 1.2 The CO oxidation mechanism (reprinted with permission from[34]).

To obtain a high catalytic activity is one of the main goals in catalyst industry, next to selectivity and stability. A common way to describe the catalytic activity is to calculate the Turn Over Frequency (*TOF*). It is the number of times (*n*) that a catalytic reaction occurs per catalytic site per unit time under the given reaction conditions of temperature / pressure / concentration and reactant ratio[35]. Therefore, high concentrations of active surface sites are very important, next to the nature of the active sites.

Another, even more important factor in catalytic reactions is catalyst selectivity. It is a measure of the fraction of converted reactants that ends up in the desired product. The selectivity usually varies with the pressure, temperature, reactant composition, conversion and the nature of the catalyst. The selectivity is not only determined by the catalyst functionality but also by thermodynamic considerations. If reaction conditions are chosen in which the equilibrium concentrations of the side products are negligible, certain undesired products can be avoided. The size and shape of a catalytically active phase are also important factors that affect the reaction selectivity[36-39]. Large PdZn alloy particles exhibit high activity for methanol steam reforming to CO_2 and H_2, while the selectivity to CO is suppressed[40]. In another study G.A. Somorjai et al. concluded that both cyclohexane and cyclohexene were formed on cubo-octahedral nanoparticles, whereas only cyclohexane was produced on cubic nanoparticles[41], a nice example of structure sensitivity in catalysis (vide infra).

A catalyst may lose its activity and selectivity during a catalytic reaction for many reasons such as chemical, thermal and mechanical deactivation[42]. Chemical catalyst deactivation arises from a loss of active sites due to the growth of non-active species, poisoning by certain unwanted foreign species or from carbon / hydrocarbon containing residues from hydrocarbon reactants[43,44] ('fouling'). Thermal catalyst deactivation includes the sintering of a catalytically active species, leading to the loss of active species surface area, or support sintering[45,46]. Mechanical catalyst deactivation includes attrition and crushing[35,47,48].

1.2.1 Catalyst preparation

Catalyst preparation is frequently described as an art to produce a reproducible catalyst and high amount of the desired product. The importance of catalyst preparation triggers scientists to study the effect of each catalyst preparation step[49-52]. From the many catalyst preparation methods, the impregnation method is the easiest and most commonly used. In this method, the catalyst support, usually a porous material, is brought into contact with a solution of one or more metal salts. The following steps are the drying and calcination. The resulting catalyst has active sites that are dispersed over the surface of the support [47,49].

As mentioned before, the conversion rate of reactant molecules to products is related to the number of active sites available on the surface of a catalyst. Therefore, the number of active sites needs to be maximised by dispersing the catalytic species onto a high surface area support. The dispersed catalyst will be present as tiny particles (crystallites) or even as a monolayer, depending on the type of active phase and support. Maximising the catalytic surface area enhances the number of sites per unit mass where chemisorption and catalytic reaction can occur. Most (but not all) commercial catalysts are dispersed on high surface area porous oxides such as Al_2O_3, SiO_2, zeolites, or on high surface area carbons, although these supports may also act as catalysts themselves. Some requirements of a catalyst support are[47]:

1. Good mechanical properties, including attrition resistance, hardness and compressive strength.
2. Stable under reaction conditions.
3. High specific surface area.
4. Porosity, including average pore size and pore size distribution.
5. Low cost.

Considering supported metal catalysts, the metal dispersion is important because usually a higher metal dispersion correlates with higher catalytic activity. The

value of dispersion is defined as the percentage of all metal atoms in the sample that are located at the outside of the metal particle, so exposed to reactants. Chemisorption methods are usually used to determine this value for metals but also Transmission Electron Microscopy (TEM) can give a direct measurement of particle size and particle size distribution which are important to determine the dispersion[35,47].

Correlations between the activity and selectivity of a catalyst with their chemical and physical properties have become an important research subject for scientists. A structure-sensitive catalytic reaction is a reaction in which the activity and selectivity mainly depend on the local metal particle size, and less on the exposed surface area. This is in contrast to a structure-insensitive catalytic reaction, where the activity is primarily dependent on the surface area and less on the structure[53,54]. This concept has stimulated many studies of the activity versus the metal surface structure or metal particle size, and the discovery of a number of structure-sensitive reactions[53,55]. Furthermore, since 1980 the interaction of the support with the active phase has become a major research subject, as these interactions affect the activity and selectivity of the catalyst as well[40,55-57].

1.2.2 Catalyst characterisation

Characterisation of a heterogeneous catalyst refers to the determination of those physical and chemical properties that are assumed relevant for its performance in a catalytic reaction. N_2 adsorption-desorption is used to determine the surface area, pore size and pore volume. In order to determine the elemental composition, Inductively Coupled Plasma-Atomic Emission Spectroscopy (ICP-AES), X-Ray Fluorescence (XRF) and X-ray Photoelectron Spectroscopy (XPS) can be used. Atomic Force Microscopy (AFM), Scanning Electron Microscopy (SEM), Scanning Tunnelling Microscopy (STM), and Transmission Electron Microscopy (TEM) are usually used to study the surface texture, morphology and particle size of the catalyst, while local structure and coordination stoichiometry follow from X-ray Absorption Structure (XAS) Studies. The surface reactivity can be determined by Temperature Programmed Desorption / Reduction / Oxidation (TPD / TPR / TPO), while the surface acidity is usually studied by ammonia TPD, Fourier Transform Infra-Red (FTIR) spectroscopy coupled with CO or pyridine adsorption, and Nuclear Magnetic Resonance (NMR) analysis. Some important reasons to do catalyst characterisation are[11]:

1. Understanding the relationship between physical, chemical and catalytic properties of the catalyst.

2. Elucidating the causes of deactivation, designing procedures for regeneration and choosing the catalyst properties to minimise deactivation.
3. Determining physical and chemical properties for the reactor design, modelling and process optimisation.
4. Ensuring quality control in catalyst manufacturing.

In temperature programmed techniques, a process is monitored while the temperature is increased linearly in time. The basis of these techniques consists of a reactor containing the sample and thermal conductivity detector (TCD) or flame ionisation detector (FID) or even a mass spectrometer to measure the hydrogen content in TPR/TPD or the oxygen in TPO of the gas mixture before and after reaction. TPR gives useful quantitative fingerprint information on the metal oxide catalyst phase that formed after catalyst preparation and on the temperature of reduction. Although revealing less information on the structure of the metal oxide catalyst, results obtained from TPR complement data obtained from spectroscopic methods.

Infrared spectroscopy is one of the non-destructive catalyst characterisation techniques. Its most common applications are to identify adsorbed species and to study the way in which these species are chemisorbed on the surface of the catalyst[26]. The basic principle of this technique is that when an infrared photon (wave number: 4000-400 cm^{-1}) irradiates a molecule, only certain specific frequencies that match with the vibration energy of the molecule are absorbed. The structure (bond lengths, symmetry) and composition of the molecule are the determining factors, therefore each molecule has its unique infrared absorption spectrum that may be used as a "fingerprint" for identification. For example, the C-O stretch vibration is at 1300-1000 cm^{-1} and the N-H vibration is at 3500-3400 cm^{-1}. Modern infrared spectroscopy techniques use an interferometer and beam splitter to produce interferograms that are converted into a frequency spectrum by Fourier transformation, all contained in a Fourier Transform Infrared (FTIR) spectrometer[58].

Transmission Electron Microscopy, TEM, the topical technique of this thesis, is a powerful and versatile technique to study the structure and chemistry of a heterogeneous catalyst at the atomic scale. The catalyst characterisation is usually performed before and after reaction, and results of this ex-situ analysis are compared. Obviously, these results are often not providing satisfactory pictures of the processes the catalyst undergoes during reaction. Therefore, recent developments in TEM target visualisation of the dynamic changes in catalyst structure at the atomic level as well as measuring its composition[59-61].

Although the size, shape and detailed surface structure of the catalyst nanoparticles can be controlled during synthesis, there is no guarantee that such materials remain stable when exposed to the reaction conditions. The gas used in the reaction can induce a sudden change in the catalyst surface and interface energy, and also drive restructuring of the nanoparticles[62]. In order to understand these phenomena, a lot of research has been conducted to study different types of catalytic reactions using catalyst characterisation instruments. TPR and Ultraviolet Visible (UV-VIS) spectroscopy were used to study the reduction, adsorption and re-dispersion of platinum catalysts. Based on the results, reaction pathways of supported Pt species in oxygen and hydrogen at different temperatures can be described[63-66]. In-situ FTIR spectroscopy has also been used to study many metal oxide catalytic reactions[23,51,67-69]. Environmental TEM (ETEM) has been used to study the sintering process of Pt/Al_2O_3, Pd/Al_2O_3 during catalyst regeneration[46,70], reduction of Cu/ZnO[71] and dynamic morphological changes of Au nanoparticles under H_2 and O_2 cycling[72,73] .

Another approach to study the catalytic reaction mechanism is quasi in-situ TEM[74,75]. This method is a combination of the ex-situ catalytic reaction and TEM measurement. In between, the TEM sample is kept in an inert gas (for example in pure Ar or N_2 environment) to prevent changes in the sample that are triggered by reaction with air or other gases. Details of this method will be discussed in Chapter 6.

1.3 History of Transmission Electron Microscopy (TEM)

In the early 20th century, physicists discovered that accelerated electrons behave in a vacuum just like light. This inspired E. Ruska and M. Knoll to build the first electron microscope. After years of dedication to electron microscopy, Ruska received the Nobel Prize in Physics in 1986[76].

When a beam of high-energy electrons passes through a thin material, it interacts with the specimen. Complex electron waves are formed as the interactions generate elastic scattering and a variety of other signals which can be used to obtain structural and chemical information about the specimen (Fig. 1.3)[77]. Elastic scattering occurs when incident electrons are scattered (deflected from their original path) by atoms in the specimen with no loss of energy (elastic mode). Since all electrons follow Bragg's law (Eq. 1.2), where λ is the wavelength, d is the space between atoms in the specimen and θ is the angle of scattering, and all have the same energy (wavelength), all electrons that are elastically scattered by the same atomic spacing will be scattered with the same angle. These scattered electrons can be collated using magnetic lenses to form a pattern of spots where

each spot belongs to a specific atomic spacing (a plane). This pattern can give information about the orientation, crystal planes and phases present in the examined area.

$$\lambda=2d\sin\theta \qquad \text{(Eq. 1.2)}$$

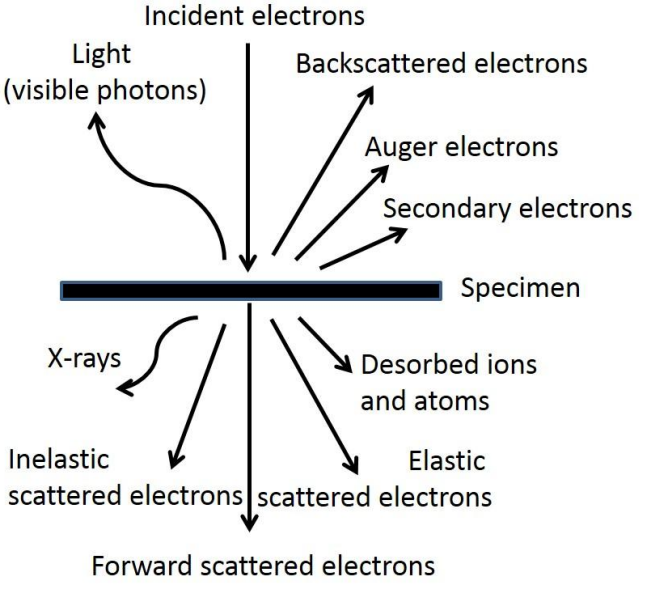

Figure 1.3. Signals generated during electron beam-sample interactions.

Inelastic scattering occurs when incident electrons interact with specimen atoms in an inelastic way (losing energy during interaction). These types of electrons can be used to measure Electron Energy Loss Spectroscopy (EELS) and Kikuchi lines. The inelastic loss of energy is unique to each bonding state of each element. Therefore, it can be used to show both compositional and bonding (e.g. oxidation state) information of the specimen. Kikuchi lines are alternating light and dark lines that are formed by inelastically scattering electrons. These lines can either be measured (their width is inversely proportional to atomic spacing) or followed as a roadmap to the real elastically scattered electron diffraction pattern (the pattern which is described in the previous paragraph).

A schematic representation of the imaging system of a TEM is shown in Fig. 1.4. The equipment inside the electron microscope is divided as: (1) electron gun, (2) vacuum system, (3) specimen stage, (4) electron lens and (5) apertures[78].

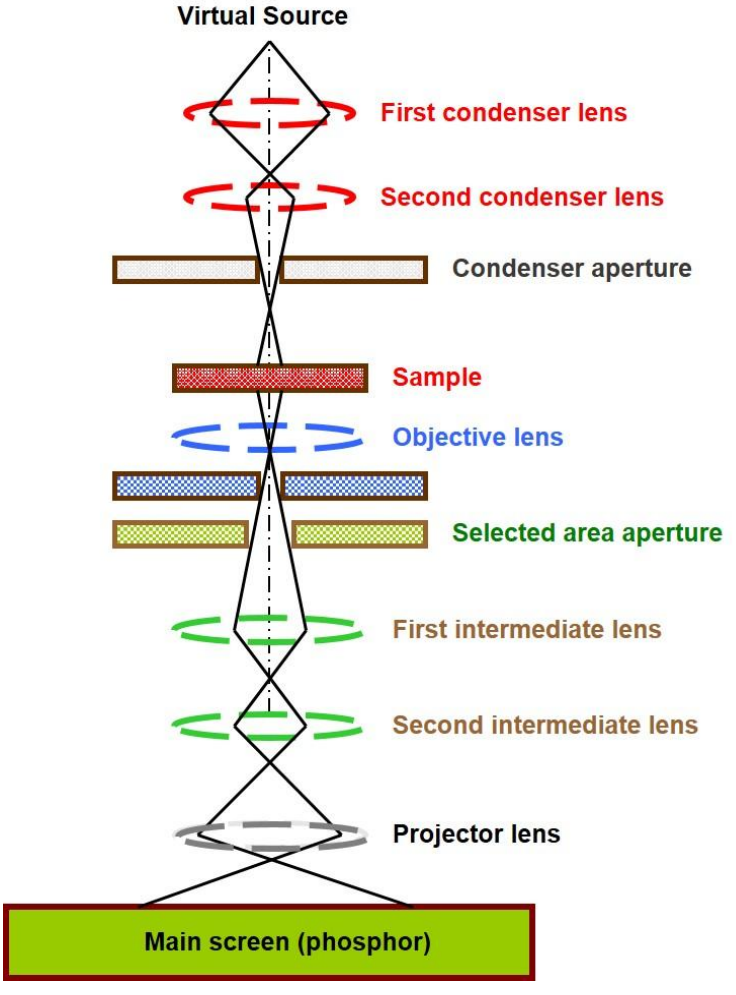

Figure 1.4. Schematic representation of the imaging system of a TEM.

1.3.1 Electron gun

The function of the electron gun is to produce an intense beam of high-energy electrons. Located at the top of the microscope, there are two types of TEM electron source; thermionic electron guns and Field Emission Guns (FEGs). In thermionic electron guns, electrons are emitted from a heated filament and accelerated towards an anode. The filament is a tungsten (W) or LaB_6 single crystal. FEGs are being commonly used because they produce smaller diameter

and more coherent beams than thermionic electron guns. Therefore, FEGs give higher resolution images than thermionic electron guns, but they require better vacuum.

1.3.2 Vacuum system

The column inside a TEM is in a vacuum (usually below 10^{-4} Pa), in order to allow the voltage difference between the cathode and ground without generating an arc and to reduce the collision frequency of electrons with gas atoms. The TEM is not permanently vacuum sealed: the specimen holder which is frequently inserted into (or removed from) the TEM requires an airlock sample holder introduction system with the ability to re-evacuate on a regular basis. To trap any gases that have entered from outside into the vacuum system despite the precaution of an airlock, a cold trap is often placed around the specimen stage. The TEM gun is isolated from the main chamber either by use of gate valves or by differential pumping apertures. These apertures are small holes that prevent diffusion of gas molecules into the gun area.

1.3.3 Specimen stage

There are several kinds of TEM holders. Their usage depends on the purpose of the experiment. Single tilt holders are used to do imaging and diffraction. These can be tilted around the axis of the rod. Double tilt holders give flexibility in orienting the specimen and are very useful for imaging and diffraction studies of crystalline materials. They allow tilting the specimen in two orthogonal directions. Tomography holders allow up to 80^{o} tilt which is very useful to create 3D imaging of the sample[78,79]. Other types of TEM holders are heating holders, cooling holders and protective atmosphere transfer holders. An example of a heating holder is a holder with a molybdenum tip, which allows temperature observation of up to 800 ^{o}C. One type of cooling holders uses liquid nitrogen (boiling point -195.8 ^{o}C) and the other uses liquid helium (boiling point -268.94 ^{o}C)[76]. The protective atmosphere transfer holder prevents specimen contact with air during TEM sample preparation and transfer to the TEM. The holder has a moveable cap that can be opened and closed in the desired gas condition[80].

1.3.4 Electron lenses

A TEM also consists of four main magnetic lenses: condenser lens, objective lens, intermediate lens and projection lens. The magnetic lenses consist of electromagnetic coils that generate convex lenses. These lenses are focusing the parallel beams at some constant focal length. The condenser lens focuses the electron beam into a thin and coherent beam, while the objective lens focuses the transmitted electron beam into an image. The intermediate and projector lenses magnify the initial image that is formed by the objective lens.

1.3.5 Apertures

The electrons that are further away from the optical axis than a fixed distance are excluded by an aperture. Several apertures are placed inside the TEM. The condenser apertures are positioned in the back focal plane of the objective lens (objective aperture), where parallel rays coming from the specimen are focused in one point. The apertures can be used to allow either the central beam or a specific scattered beam to pass through. Another is positioned at the first image plane (between the objective lens and the intermediate lens). With this aperture, scattered electrons can be selected to do Selected Area Electron Diffraction (SAED).

1.4 History of in-situ TEM

1.4.1 Controlled Atmosphere Electron Microscope (CAEM)

The importance of information about real time changes of a catalytic reaction in the electron microscope has stimulated scientists to develop in-situ environmental transmission electron microscopy (ETEM). As pioneers of this system, R.T.K. Baker and co-workers at EXXON Research and Engineering Co. introduced the Controlled Atmosphere Electron Microscope (CAEM) into the JEOL microscope since this is the only series of low voltage TEM with a specimen chamber sufficiently large to accommodate the gas reaction cell. The gas reaction cell was inserted into the microscope in such a way that the inlet of the gas tube can be connected properly[81]. Low voltage TEM was used to prevent the knock on damage on the sample due to the high intensity electron beam while still obtaining high contrast images of the sample.

Figure 1.5 shows the schematic representation of CAEM. In this system, a three-stage diffusion pump backed by a rotary pump surrounds the specimen chamber. The normal pumping port to the microscope vacuum system is blanked off at A (dashed line). An aperture at B restricts gas leakage to the illumination system. The central area of the electron beam passes through a 20 mm diameter hole cut in the centre of the fluorescent viewing screen (C) and strikes a secondary screen (D) with a transmission phosphor. An auxiliary shutter (E) is important to protect the camera during alignment of the microscope. A glove box has been adapted to fit the entry port of the microscope to load the specimens into the microscope in argon atmosphere, so that the specimen will not be exposed to air and water vapour.

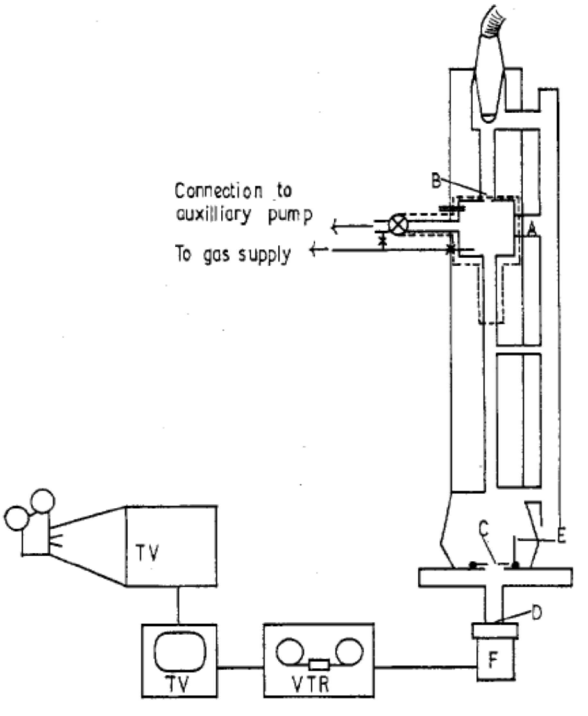

Figure 1.5. Schematic representation of the CAEM (reprinted with permission from[81]) .

The advantages of this system allowed the specimen to be viewed at pressure up to 33 mbar, instead of vacuum condition, and to be heated up to 1200 °C. The disadvantages of the system were low resolution imaging due to the gas

environment and major modifications on the microscope as well as requiring an additional glove box. Therefore, the microscope was dedicated only for gas reaction studies.

1.4.2 Environmental Cell (E-CELL) TEM

Gai and co-workers at DuPont Company presented the second generation of in-situ TEM using a fully integrated and permanently-mounted environmental cell (E-CELL) system based on multistage differential pumping[82-85]. This system included an E-TEM design with the objective lens pole pieces incorporated in the first stage differential pumping (Fig. 1.6). The second differential pumping stage was located between the condenser aperture (top) and selected area diffraction aperture (bottom). Turbo molecular pumps (TMPs) were connected to the ETEM system to perform differential pumping of the region between the pairs of apertures. The ECELL can stand a gas pressure of up to ~50 mbar and a temperature of up to 1100 ^{o}C. For the experiments, Gai et al. used a Philips CM30 TEM with a LaB_6 electron emission source. Some research to understand the role of gas-surface interaction in nanocluster catalysts has been done using this system[35,83-86].

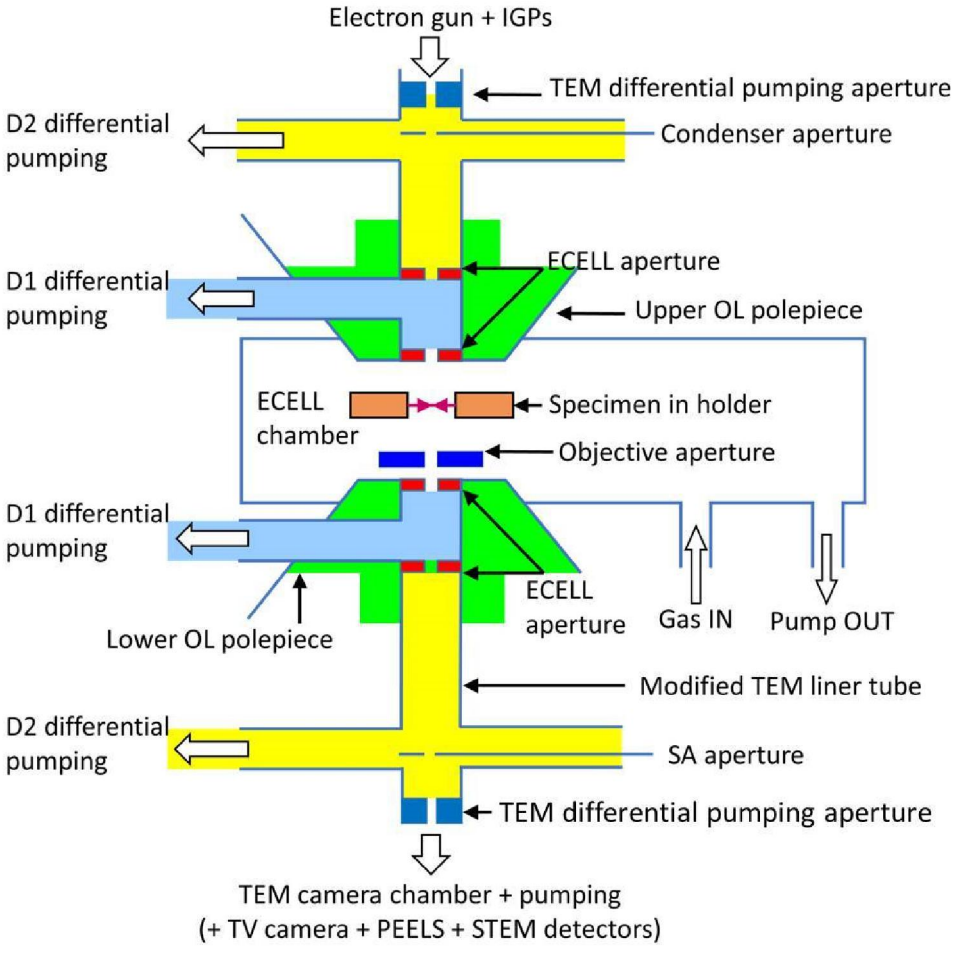

Figure 1.6. Schematic representation of the ETEM (reproduced with permission from [82]).

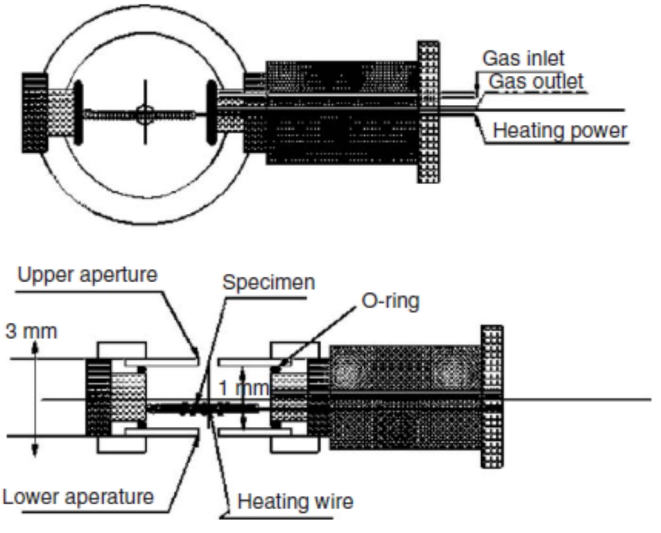

Figure 1.7. ECELL heating holder in top and profile view (reprinted with permission from[73]).

1.4.3 In-situ TEM holder

Instead of modifying the microscope, the third generation of in-situ TEM only modifies the TEM holder. S. Giorgio and co-workers combined an E-CELL that has been incorporated in the TEM holder with a closed reactor equipped with carbon film windows (Fig. 1.7). The experiments were conducted on a JEOL TEM 3010 at 300 kV. The sealing of the cell was provided by Viton O-rings that had been tested in ex-situ mode for leakages at pressures of up to 200 mbar prior to the experiments. The system has been used to do in-situ TEM experiments at temperatures up to 350 ^{o}C and pressures up to 10 mbar. Turbo molecular pumps were used to pump the gas into the cell. They studied the structure-activity relations of Au supported on different materials, such as TiO_2 and amorphous carbon. The samples were observed in vacuum, then in the gas cycle of H_2 and O_2. During the gas cycle, the images showed reversible change from faceted Au nanoparticles in H_2 to a more spherical shape during O_2 exposure. They concluded that the shape changes were driven by the adsorption of gas (O_2 and H_2) on the Au surface[72,73].

A different approach towards in-situ TEM was introduced by H. Saka and co-workers. They developed an environmental TEM holder that had a gas injection nozzle close to the specimen-heater (Fig. 1.8). The experiments were performed

on a Hitachi H-9500 TEM (300kV). The gas injection nozzle permitted gas to flow around the specimen that was located on top of the heating element made from tungsten. The pressure in the specimen chamber was maintained above 10^{-4} mbar while the pressure in the electron gun chamber was kept at around $2x10^{-6}$ mbar using a differential pumping system. Using this system, a temperature of up to 1200 ^{o}C could be reached to study the oxidation of In into InO_3 and the reduction-oxidation cycle of Si into SiO_2[87-90].

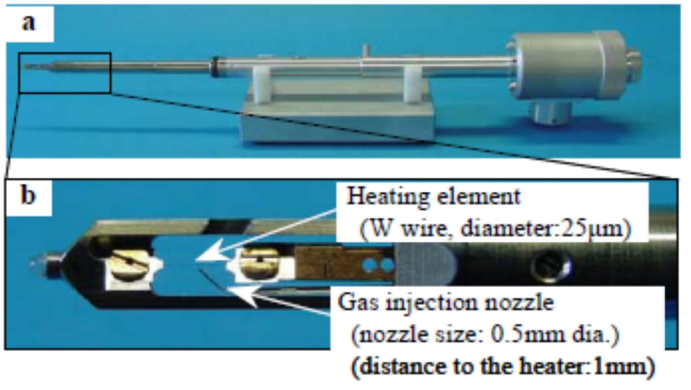

Figure 1.8. (a) Specimen holder, whole image and (b) detail of the tip (reprinted with permission from[87]).

1.4.4 Nanoreactor

A recent development of the in-situ TEM research is using a nanoreactor fabricated by micro-electro-mechanical systems (MEMS) technology, in conjunction with a specially designed TEM specimen holder. The nanoreactor is functionalised with a micrometer-sized gas-flow channel, electron transparent windows and a heating device[71]. Details of this modification will be discussed in Chapter 2.

1.5 Objectives and outline of the thesis

In-situ TEM is a powerful tool to explore gas-solid reactions and catalysts at the atomic level under reaction conditions. But since TEM only works under vacuum conditions, special equipment is needed to perform in-situ TEM experiments under safe and reliable conditions. The equipment should be able to withstand high pressure and high temperature, and at the same time have a good

electron transparency while not leading to contamination. The equipment further requires atomic resolution, easy handling and cost effectiveness. The objectives of this thesis are to address these challenges and to introduce and demonstrate a new generation of in-situ TEM equipment. Basically, the equipment consists of a nanoreactor, a TEM holder and a gas system. The experimental results will provide valuable visual in-situ information to investigate the mechanism of a catalytic reaction and the behaviour of the catalyst under reaction conditions.

The introduction of heterogeneous catalysis, TEM and the history of in-situ TEM are presented in this Chapter 1. Chapter 2 gives an overview of the experimental details and the equipment used in the in-situ TEM experiments. This includes the TEM holder, the gas system, and the nanoreactor design and fabrication. Experimental details of the ex-situ and quasi in-situ TEM experiments are included as sub-chapters in Chapter 5 and 6 respectively. As the electron beam is highly energetic it may also affect the sample on the grid and other species present. The effect of the electron beam during the experiment is studied in Chapter 3. The in-situ cell is based on two windows with the controlled atmosphere in between. To keep the influence of the gas atmosphere as small as possible, the distance between these windows is kept in the order of magnitude of a few micrometer. This introduces challenges for the introduction of the catalyst sample. Chapter 4 focuses on the issue of loading the nanoreactor and presents a method to investigate the loading procedure.

During the project, several studies have been carried out on catalytic reactions performed in ex-situ, quasi in-situ and in-situ TEM mode. Capping agent removal from Au nanoparticles in the ex-situ TEM mode is discussed in Chapter 5. The reduction of Pt/Al_2O_3 and Pd/Al_2O_3 catalysts in the quasi in-situ TEM mode are described in Chapter 6. In Chapter 7 the CO oxidation by Pt nanoparticles is analysed in-situ. The thesis concludes with a summary and evaluation of the work presented.

1.6 References

1 Bond, G. C., Louis, C. & Thompson, D. T. *Catalysis by Gold*. (Imperial College Press, 2006). ISBN: 978-1860946585

2 Cook, E. Peregrine Phillips, the Inventor of the Contact Process for Sulphuric Acid. *Nature* **117**, 419, (1926).

3 Ostwald, W. Improvements in the Manufacture of Nitric Acid and Nitrogen Oxides. *UK Patent 190200698*, (1903).

4 Mittasch, A. & Frankenburg, W. Early Studies of Multicomponent Catalysts. *Adv. Catal.* **2**, 81-104, (1950).

5 Davis, B. H. & Hettinger, W. P. Heterogeneous Catalysis: Selected American Histories **222**, 200, (1983).
6 Taylor, H. S. & Kistiakowsky, G. B. Studies of methanol catalysts. I. *JACS* **49**, 2468-2476, (1927).
7 Haensel, V. & Ipatieff, V. N. Selective demethylation of paraffin hydrocarbons [4]. *JACS* **68**, 345-346, (1946).
8 Hightower, J. W. Catalysts for Automobile Emission Control. *Stud. Surf. Sci. Catal.* **1**, 615-636, (1976).
9 Mantell, D. A., Ryali, S. B. & Haller, G. L. Time-resolved infrared emission studies of CO_2 formed by CO oxidation on Pt and Pd. *Chem. Phys. Lett.* **102**, 37-40, (1983).
10 Kummer, J. T. Use of noble metals in automobile exhaust catalysts. *J. Phys. Chem.* **90**, 4747-4752, (1986).
11 Bartholomew, C. H. & Farrauto, R. J. *Fundamentals of Industrial Catalytic Process*. 2nd edn., (John Wiley and Sons. Inc, 2006). ISBN: 978-0-471-45713-8.
12 Bjerre, J., Rousseau, C., Marinescu, L. & Bols, M. Artificial enzymes, "Chemzymes": Current state and perspectives. *Appl. Micro. Biotech.* **81**, 1-11, (2008).
13 Xuereb, D. J., Dzierzak, J. & Raja, R. From zeozymes to bio-inspired heterogeneous solids: Evolution of design strategies for sustainable catalysis. *Catal. Today* **198**, 19-34, (2012).
14 Gascon, J., Corma, A., Kapteijn, F. & Llabrés I Xamena, F. X. Metal organic framework catalysis: Quo vadis? *ACS Catal.* **4**, 361-378, (2014).
15 Smutny, E. J. Oligomerization and dimerization of butadiene under homogeneous catalysis. Reaction with nucleophiles and the synthesis of 1,3,7-octatriene. *JACS* **89**, 6793-6794, (1967).
16 Laine, R. M., Rinker, R. G. & Ford, P. C. Homogeneous catalysis by ruthenium carbonyl in alkaline solution: the water gas shift reaction. *JACS* **99**, 252-253, (1977).
17 Hill, C. L. & Prosser-McCartha, C. M. Homogeneous catalysis by transition metal oxygen anion clusters. *Coord. Chem. Rev.* **143**, 407-455, (1995).
18 Jessop, P. G., Hsiao, Y., Ikariya, T. & Noyori, R. Homogeneous Catalysis in Supercritical Fluids: Hydrogenation of Supercritical Carbon Dioxide to Formic Acid, Alkyl Formates, and Formamides. *JACS* **118**, 344-355, (1996).
19 Odenkirk, W., Rheingold, A. L. & Bosnich, B. Homogeneous catalysis: a ruthenium-based Lewis-acid catalyst for the Diels-Alder reaction. *JACS* **114**, 6392-6398, (1992).
20 Baylet, A., Capdeillayre, C., Retailleau, L., Valverde, J. L., Vernoux, P. & Giroir-Fendler, A. Parametric study of propene oxidation over Pt and Au

catalysts supported on sulphated and unsulphated titania. *Appl. Catal. B: Environ.* **102**, 180-189, (2011).

21 Rekkab-Hammoumraoui, I., Choukchou-Braham, A., Pirault-Roy, L. & Kappenstein, C. Catalytic oxidation of cyclohexane to cyclohexanone and cyclohexanol by tert-butyl hydroperoxide over Pt/oxide catalysts. *Mater. Sci.* **34**, 1127-1135, (2011).

22 Newton, M. A., Belver-Coldeira, C., Martanez-Arias, A. & Fernandez-Garcaa, M. Dynamic in situ observation of rapid size and shape change of supported Pd nanoparticles during CO/NO cycling. *Nature Mater.* **6**, 528-532, (2007).

23 Almeida, A. R., Moulijn, J. A. & Mul, G. In situ ATR-FTIR study on the selective photo-oxidation of cyclohexane over anatase TiO_2. *J. Phys. Chem. C* **112**, 1552-1561, (2008).

24 Behrens, M., Studt, F., Kasatkin, I., Kühl, S., Hävecker, M., Abild-Pedersen, F., Zander, S., Girgsdies, F., Kurr, P., Kniep, B. L., Tovar, M., Fischer, R. W., Nørskov, J. K. & Schlögl, R. The active site of methanol synthesis over $Cu/ZnO/Al_2O_3$ industrial catalysts. *Science* **336**, 893-897, (2012).

25 Razali, N. A. M., Lee, K. T., Bhatia, S. & Mohamed, A. R. Heterogeneous catalysts for production of chemicals using carbon dioxide as raw material: A review. *Renew. Sustain. Energy Rev.* **16**, 4951-4964, (2012).

26 Santen, R. A. v., Leeuwen, P. W. N. M. v., Moulijn, J. A and Averill, B. A. *Catalysis: An Integrated Approach*. 2nd edn., (Elsevier, 2000), ISBN: 9780444829634

27 Santen, R. A. v. in *Novel Concepts in Catalysis and Chemical Reactors* (ed. Moulijn J. A., Cybulski A., Stankiewicz A.) Ch. 1, (Willey-VCH, 2010). ISBN: 9783527324699

28 Ackermann, M. D., Pedersen, T. M., Hendriksen, B. L. M., Robach, O., Bobaru, S. C., Popa, I., Quiros, C., Kim, H., Hammer, B., Ferrer, S. & Frenken, J. W. M. Structure and reactivity of surface oxides on Pt(110) during catalytic CO oxidation. *Phys. Rev. Lett.* **95**, 1-4, (2005).

29 Ivanova, A. S., Slavinskaya, E. M., Gulyaev, R. V., Zaikovskii, V. I., Stonkus, O. A., Danilova, I. G., Plyasova, L. M., Polukhina, I. A. & Boronin, A. I. Metal-support interactions in Pt/Al_2O_3 and Pd/Al_2O_3 catalysts for CO oxidation. *Appl. Catal. B: Environmental* **97**, 57-71.

30 Zou, X., Qi, S., Xu, J., Suo, Z., An, L. & Li, F. Study on Au/Al_2O_3 catalysts for low-temperature CO oxidation in situ FT-IR. *J. Nat. Gas Chem.* **19**, 307-312, (2010).

31 Davran-Candan, T., Tezcanli, S. T. & Yildirim, R. Selective CO oxidation over promoted $Au/\gamma\text{-}Al_2O_3$ catalysts in the presence of CO_2 and H_2O in the feed. *Catal. Commun.* **12**, 1149-1152, (2011).

32 Goldstein, E. A. & Mitchell, R. E., Chemical kinetics of copper oxide reduction with carbon monooxide, in *P. Combust. Inst.* 2nd edn. (Elsevier, 2011), 2803-2810, ISSN: 1540-7489
33 Song, E. H., Wen, Z. & Jiang, Q. CO catalytic oxidation on copper-embedded graphene. *J. Phys. Chem. C* **115**, 3678-3683, (2011).
34 Ertl, G. Reactions at surfaces: From atoms to complexity (Nobel Lecture). *Angew. Chem. - Int. Ed.* **47**, 3524-3535, (2008).
35 Gai, P. & Boyes, E. D. *Electron Microscopy in Heterogeneous Catalysis*. (IOP Publishing, 2003). ISBN: 0750308095
36 Somorjai, G. A. & Park, J. Y. Molecular factors of catalytic selectivity. *Ang. Chem. - Int. Ed.* **47**, 9212-9228, (2008).
37 Narayanan, R. & El-Sayed, M. A. Shape-dependent catalytic activity of platinum nanoparticles in colloidal solution. *Nano Lett.* **4**, 1343-1348, (2004).
38 Lee, I., Morales, R., Albiter, M. A. & Zaera, F. Synthesis of heterogeneous catalysts with well shaped platinum particles to control reaction selectivity. *PNAS* **105**, 15241-15246, (2008).
39 Tao, A. R., Habas, S. & Yang, P. Shape control of colloidal metal nanocrystals. *Small* **4**, 310-325, (2008).
40 Dagle, R. A., Chin, Y. H. & Wang, Y. The effects of PdZn crystallite size on methanol steam reforming. *Topics in Catalysis* **46**, 358-362, (2007).
41 Bratlie, K. M., Lee, H., Komvopoulos, K., Yang, P. & Somorjai, G. A. Platinum nanoparticle shape effects on benzene hydrogenation selectivity. *Nano Lett.* **7**, 3097-3101, (2007).
42 Moulijn, J. A., van Diepen, A. E. & Kapteijn, F. Catalyst deactivation: is it predictable?: What to do? *Appl. Catal. A* **212**, 3-16, (2001).
43 Quintanilla, A., Butselaar-Orthlieb, V. C. L., Kwakernaak, C., Sloof, W. G., Kreutzer, M. T. & Kapteijn, F. Weakly bound capping agents on gold nanoparticles in catalysis: Surface poison? *J. Catal.* **271**, 104-114, (2010).
44 Halevi, B., Peterson, E. J., Roy, A., Delariva, A., Jeroro, E., Gao, F., Wang, Y., Vohs, J. M., Kiefer, B., Kunkes, E., Hävecker, M., Behrens, M., Schlögl, R. & Datye, A. K. Catalytic reactivity of face centered cubic PdZn α for the steam reforming of methanol. *J. Catal.* **291**, 44-54, (2012).
45 Cabello Galisteo, F., Mariscal, R., López Granados, M., Fierro, J. L. G., Daley, R. A. & Anderson, J. A. Reactivation of sintered Pt/Al_2O_3 oxidation catalysts. *Appl. Catal. B: Environmental* **59**, 227-233, (2005).
46 Liu, R. J., Crozier, P. A., Smith, C. M., Hucul, D. A., Blackson, J. & Salaita, G. In Situ Electron Microscopy Studies of the Sintering of Palladium Nanoparticles on Alumina during Catalyst Regeneration Processes. *Microsc. Microanal.* **10**, 77-85, (2004).

47 Satterfield, C. N. *Heterogeneous Catalysis in Practice*. (McGraw-Hill, 1980). ISBN: 9780070548756.
48 Bartholomew, C. H. Mechanisms of catalyst deactivation. *Appl. Catal. A* **212**, 17-60, (2001).
49 Bass, R. J., Dunn, T. M., Lin, Y. C. & Hohn, K. L. Syngas production from catalytic partial oxidation of n-butane: Comparison between incipient wetness and sol-gel prepared Pt/Al_2O_3. *Ind. Eng. Chem. Res.* **47**, 7184-7189, (2008).
50 Chin, Y.-H., Wang, Y., Dagle, R. A. & Shari Li, X. Methanol steam reforming over Pd/ZnO: Catalyst preparation and pretreatment studies. *Fuel Process Technol.* **83**, 193-201, (2003).
51 Ebbesen, S. D., Mojet, B. L. & Lefferts, L. In situ ATR-IR study of CO adsorption and oxidation over Pt/Al_2O_3 in gas and aqueous phase: Promotion effects by water and pH. *J. Catal.* **246**, 66-73, (2007).
52 Menard, L. D., Xu, F., Nuzzo, R. G. & Yang, J. C. Preparation of TiO_2-supported Au nanoparticle catalysts from a Au_{13} cluster precursor: Ligand removal using ozone exposure versus a rapid thermal treatment. *J. Catal.* **243**, 64-73, (2006).
53 Somorjai, G. A. & Carrazza, J. Structure sensitivity of catalytic reactions. *Ind. Eng. Chem. Fund.* **25**, 63-69, (1986).
54 Boudart, M. Catalysis by Supported Metals. *Adv. Catal.* **20**, 153-166, (1969).
55 Taghavi, M. B., Pajonk, G. M. & Teichner, S. J. On the structure-sensitive and structure-insensitive catalytic reactions and their new characteristics, demonstrated with copper-supported catalysts. *J. Coll. Interf. Sci.* **71**, 451-465, (1979).
56 Joyner, R. W., Pendry, J. B., Saldin, D. K. & Tennison, S. R. Metal-support interactions in heterogeneous catalysis. *Surf. Sci.* **138**, 84-94, (1984).
57 Subramanian, S. & Schwarz, J. A. Effect of support microporosity and preparation conditions on the reducibility of Pt/Al_2O_3 catalysts. *Appl. Catal.* **61**, L15-L19, (1990).
58 Larkin, P. J. *IR and Raman Spectroscopy: Principles and Spectral Interpretation*. (Elsevier, 2011). ISBN: 978-0123869845
59 Chenna, S. & Crozier, P. A. In situ environmental transmission electron microscopy to determine transformation pathways in supported Ni nanoparticles. *Micron* **43**, 1188-1194, (2012).
60 Crozier, P. A., Wang, R. & Sharma, R. In situ environmental TEM studies of dynamic changes in cerium-based oxides nanoparticles during redox processes. *Ultramicroscopy* **108**, 1432-1440, (2008).
61 Creemer, J. F., Helveg, S., Kooyman, P. J., Molenbroek, A. M., Zandbergen, H. W. & Sarro, P. M. A MEMS reactor for atomic-scale

microscopy of nanomaterials under industrially relevant conditions. *J. Microelectromech. Syst.* **19**, 254-264, (2010).
62 Ertl, G. *Reactions at Solid Surface*. (John Willey & Sons, Inc., 2009). ISBN: 978-0-470-26101-9.
63 Lietz, G., Lieske, H., Spindler, H., Hanke, W. & Völter, J. Reactions of platinum in oxygen- and hydrogen-treated Pt/γ-Al_2O_3 catalysts: II. Ultraviolet-visible studies, sintering of platinum, and soluble platinum. *J. Catal.* **81**, 17-25, (1983).
64 Fiedorow, R. M. J. & Wanke, S. E. The sintering of supported metal catalysts: I. Redispersion of supported platinum in oxygen. *J. Catal.* **43**, 34-42, (1976).
65 Lieske, H., Lietz, G., Spindler, H. & Völter, J. Reactions of platinum in oxygen- and hydrogen-treated Pt/y-Al_2O_3 catalysts: I. Temperature-programmed reduction, adsorption, and redispersion of platinum. *J. Catal.* **81**, 8-16, (1983).
66 Niwa, M., Awano, K. & Murakami, Y. Activity of supported platinum catalysts for methane oxidation. *Appl. Catal.* **7**, 317-325, (1983).
67 Ammendola, P., Barbato, P. S., Lisi, L., Ruoppolo, G. & Russo, G. Alumina contribution to CO oxidation: A TPR and IR study. *Surf. Sci.* **605**, 1812-1817, (2011).
68 Ferri, D., Bürgi, T. & Baiker, A. In situ ATR-IR study of the adsorption of cinchonidine on Pd/Al_2O_3: Differences and similarities with adsorption on Pt/Al_2O_3. *J. Catal.* **210**, 160-170, (2002).
69 Ortiz-Hernandez, I. & Williams, C. T. In situ investigation of solid-liquid catalytic interfaces by attenuated total reflection infrared spectroscopy. *Langmuir* **19**, 2956-2962, (2003).
70 Liu, R. J., Crozier, P. A., Smith, C. M., Hucul, D. A., Blackson, J. & Salaita, G. In situ TEM study of sintering in Pd/Al_2O_3 catalysts. *Microsc. Microanal.* **10**, 488-489, (2004).
71 Creemer, J. F., Helveg, S., Hoveling, G. H., Ullmann, S., Molenbroek, A. M., Sarro, P. M. & Zandbergen, H. W. Atomic-scale electron microscopy at ambient pressure. *Ultramicroscopy* **108**, 993-998, (2008).
72 Giorgio, S., Cabie, M. & Henry, C. R. Dynamic observations of Au catalysts by environmental electron microscopy. *Gold Bull.* **41**, 167-173, (2008).
73 Giorgio, S., Sao Joao, S., Nitsche, S., Chaudanson, D., Sitja, G. & Henry, C. R. Environmental electron microscopy (ETEM) for catalysts with a closed E-cell with carbon windows. *Ultramicroscopy* **106**, 503-507, (2006).
74 Reinhoudt, H. R., Van Langeveld, A. D., Kooyman, P. J., Stockmann, R. M., Prins, R., Zandbergen, H. W. & Moulijn, J. A. The evolution of surface species in NiW/Al_2O_3 catalysts in various stages of sulfidation: A quasi in-

situ high resolution transmission electron microscopic investigation. *J. Catal.* **179**, 443-450, (1998).
75 Janbroers, S., Louwen, J. N., Zandbergen, H. W. & Kooyman, P. J. Insights into the nature of iron-based Fischer-Tropsch catalysts from quasi in situ TEM-EELS and XRD. *J. Catal.* **268**, 235-242, (2009).
76 Shindo, D. & Oikawa, T. *Analytical Electron Microscopy for Materials Science*. (Springer, 2002). ISBN: 978-4431703365.
77 Thomas, J. M. & Gai, P. L., Electron Microscopy and the Materials Chemistry of Solid Catalysts, in *Adv. Catal.,* Vol. 48, 171-227, (Academic Press, 2004). ISBN: 0360-0564.
78 William, D. B. & Carter, C. B. *Transmission Electron Microscopy: A textbook for Materials Science*. (Plenum, 1996). ISBN: 9780306452475
79 Gatan, Inc. *TEM Specimen Holders*, http://www.gatan.com/products/specimen_holders/ (consulted date 8-4-2016).
80 Kooyman, P. J., Buglass, J. G., Reinhoudt, H. R., Van Langeveld, A. D., Hensen, E. J. M., Zandbergen, H. W. & Van Veen, J. A. R. Quasi in situ sequential sulfidation of $CoMo/Al_2O_3$ studied using high-resolution electron microscopy. *J. Phys. Chem. B* **106**, 11795-11799, (2002).
81 Baker, R. T. K. & Harris, P. S. Controlled atmosphere electron microscopy. *J. Phys. E.* **5**, 793, (1972).
82 Gai, P. L., Boyes, E. D., Helveg, S., Hansen, P. L., Giorgio, S. & Henry, C. R. Atomic-resolution environmental transmission electron microscopy for probing gas-solid reactions in heterogeneous catalysis. *MRS Bull.* **32**, 1044-1050, (2007).
83 Boyes, E. D., Gai, P. L. & Hanna, L. G. Controlled environment [ECELL] TEM for dynamic in-situ reaction studies with HREM lattice imaging. *Mater. Res. Soc. Symp. Proc.* **404**, 53-60, (1996).
84 Boyes, E. D. & Gai, P. L. Environmental high resolution electron microscopy and applications to chemical science. *Ultramicroscopy* **67**, 219-232, (1997).
85 Gai, P. L. Environmental high resolution electron microscopy of gas-catalyst reactions. *Top. Catal.* **8**, 97-113, (1999).
86 Hansen, P. L., Wagner, J. B., Helveg, S., Rostrup-Nielsen, J. R., Clausen, B. S. & Topsoe, H. Atom-resolved imaging of dynamic shape changes in supported copper nanocrystals. *Science* **295**, 2053-2055, (2002).
87 Kishita, K., Kamino, T., Watabe, A., Kuroda, K. & Saka, H. In situ TEM observation of solid-gas reactions. *JPCS* **126**, (2008).
88 Kamino, T., Yaguchi, T., Konno, M., Watabe, A., Marukawa, T., Mima, T., Kuroda, K., Saka, H., Arai, S., Makino, H., Suzuki, Y. & Kishita, K.

Development of a gas injection/specimen heating holder for use with transmission electron microscope. *J. Electron Microsc.* **54**, 497-503, (2005).
89 Yaguchi, T., Suzuki, M., Watabe, A., Nagakubo, Y., Ueda, K. & Kamino, T. Development of a high temperature-atmospheric pressure environmental cell for high-resolution TEM. *J. Electron Microsc.* **60**, 217-225, (2011).
90 Yaguchi, T., Kanemura, T., Shimizu, T., Imamura, D., Watabe, A. & Kamino, T. Development of a technique for in situ high temperature TEM observation of catalysts in a highly moisturized air atmosphere. *J. Electron Microsc.* **61**, 199-206, (2012).

2 Towards High Pressure In-situ TEM Catalytic studies

Catalyst characterisation is usually done before and after use of the catalyst. Based on these (and other) results, interpretations regarding the reaction mechanism or catalyst performance can be formulated. But the questions regarding what happened to the catalyst during the reaction are still intriguing the scientist. To address these questions, scientists perform in-situ studies using different types of characterisation techniques[1-6]. Depending on the technique, the in-situ study may give valuable information on changes of the catalyst size, structure and morphology while being exposed to the reaction conditions. This may lead to a better understanding of the catalytic action. In the end, the information can suggest what kind of factor(s) should be added and / or eliminated in order to improve the catalytic activity and selectivity[7-9].

TEM is one of the important instruments for catalyst characterisation. TEM operates using high-energy electrons (40-1500 keV) and needs high vacuum conditions (below 10^4 Pa). The vacuum system is important to reduce the collision frequency of the electrons with gas atoms, which will scatter the electron beam and reduce the resolution of the images. Moreover, the electron gun cannot stand high gas pressures. This pressure condition impedes the development of in-situ TEM studies.

Since the gas presence inside the microscope is unwanted, in order to do catalytic reactions where gases are the main components inside the TEM, a special device is needed. The device should comply with several features such as an electron beam transparent membrane, stability under the electron beam, gas tightness, ability to withstand high-pressure gas (catalytic reaction conditions) and being equipped with a heating system.

To address this challenge, the Delft Institute of Microsystems and Nanoelectronics (DIMES), the Kavli Institute for NanoScience and ChemE (all at TU Delft), together developed an in-situ TEM nanoreactor design which fulfils the above requirements and can be easily inserted into (or removed from) a dedicated in-situ TEM holder with additional heating and gas supply systems. This feature is an additional advantage of the design, which allows reproducible experiments. Modification of the TEM itself is not needed with this design, therefore the in-situ TEM holder in combination with a replaceable nanoreactor constitutes a versatile technique.

The oscillatory catalytic CO oxidation by Pt nanoparticles is analysed as the ultimate demonstration application of the complete in-situ TEM system in this project. The results are described in Chapter 7. The hardware details of the system are described in this chapter.

2.1 Transmission Electron Microscope (TEM)

Several different TEM machines have been used in the project (Fig. 2.1), fabricated by FEI. For ex-situ and quasi in-situ experiments we used a TECNAI, which is located at the Kavli Institute for NanoScience, TU Delft. The in-situ experiments are conducted using TITANs. One TITAN machine used is located at the Kavli Institute for NanoScience, TU Delft, The Netherlands, and the other is located at Haldor Topsøe A/S, in Lyngby, Denmark.

2.1.1 TECNAI

The FEI TECNAI TF20 is one of the TECNAI G2 series. The microscope enables atomic resolution TEM imaging, which can reveal sub-Ångstrøm information of a material. This TECNAI is equipped with a FEG operated at 80-200 kV. An Energy Dispersive X-Ray (EDX) detector is attached to the TEM to provide elemental analysis of the sample. The main computer with FEI software controls all microscope functions. The software available to the users is: User Interface (for TEM control and operation), TIA (FEI imaging and EDX software), Gatan Imaging Filter (GIF) and Gatan CCD camera with Digital Micrograph[10].

2.1.2 TITAN

FEI TITAN TEM is equipped with a FEG operated at 80-300 kV, which enables stronger penetration of the electron beam through dense material, atomic scale resolution and minimising the knock-on damage for beam sensitive samples. TITAN has a stable environmental enclosure that isolates the TEM column from external interference and maintains constant environmental conditions. The machine is equipped with an image Cs corrector that gives high probe currents for atomic chemical mapping and sub-Ångstrøm Scanning TEM (STEM) imaging in bright and dark field applications. The pole piece gap in the microscope is 5 mm, large enough for the high tilt range of the specimen that is needed to orient polycrystalline specimen in the desired projection so that the structure can be determined in 3D. The TITAN at Haldor Topsøe, Denmark, is an E-TEM

(Environmental TEM)[11]. The TITAN at Delft, The Netherlands, is not an E-TEM, therefore an additional gas system is needed to perform in-situ TEM experiments inside the machine. The gas system is discussed in detail in section 2.2.5. As in the TECNAI, the main computer with FEI software controls all the microscope functions.

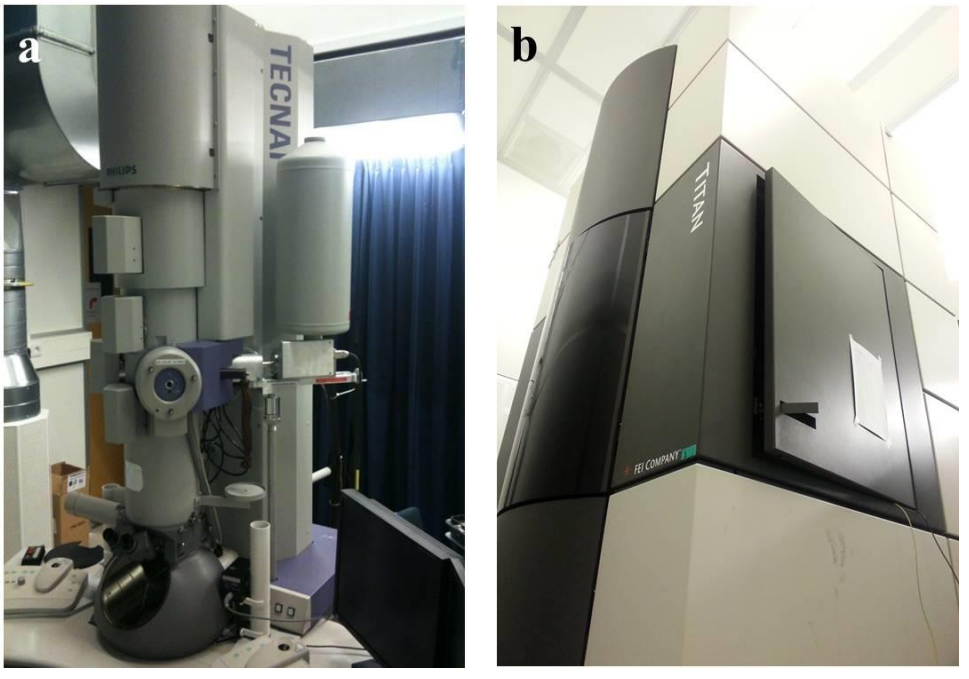

Figure 2.1 (a) TECNAI and (b) TITAN TEM at the Kavli Institute for NanoScience, TU Delft, The Netherlands.

2.2 In-situ TEM

In this section, the design, manufacture and properties of the equipment used for the in-situ TEM experiments are presented. The equipment for the ex-situ and quasi in-situ TEM experiments will be discussed in Chapter 5 and 6, respectively.

2.2.1 Nanoreactor

The nanoreactor is fabricated using Micro-Electro-Mechanical Systems (MEMS) technology[3,12-14]. This technology is known to make very small devices therefore it is possible to miniaturise the complete catalytic reactor, which includes a reactor column, heating system and gas system. Since the catalytic reaction will be conducted inside the TEM and will be monitored during the reaction, the reactor should have good electron transparency and be able to withstand high temperature and pressure. DIMES fabricates in-situ TEM nanoreactors for this project[6,14,15].

The nanoreactor is designed as a windowed cell reactor (Fig. 2.2). This design allows penetration of the electron beam through the nanoreactor while preventing gas exposure into the TEM column. The catalyst particles are loaded inside the nanoreactor. After insertion of the TEM holder (the loaded nanoreactor is included inside), the gas is fed to the nanoreactor to perform a catalytic reaction. The nanoreactor is also equipped with a heating system that enables catalytic reaction at elevated temperature. Four types of nanoreactors have been fabricated by DIMES: glued nanoreactor (GNR), wafer bonded nanoreactor (WBNR), surface micromachined nanoreactor (SMNR) and a new generation of SMNR.

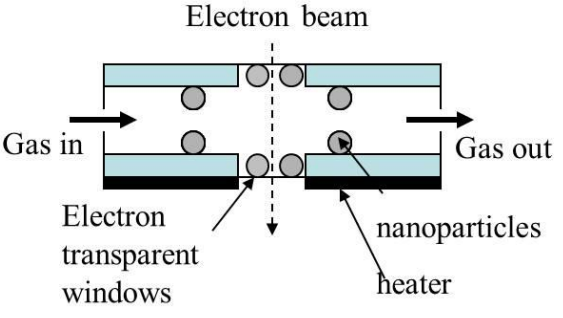

Figure 2.2 Window cell design.

Glued nanoreactor (GNR)

The first generation of in-situ TEM nanoreactors is the GNR[6,16] (Fig. 2.3). This nanoreactor consists of two facing wafers made from silicon substrates. Each wafer has a central hole of 1 mm^2 that is covered by a 1.2 μm thick membrane of amorphous SiN_x. A shallow gas channel is formed from the opposing membranes with a minimum height of 4 μm. The disc spacers that are integrated into one of

the membranes determine the height. The spacers prevent the membranes from collapsing, which would permanently block the channel.

The in-situ TEM nanoreactor should have high electron transparency. In order to achieve this requirement, 20 ultra-thin windows are made in the central part of the membrane. The windows are made from amorphous SiN_x films with 10 nm thickness. To be able to do in-situ TEM catalytic reactions safely, the nanoreactor windows must withstand the gas pressure of more than 1 bar toward the vacuum of the TEM. To prevent bulging of the membrane, which can cause fracture and gas leakage, the windows are ellipsoidal and their size is about 10 μm x 20 μm [6].

To provide heating in the nanoreactor, a microheater is embedded in the central part of the bottom membrane. The heater is able to raise the temperature locally while the rest of the nanoreactor area remains at ambient temperature[17,18]. The heater is a thin film of Pt in a spiral configuration (Fig. 2.3). Four electrical connections provide heating and temperature measurement, with the resistance-based temperature measurement accuracy being ±10 ^{o}C below 50 ^{o}C and ±5 ^{o}C above 50 ^{o}C[19]. For this nanoreactor, the temperature of the heater can be increased up to 500 ^{o}C with minimal thermal drift of the specimen [14].

The disadvantage of this nanoreactor is the use of glue to combine the top and bottom part of the nanoreactor. Under the electron beam, glue can cause hydrocarbon contamination build-up that can interrupt the in-situ TEM experiment. This type of contamination is discussed in Chapter 3. Another disadvantage of this nanoreactor is the difficulty to produce the nanoreactor on a large scale since it is time consuming and highly skilled personnel is needed. Therefore, new designs were made.

Despite these disadvantages, the nanoreactor has been used to perform in-situ reduction of a Cu/ZnO catalyst[6]. The hydrogen gas pressure inside the nanoreactor reached 1.2 bar and the temperature could be increased up to 500 ^{o}C. During the experiments the atomic lattice fringes of the Cu and ZnO were observed. The Cu particle growth and mobility on the ZnO support with the temperature increase could be nicely observed. De Smit et al. used the nanoreactor to perform in-situ STXM (Scanning Transmission X-ray Microscopy). The phase changes in an iron-based Fischer-Tropsch catalyst at atmospheric pressure and up to 350 ^{o}C could be monitored[3].

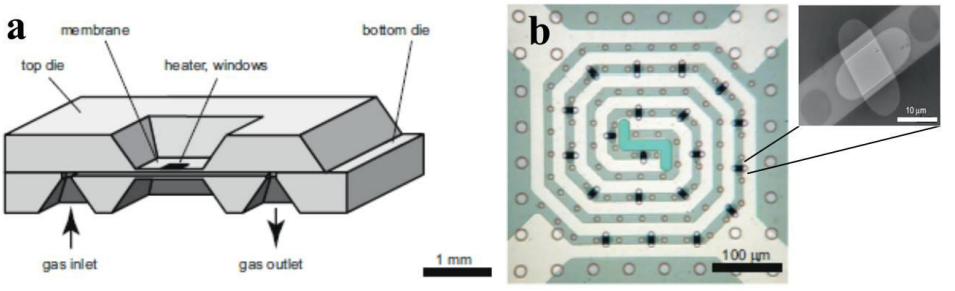

Figure 2.3 (a) The GNR design and (b) top view of the nanoreactor. The bright spiral is the Pt heater. The small ellipses (inset) are the electron transparent windows. The white circles are the SiO_2 spacers (reprinted with permission from[6]).

Wafer bonded nanoreactor (WBNR)

The second nanoreactor type is the WBNR[13]. The glue to fabricate the GNR was an adhesive bonding with epoxy, which may cause hydrocarbon contamination (Chapter 3) because of out-gassing during the experiment in the TEM. In order to avoid contamination due to the use of the glue, several wafer-bonding techniques have been considered to fabricate the nanoreactor. Anodic bonding is not suitable because the use of glass would complicate the fabrication process to produce thin electron transparent windows. Eutectic bonding cannot be applied because the presence of metal alloy can interfere with the catalytic reaction. Silicon fusion bonding is the best candidate for the fabrication because both halves (top and bottom part) of the wafer are amorphous SiN_x which can be finely machined and no intermediate layers are required that could interfere with the performance of the device[20]. The fabrication steps for this nanoreactor are summarised in Fig. 2.4. The fabrication of the bottom part is started with deposition of a 300 nm thermal oxide layer (a). Then it is patterned using buffered hydrofluoric acid (BHF) to form the geometry of the channel. The process continued by the recess opening (b) using deep reactive ion etching (DRIE). The next step is the deposition of a SiN_x layer by low-pressure chemical vapour deposition (LPCVD) (c). Then the heater is formed by a lift-off process (d), and the heater surface is covered by LPCVD SiN_x. After that, dry etching on the nitride layers forms the electron transparent windows (e). Further wet etching using BHF removes the stack layer for the bonding process (f). The nanoreactor top part fabrication steps are similar to those for the bottom part. After the deposition of the SiN_x (a), the spacers are formed by deposition of LPCVD TEOS and BHF wet etching. The contact pad access is formed by opening the entire part

of the back-side of the wafer using 33 wt% KOH at 85 ^{o}C (c). Then the transparent windows are opened using dry etching on the nitride layers. Finally, the stacked layers are removed for the bonding process.

Prior to the wafer bonding process, the wafers are cleaned in RCA-1 solution and aligned with 2 μm accuracy. RCA-1 solution is used to remove organic residues from the silicon wafer. It consists of 5 parts of water, 1 part of 27% ammonium hydroxide and 1 part of 30% hydrogen peroxide. The aligned wafer is then moved into the EV 501 bonder where the bonding and annealing processes are performed. The electrical connections are opened (a) then closed by deposition of PECVD TEOS at 350 ^{o}C (b). A SiN_x layer is then deposited on top of the TEOS layer. The channel, inlet and outlet are defined after 33 wt% KOH etching at 85 ^{o}C (c). The last step is opening of the electrical connection pads by DRIE. In this project, the GNR and WBNR are only used for the window and suspension loading tests.

The WBNR has 2 μm channel height and 20 electron transparent windows made from 15 nm thick amorphous SiN_x films. The spiral heater is made from Pt deposited on a tantalum (Ta) layer. The combination of those two materials provides good adhesion up to 550 ^{o}C. In the gas leak test, the nanoreactor was able to maintain pressures up to 1 bar. The window transparency was proven by atomic resolution images of yttrium barium copper oxide (YBCO) nanoparticles[13].

The disadvantage of this nanoreactor is the relatively low channel height (2 μm). Real catalyst particles might easily form agglomerates that may cause blockage along the channel during suspension loading. But this feature can increase the image resolution since a thinner gas channel will decrease the scattering due to interactions between accelerated electrons and gas molecules. The silicon fusion bonding is also an answer to the large-scale nanoreactor production problems.

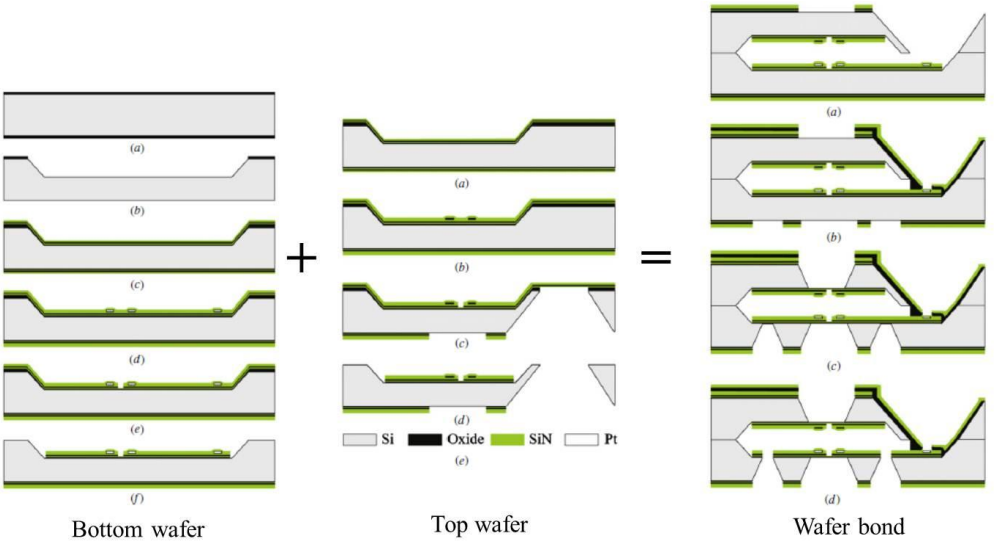

Figure 2.4 Fabrication of WBNR (reprinted with permission from[13]). (See text for description).

Surface micromachined nanoreactor (SMNR)

During the in-situ TEM experiment, gases flow through the nanoreactor channel to perform a catalytic reaction. As mentioned before, the gas molecules can scatter the electron beam and blur the image. To overcome this problem, the in-situ TEM nanoreactor channel should be as thin as possible. This idea is the basis of the SMNR.

The SMNR was fabricated from a Si 100 mm wafer, using surface micromachining techniques (Fig. 2.5)[15]. The fabrication started with the growth of wet thermal SiO_2 layers (0.2 µm) and deposition of LPCVD low-stress SiNx (0.7 µm) to form the bottom of the channel. These layers are provided with holes by means of photolithography and wet etching to define the lower electron transparent windows. The next step is the deposition of TEOS, 1 µm, as a sacrificial layer by low-pressure chemical vapour deposition (LPCVD). Then it is patterned with BHF (buffered HF) to create a mould for the pillars. On top of the wafer a SiN_x (0.5 µm) layer is deposited by LPCVD to form the top channel wall (Fig. 2.5a). Then it is plasma etched to create an array of access holes for the BHF sacrificial etch process. After BHF etching, the interior channel is coated with TEOS (0.25 µm) and SiN_x (15 nm) by LPCVD. The TEOS layer forms an etch

stop layer and the SiN_x layer is the electron transparent window (Fig. 2.5b). The access holes are then closed with SiN_x (15 nm) by plasma enhanced chemical vapour deposition (PECVD). The plugging layer is then sealed by another 0.2 μm of SiN_x by LPCVD (Fig. 2.5c).

Just like the previous generations of nanoreactor, the SMNR consists of a channel, a heater and electron transparent windows. The channel is 4.6 mm long, 0.3 mm wide and 0.5 μm high. The top and bottom parts of the reactor are held together by an array of pillars at a spacing of 20 μm. The pillars increase the stiffness of the channel and reduce bulging when gas is loaded into the channel. A 1 mm^2 area of SiN_x substrate underneath the channel provides high transparency and thermal insulation of the heated zone. The electrical connections and Pt spiral heater provide the heating system. The Pt heater is created from evaporation of Pt (0.2 μm) on top of an adhesion layer of Ta (15 μm) with the lift-off process (Fig. 2.5c). Forty-one electron transparent windows are aligned along the heater. They are made of SiN_x and have a circular shape of 2 μm diameter and 15 nm thickness. The transparency test was performed using Au nanoparticles[15].

The low channel height (0.5 μm) and the array of pillars along the channel trigger difficulties during loading of the catalyst suspension. The particles are trapped near the inlet and form agglomerates. The small particles are also trapped inside the holes that remain under the plugs. These phenomena were observed during loading tests using a fluorescence microscope (see Chapter 4).

Based on the fluorescence microscopy results, a new generation of SMNR was fabricated. The new design has a higher channel, which is now 4.5 μm, while the other details remain the same. This change simplifies the catalyst loading but does not much decrease the image resolution since the pillars hold the membrane so that the bulging effect is reduced. This type of nanoreactor is used for in-situ TEM experiments during this project (Chapter 7).

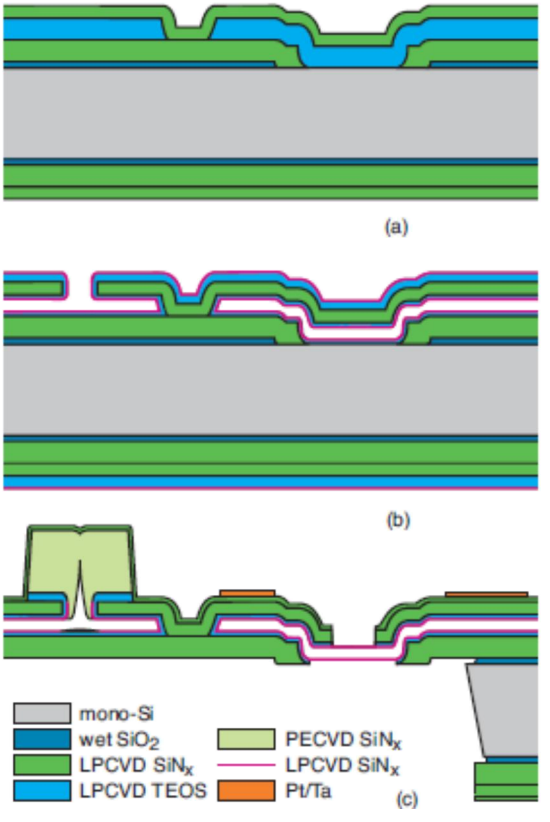

Figure 2.5 Fabrication of SMNR (reprinted with permission from[15]). (See text for description).

2.2.2 Nanoreactor loading

There are two techniques to load catalyst particles into the nanoreactor. The GNR and WBNR are loaded with a loading tool (Fig. 2.6a) while the SMNR is loaded with the drop loading method (Fig. 2.6b). The loading tool is made from steel and consists of two parts, top and bottom. The nanoreactor is placed on the bottom part with inlet and outlet hole facing upwards. Then the top part is placed and the system is sealed with screws. Two channels have been drilled inside the top part and enable the suspension to flow from the inlet to the reactor, and then being discharged from the outlet. The catalyst suspension is dropped with a pipette in the inlet and is sucked at the outlet using syringe suction. After loading, the nanoreactor is taken out from the loading tool and dried on a hot plate. The drying

temperature and time vary, depending on the suspension used. Water-based suspensions need higher temperature (>100 ^{o}C) and longer evaporation time than ethanol-based suspensions that can be dried at room temperature.

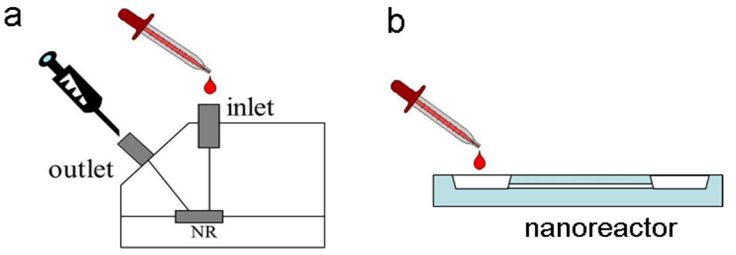

Figure 2.6 The nanoreactor loading process using (a) loading tools and (b) drop loading.

The drop loading uses the capillary forces of the SiN_x membrane channel to direct the suspension from the inlet to the outlet of the nanoreactor. Since the SMNR channel is very narrow, the loading process of this type of nanoreactor using drop loading is quite difficult. The catalyst particles agglomerate at the inlet and outlet and cause blockage of the channel. Therefore, the experiments using this type of nanoreactor are continued using metal salt solution as the metal precursor. As an example, for the CO oxidation experiments on Pt nanoparticles described in Chapter 7, the Pt nanoparticles are obtained from 4% tetrammineplatinum (II) nitrate solution. After drying, the salt compound is decomposed by drying on a hot plate at >100 ^{o}C, leaving platinum oxide nanoparticles on the nanoreactor channel walls, including the windows.

To prevent contamination during the loading process, one should take care to:

1. Use high purity chemicals and water.
2. Use clean loading tools (cleaned using water, ethanol and acetone).
3. Perform the experiment in a clean environment.
4. Use powder-free gloves.

2.2.3 In-situ TEM holder

The in-situ TEM holder used for this project was fabricated by FEI (Fig. 2.7). The development of 3D printing technology simplifies the fabrication of the in-situ TEM holder. The holder consists of several components: holder rod, gas tubes, electrical connections and a nanoreactor slot. The gas tubes are made from steel and interfaced to the nanoreactor with O-rings. The holder is designed to fit

into the FEI microscopes and use the DIMES nanoreactors. Prior to the real in-situ experiment, the holder was tested for compatibility with gases, gas leaking, drift, contamination and resolution.

The gas leak test was performed using a helium leak tester. The holder should be able to withstand the pressure difference down to the normal pressure inside the TEM (~10^{-7} mbar). The TEM holder loaded with a GNR was tested for drift at the Haldor Topsøe TITAN in Denmark. The test was performed at room temperature (with and without gas) and at fast temperature change (<50 μs) from RT-500 ^{o}C, 500-550 ^{o}C, 550-500 ^{o}C with H_2 gas. The drift at room temperature should be less than 0.5 nm/min (regardless of the presence of gas) while under heating and in the presence of gas the drift should be less than 3 nm/s (just after temperature change) and 3 nm/min (after a stabilisation time of 20-30 minutes).

The contamination test was done using a clean nanoreactor. The beam spot with an intensity of 100 ke/nm^{2}s (at 300 kV) at octagon (column) pressure less than 5x10^{-7} mbar was put on one of the transparent window areas for 10 min. Black contamination rings should not be visible in the observation area after the imaging. Details on the contamination problems will be discussed in Chapter 3. The resolution test was performed using a nanoreactor loaded with gold nanoparticles using the drop loading method. The gold lattice fringes of 0.12 nm should be visible. The handling of the holder should follow the rules of cleanliness to avoid carbon contamination during the in-situ TEM experiments. The rules are to always use aluminium foil to wrap the holder during storage and only touch the holder using hands wearing powder-free gloves[21].

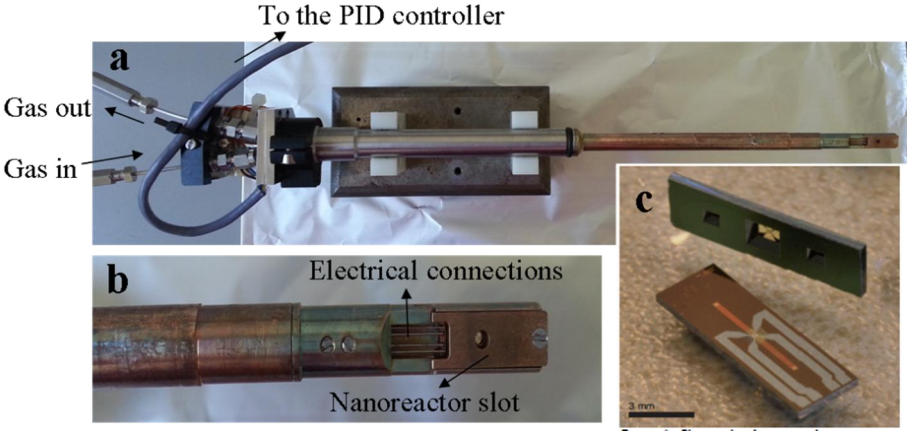

Figure 2.7. (a) The in-situ TEM holder, (b) A closer look on the holder tip shows the electrical connections and nanoreactor slot, (c) The SMNR photographed from different angles (reprinted with permission from[15]).

2.2.4 Temperature controller

The nanoreactor temperature during the in-situ TEM experiments is controlled by a proportional integral derivative (PID) controller, which is made by DIMES. The response time is very fast (milliseconds).

2.2.5 Gas system (at TU Delft)

A gas system designed and fabricated by Leiden Probe Microscopy (LPM) is used for the in-situ TEM experiments. The gas flow diagram used for the in-situ experiments is presented in Fig. 2.8. Gases from the gas bottles flow through the pressure regulators (PR) and mass flow controllers (MFC) to the mixing valve. Small amounts of the mixed gas will flow to the nanoreactor while the rest will be directed to the exhaust system via the backpressure controller (BPC). The gas sent to the nanoreactor is used for the catalytic reaction. The nanoreactor outlet gas flows to the mass spectrometer (MS) for analysis.

The narrow tubes in the LPM gas system result in low dead volume and a minimal dispersion. During the CO oxidation experiments on Pt nanoparticles, the gas is changed between CO-rich and O_2-rich conditions to study the morphological / structural changes of the nanoparticles and the activity changes simultaneously.

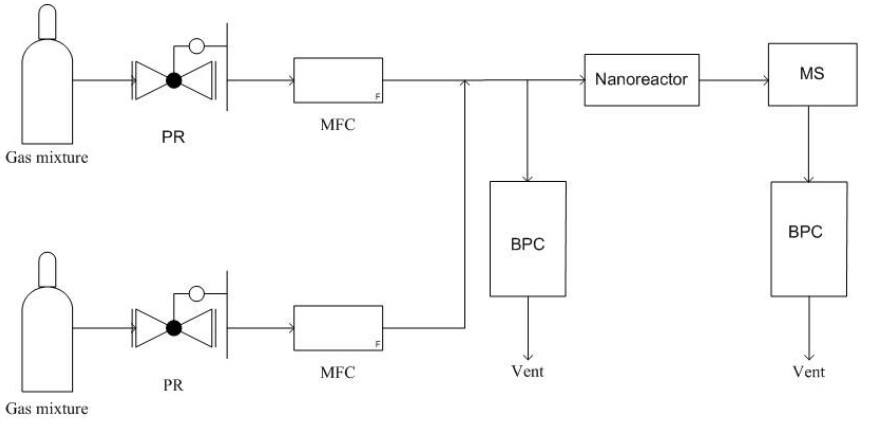

Figure 2.8. The simplified gas flow diagram of LPM gas system.

2.2.6 In-situ TEM experiments

CO oxidation experiments on Pt nanoparticles are performed in this project and will be discussed further in Chapter 7. The nanoreactors are loaded with Pt or Pd nitrate solutions using the drop loading method. The loaded nanoreactors are checked using TEM to verify the availability of nanoparticles for the reaction. This step is also important to check whether carbon contamination occurs, which may be caused by the loading process, and whether windows are damaged, which would lead to gas leaking out of the nanoreactor into the TEM. The loading process can be repeated several times until enough particles have been deposited on the nanoreactor windows. The clean nanoreactor, with enough particles inside, is inserted into the TEM holder. Then a He leak test needs to be performed on the TEM holder, as well as an electrical connectivity test.

The gas system needs to be connected to the TEM holder prior to the experiments and checked for gas leakage. The system should be pumped for a particular time (usually over the weekend) to make sure that the lines of the gas system are clean and will not trigger carbon contamination during the experiments.

After TEM holder insertion, the loaded nanoreactor should be checked for carbon contamination and drift prior to the real in-situ TEM experiments. If there is no contamination, the real experiments can proceed.

2.3 References

1 Yokosawa, T., Alan, T., Pandraud, G., Dam, B. & Zandbergen, H. In-situ TEM on (de)hydrogenation of Pd at 0.5 - 4.5 bar hydrogen pressure and 20 - 400 °C. *Ultramicroscopy* **112**, 47-52, (2012).

2 Almeida, A. R., Moulijn, J. A. & Mul, G. In situ ATR-FTIR study on the selective photo-oxidation of cyclohexane over anatase TiO_2. *J. Phys. Chem. C* **112**, 1552-1561, (2008).

3 De Smit, E., Swart, I., Creemer, J. F., Hoveling, G. H., Gilles, M. K., Tyliszczak, T., Kooyman, P. J., Zandbergen, H. W., Morin, C., Weckhuysen, B. M. & De Groot, F. M. F. Nanoscale chemical imaging of a working catalyst by scanning transmission X-ray microscopy. *Nature* **456**, 222-225, (2008).

4 Dent, A. J., Diaz-Moreno, S., Evans, J., Fiddy, S. G., Jyoti, B. & Newton, M. A. In situ monitoring of oxide-supported platinum-group metal catalysts by energy dispersive EXAFS. *Phys. Scripta T* **T115**, 72-75, (2005).

5 Hendriksen, B. L. M. & Frenken, J. W. M. CO Oxidation on Pt(110): Scanning Tunneling Microscopy Inside a High-Pressure Flow Reactor. *Phys. Rev. Lett.* **89**, 046101, (2002).

6 Creemer, J. F., Helveg, S., Hoveling, G. H., Ullmann, S., Molenbroek, A. M., Sarro, P. M. & Zandbergen, H. W. Atomic-scale electron microscopy at ambient pressure. *Ultramicroscopy* **108**, 993-998, (2008).

7 Ferreira, P. J., Mitsuishi, K. & Stach, E. A. In situ transmission electron microscopy. *MRS Bull.* **33**, 82-90, (2008).

8 Datye, A. K. Electron microscopy of catalysts: Recent achievements and future prospects. *J. Catal.* **216**, 144-154, (2003).

9 Sharma, R. An environmental transmission electron microscope for in situ synthesis and characterization of nanomaterials. *J. Mater. Res.* **20**, 1695-1707, (2005).

10 FEI. *Tecnai™ Transmission Electron Microscope*, http://www.fei.com/products/transmission-electron-microscopes/tecnai.aspx (consulted 14-1-2016).

11 FEI. *Titan™ Transmission Electron Microscope*, http://www.fei.com/products/transmission-electron-microscopes/titan.aspx (consulted 14-1-2016).

12 Creemer, J. F., Helveg, S., Kooyman, P. J., Molenbroek, A. M., Zandbergen, H. W. & Sarro, P. M. A MEMS reactor for atomic-scale microscopy of nanomaterials under industrially relevant conditions. *J. Microelectromech. Syst.* **19**, 254-264, (2010).

13 Mele, L., Santagata, F., Pandraud, G., Morana, B., Tichelaar, F. D., Creemer, J. F. & Sarro, P. M. Wafer-level assembly and sealing of a MEMS nanoreactor for in situ microscopy. *J. Micromech. Microeng.* **20**, (2010).

14 Creemer, J. F., Helveg, S., Kooyman, P. J., Molenbroek, A. M., Zandbergen, H. W. & Sarro, P. M. A MEMS reactor for atomic-scale microscopy of nanomaterials under industrially relevant conditions. *J. Microelectromech. Syst.* **19**, 254-264, (2010).
15 Creemer, J. F., Santagata, F., Morana, B., Mele, L., Alan, T., Iervolino, E., Pandraud, G. & Sarro, P. M. An all-in-one nanoreactor for high-resolution microscopy on nanomaterials at high pressures. *Proc. IEEE Micr. Elect.*, (2011). 1103-1106, ISBN: 978-1-4244-9632-7.
16 Creemer, J. F., Zandbergen, H. W. & Sarro, P. M. Microreactor for a transmission electron microscope and heating element and method of manufacture thereof. *US Patent 01795118 A1*, (2008).
17 Briand, D., Krauss, A., Van Der Schoot, B., Weimar, U., Barsan, N., Göpel, W. & De Rooij, N. F. Design and fabrication of high-temperature micro-hotplates for drop-coated gas sensors. *Sensors Actuat. B: Chem.* **68**, 223-233, (2000).
18 Solzbacher, F., Imawan, C., Steffes, H., Obermeier, E. & Eickhoff, M. A highly stable SiC based microhotplate NO_2 gas-sensor. *Sensors Actuat. B: Chem.* **78**, 216-220, (2001).
19 Vendelbo, S. B., Kooyman, P. J., Creemer, J. F., Morana, B., Mele, L., Dona, P., Nelissen, B. J. & Helveg, S. Method for local temperature measurement in a nanoreactor for in situ high-resolution electron microscopy. *Ultramicroscopy* **133**, 72-79, (2013).
20 Miki, N. Wafer bonding techniques for MEMS. *Sensor Lett.* **3**, 263-273, (2005).
21 Vendelbo, S. *Private communications*, (2013).

3 Carbon Contamination in the Transmission Electron Microscope

3.1 Introduction

To achieve good Transmission Electron Microscopy (TEM) results, microscopists should consider the electron beam interaction with the sample. This interaction often leads to sample defects that could ruin the measurement. TEM carbon contamination is an example of such an interaction. Carbon contamination is a build-up of carbon deposited on the surface of the sample that thickens the sample area, leading to loss of contrast and masking of the fine detail. The contamination sources are adsorbed hydrocarbons in the specimen, which can be introduced during sample preparation. Oil from the conventional TEM machine, which is usually used in the rotary pump and diffusion pump to pull vacuum, can also contribute to the contamination problem[1]. Even though recent TEM technology provides better vacuum to prevent contamination sources from the machine, some contamination can still occur, since the sample itself can act as a local carbon source. Despite the importance of preparing contamination-free samples, published research on this subject is somewhat limited.

This chapter will discuss contamination problems during both ex-situ and in-situ experiments, and how to overcome the problems. The source and formation mechanism of TEM contamination will be discussed. In the end, the in-situ TEM contamination problems led to the development of better in-situ TEM nanoreactors and TEM sample preparation procedures (Chapters 2 and 4).

Kumao et al. categorised the contamination type based on the distribution of the beam, the specimen temperature and the accumulated contamination layer (Fig. 3.1)[2]. Kumao mentioned that a small electron beam size gives a lower temperature at the edge than at the centre of the beam. Therefore, hydrocarbon contamination tends to deposit at the edge of the irradiated region. This type of contamination usually forms visible black rings with a brighter area in the centre. On the other hand, a larger electron beam size will give a more uniform temperature profile with similar temperatures both at the edge and at the centre of the beam. The contamination formed using this type of beam has a more uniform thickness over the irradiated area. Kumao's analysis can be explained with two different theories: hydrocarbon diffusion due to a temperature gradient and due to a concentration gradient.

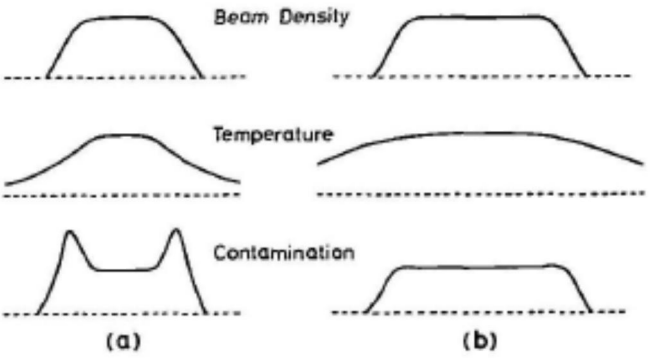

Figure 3.1. Schematic diagrams of the distributions of beam density, sample temperature and accumulated contamination layer. The sample is irradiated by a high-density beam with (a) a small beam diameter, and (b) a large beam diameter (reprinted with permission from[2]).

Hydrocarbon surface diffusion due to temperature gradient

During TEM observation, when the beam hits the sample, the intensity pattern of the beam follows a Gaussian shape distribution with the brightest region in the centre followed by gradient bright rings. At the centre of the pattern, the intensity reaches its peak value, and so does the temperature as depicted in Fig. 3.2. This temperature profile leads to a temperature gradient within the beam intensity pattern of which the gradient vectors are in the direction towards the centre of the pattern. The temperature gradient that is present within the pattern can induce the diffusion of the contamination molecules from the hotter region (centre of the beam) towards the colder region (the edge of the beam). This phenomenon is known as thermal diffusion or thermophoresis[3-5]. In a steady state situation, molecules are accumulating at the colder area.

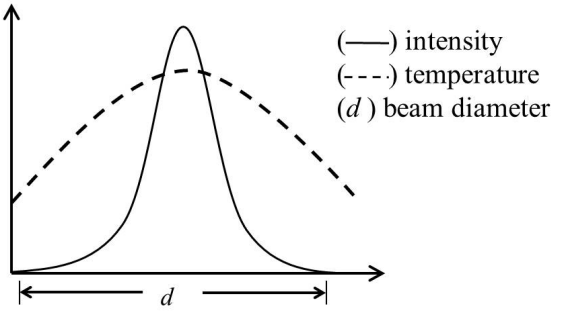

Figure 3.2. Typical beam intensity pattern. Both the intensity and temperature reach their maximum at the centre. (*d* is the diameter of the beam).

The physical mechanism of thermophoresis of the particles in a gaseous environment depends on the ratio between the gas mean free path (λ = 0.066 μm)[6] and the particle/molecule size (d_p), known as the Knudsen number (Kn)

$$Kn = \frac{\lambda}{d_p} \qquad \text{Eq. 3.1}$$

If $Kn \geq 1$ (very low density gas), the thermophoresis force depends on the temperature gradient in the surrounding molecules. However, if $Kn \leq 1$ (high density gas), the thermophoresis force depends on the thermal conductivity of the molecules. The molecules in the hot region have a higher velocity (u_h) than molecules in the colder region (u_c). Therefore when the contaminated molecules which are assumed to be small, collide with the gas molecules (at $Kn \geq 1$), they receive higher momentum transfer from the hotter gas than from the colder gas ($\Sigma m_h u_h > \Sigma m_c u_c$). This causes a net force (F_{th}) towards the colder region as illustrated in Fig. 3.3. Theoretically, the net force experienced by molecules of diameter (d_p) due to the temperature gradient field is predicted by Waldmann in this equation;

$$F_{th} = \frac{p\lambda d_p^2}{T}\nabla T \qquad \text{Eq. 3.2}$$

where p is the gas pressure, λ is the gas mean free path, and T is the absolute temperature[5,7] .

This thermophoresis effect can explain the formation of the contamination during TEM imaging. The focussed (small diameter) beam has a sharp Gaussian distribution that leads to large temperature gradients (ΔT). The net force exerted by the molecules in the hotter region drives the hydrocarbon molecule to the colder

region, resulting in the accumulation at the edge of the beam. This then shows as a black ring on the surface of the TEM sample (Fig. 3.4a).

The defocussed beam has a more uniform distribution. The net thermophoretic force on the molecules is lower, therefore they cover a wider region, which shows as contamination with uniform thickness over the irradiated area (Fig. 3.4b). These hypotheses correspond to the TEM contamination classification proposed by Kumao et al[2].

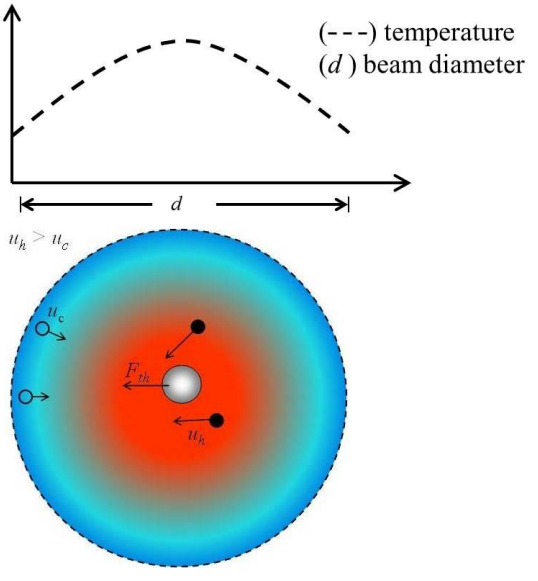

Figure 3.3. Gas molecular impact on contamination in a temperature gradient. The contaminating molecules collide with the gas molecules from both the hot and the cold sides. The gas molecules from the hot side transfer higher momentum to the contaminant, causing a net force to the cold side.

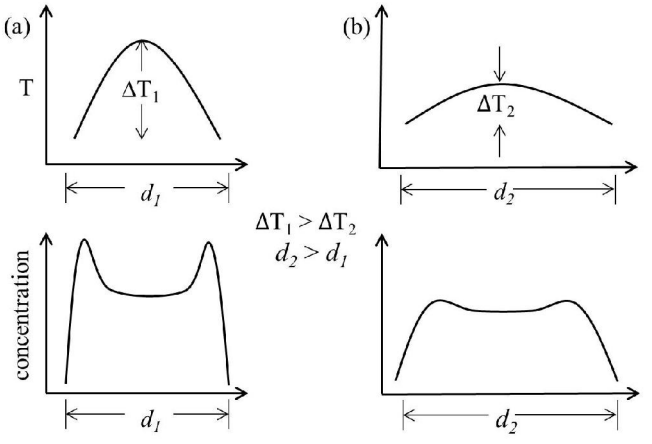

Figure 3.4. Correlation between beam intensity (top) and hydrocarbon concentration profile (bottom), describing the mechanism of TEM contamination based on hydrocarbon diffusion due to the temperature gradient. (a) TEM contamination profiles based on the focussed (small beam) diameter, and (b) defocussed (larger) beam diameter.

Hydrocarbon surface diffusion due to concentration gradient.

Another diffusion mechanism that places carbon contamination within the electron beam is hydrocarbon surface diffusion due to a concentration gradient[8]. The surface diffusion of the hydrocarbons due to a concentration gradient can be described using Fick's first law of diffusion. The steady-state reaction-diffusion problem is described by:

$$0 = D\,\nabla^2 c - v \qquad \text{Eq. 3.3}$$

Where D is the diffusivity, $\nabla^2 c$ is the derivative of the concentration gradient, and v is the hydrocarbon cracking rate.

Hydrocarbons are cracked under the electron beam, resulting in low concentrations of hydrocarbons in the illumination area. This triggers hydrocarbon diffusion from the surrounding area into the illuminated area. If the beam is focussed (diameter is small), the hydrocarbon diffusion rate is smaller than the cracking rate inside the illuminated area ($D\,\nabla^2 c \leq v$). Therefore, the cracked hydrocarbons accumulate at the edge region of the illuminated area, resulting a dark ring-like deposit. If the beam is defocussed (diameter is large), the hydrocarbon diffusion rate is relatively larger than the cracking rate inside the beam ($D\,\nabla^2 c \geq v$). Therefore, the cracked

hydrocarbon accumulates inside the illuminated area resulting in a more uniform dark effect (Fig. 3.5).

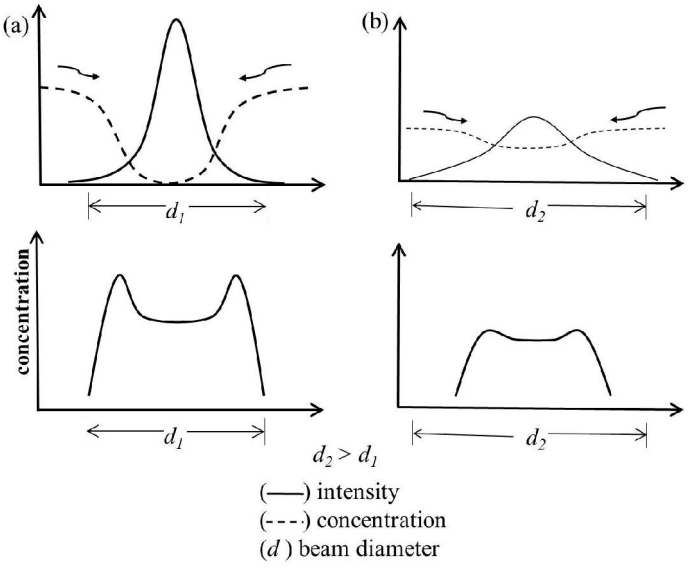

Figure 3.5. Correlation between beam intensity (top) and hydrocarbon concentration profile (bottom), describing the mechanism of TEM contamination based on hydrocarbon diffusion due to the concentration gradient and cracking in the illuminated region. (a) The TEM contamination profiles based on focussed (small beam) diameter, and (b) defocussed (larger) beam diameter.

Since hydrocarbon contamination is undesirable, Egerton et al. suggest the following steps to prevent it[8]:

1. Heat the sample with a lamp to desorb hydrocarbons from its surface. For heat sensitive samples, irradiation by a small UV lamp is effective.
2. Expose the sample to energetic ions in a plasma cleaner, which sputters away the surface layer[9].
3. Flood the surrounding area with electrons, by defocussing the illumination and removing the condenser aperture, in order to polymerise surface hydrocarbons and prevent them from diffusing toward the focused probe.

4. Heat the sample to about 300 ^{o}C in the TEM in order to desorb the hydrocarbons from its surface and maintain a low hydrocarbon concentration during imaging.
5. Cool the sample during observation and thereby reduce the mobility of hydrocarbons.

Steps 1 and 2 are ex-situ treatments of the sample before imaging under the TEM, while steps 3, 4 and 5 are in-situ TEM treatments. Working in a clean environment and performing sample preparation according to standard clean working procedures also help to prevent contamination problems. Cleaning all equipment that will be used to prepare the sample with acetone and ethanol is a must. These solvents dissolve organic materials that are attached to the equipment. Routine plasma cleaning of the TEM holder is recommended. For the removal of hydrocarbon contamination, a mixture of 25 % oxygen and 75% argon was found to be suitable as the plasma source[9-11]. This composition is sufficient to remove the hydrocarbons while also considering the laboratory safety compared to the use of pure oxygen.

Isabell *et al*. investigated the effect of plasma cleaning on a TEM sample[9]. Figure 3.6 shows TEM images of a $SrTiO_3$ film that has been mechanically polished, dimpled and ion milled during sample preparation. Prior to the plasma cleaning, several contamination circles were formed. After 1 minute of plasma cleaning the sample was checked under the TEM. No additional contamination was observed. Longer plasma cleaning time showed that the contamination circles were fading (some almost disappeared).

Despite these successful results, microscopists should consider the nature of their sample before using this plasma cleaning technique. For example, contact with plasma can trigger changes in the oxidation state of metal nanoparticles[12,13].

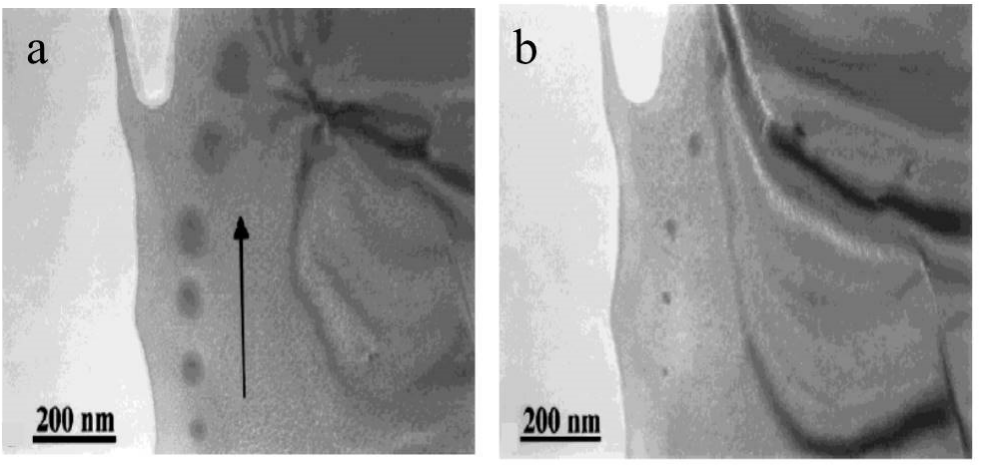

Figure 3.6. (a) TEM images of $SrTiO_3$ taken after 1 minute and (b) 5 minutes of plasma cleaning (reprinted with permission from[9]).

3.2 Experimental methods

A copper TEM grid coated with amorphous microgrid carbon as received from QUANTIFOIL® was tested for contamination. In this contamination test, an empty area of the grid was irradiated with the electron beam for 5 minutes. The beam was set to a particular diameter, acceleration voltage 200 kV (FEI Tecnai F20 TEM) and beam density of 100 ke/nm^{2}s. Before and after the contamination test, an overview image of the grid was taken. If the irradiation formed a black circle on the observation area, the sample was considered to be contaminated.

TEM contamination during ex-situ TEM experiments

Capping agents (usually hydrocarbons) are commonly used to avoid aggregation of nanoparticles in the suspension and to control the size as well as the shape of the nanoparticles during catalyst preparation. At the end of this process, the capping agents are still attached to the surface of the catalyst, and may hamper its catalytic action[14]. Under the electron beam, the capping agents cause contamination, which disturbs the sample analysis. Removal of the capping agents from the surface of gold catalysts is the main topic of the ex-situ experiments (Chapter 5).

The gold nanoparticles were produced via colloidal methods and immobilised on γ-Al_2O_3 support to obtain Au-DDA/ γ-Al_2O_3 catalysts. The capping agent is dodecylamine (DDA). The catalysts were then plasma treated to remove the capping agent. The reaction was performed at room temperature to prevent morphological changes of the gold nanoparticles. Fourier Transform Infrared (FTIR) spectroscopy and TEM were used to characterise the catalysts before and after capping agent removal.

For the TEM analysis, a drop of Au-DDA colloid was deposited on the copper grid coated with amorphous carbon and left to dry at room temperature. To prepare TEM samples from the Au-DDA/γ-Al_2O_3 catalysts, the catalysts were ground and suspended in ethanol. A drop of the suspension was deposited on the copper grid and left to dry at room temperature. Prior to the TEM sample preparation, all the equipment was cleaned with water, acetone and ethanol in order to prevent contamination. High purity (99.9 %) ethanol was used to make the suspension. The sample preparation was conducted on a clean laboratory desk.

TEM contamination during in-situ TEM experiments

For some preliminary in-situ TEM experiments (not reported in this thesis), Pt/γ-Al_2O_3 catalyst samples were deposited on the SiN film inside the in-situ TEM nanoreactor. The nanoreactor was fabricated using MEMS technology (Chapter 2). The first nanoreactor generation, glued nanoreactor, consists of two facing wafers made from silicon substrates, which are glued together to form a complete reactor. The glue used in this process was an adhesive bonding with epoxy. The glue may cause hydrocarbon contamination because of outgassing during the experiments in the TEM[15,16].

To load the sample, a dedicated loading tool was used (Fig. 2.6a). Prior to the loading experiment, all equipment and tools such as the tweezers, screws and O-rings were consecutively cleaned with water, acetone and ethanol. For each cleaning solvent, the equipment was placed in a sonicator for 10 minutes. The loading tool for the glued nanoreactors has two Viton O-rings that prevent direct contact of the nanoreactor with the loading tool's steel surface. After the cleaning steps, the O-rings were dried on a hot plate at 80 ^{o}C for 15 minutes. After loading, the nanoreactor was dried on a hot plate at 80 ^{o}C temperature for 15 minutes. After drying, the nanoreactor was inserted into a dedicated TEM holder (Chapter 2) for TEM imaging. Prior to use, the TEM holder was also plasma cleaned for at least 10 minutes using a Fischione Plasma cleaner 1020 (80% Ar in 20% O_2).

3.3 Results and discussion

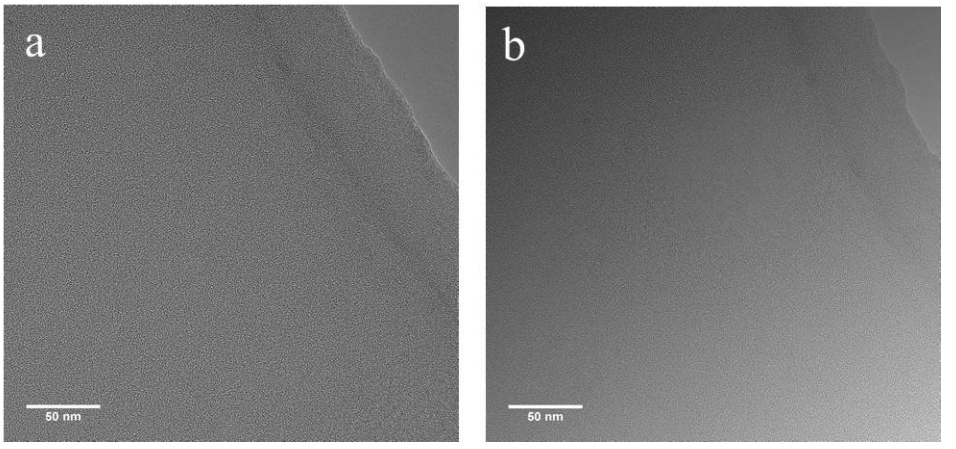

Figure 3.7. (a) TEM images of the TEM grid before and after (b) contamination test.

TEM contamination in ex-situ TEM experiments

Figures 3.7a and b show images of the TEM grid before and after the contamination test. The as-received TEM grid was clean and in good condition, since no contamination was observed. These results are in contrast with the TEM grid loaded with as-synthesised Au-DDA colloid. The grid exhibited strong contamination under the electron beam (Fig. 3.8a). The black ring is the result of DDA decomposed by the electron beam. It was difficult to take high magnification images of the particles. Therefore, the colloid was washed with acetone and redispersed in cyclohexane. The washed colloid was dropped on the TEM grid and analysed under the TEM. The washing step removed the excess of DDA in the colloid; less contamination was observed from this sample (Fig. 3.8b). But DDA is still present on the gold particle surface (from FTIR data). To remove the DDA from the surface of the catalyst, the samples were plasma treated at room temperature. TEM and Infrared (IR) spectroscopy indicated that the capping agent was removed after 8 h plasma cleaning treatment (Fig. 3.8c and Chapter 5).

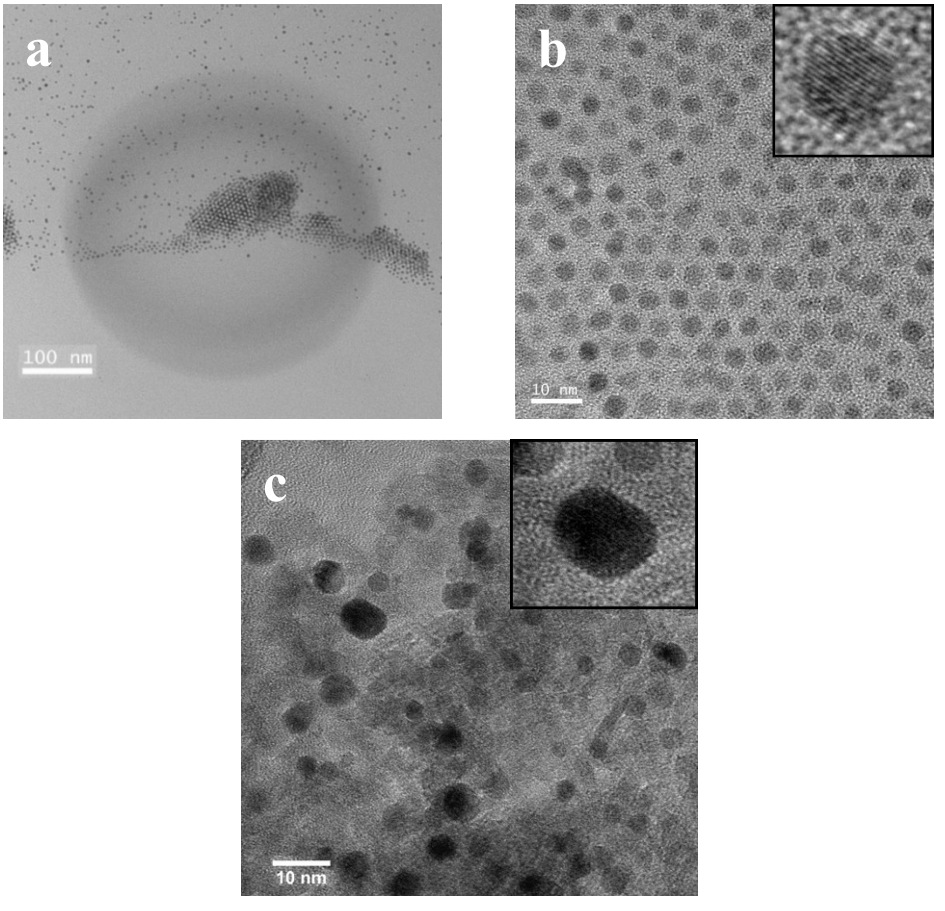

Figure 3.8. TEM image of Au-DDA colloid on the TEM grid (a) before and (b) after washing. The inset shows that the Au particles are crystalline. (c) TEM image of Au-DDA/γ-Al_2O_3 support after the catalyst was plasma cleaned for 8 hours. The particle size of plasma treated catalyst is sintered but since the ozone treatment is at mild temperature, the agglomeration is less than at high temperatures (Chapter 5). The insets show that the particles remain crystalline.

TEM contamination during in-situ TEM experiments

Even though precautions had been taken during the sample preparation, severe contamination was still occurring during in-situ TEM imaging using glued nanoreactors (Fig. 3.9a and b). The contamination sources could be the glue inside the nanoreactor and contaminated gas used during the experiment. The Pt/γ-Al_2O_3

catalyst and solutions used to load the catalyst were also among the suspects of the contamination. To prevent contamination from the gas, high purity gas was used. The tubes of the gas system were flushed with nitrogen gas prior to the experiment. Figures 3.9c and d show contamination on a Pt/γ-Al_2O_3 particle in artificial air. The contamination was reduced after changing the gas bottle and a longer time flushing process through all the gas system tubes (depending on the contamination level, minimum 15 min). Since the nanoreactor was contaminated, the in-situ experiments were performed at lower magnification (defocused beam). Figure 3.10a was taken at magnification of 145kx. Severe deformation as a result of contamination on the Pt particles can be observed. Figure 3.10b was taken at defocused beam (magnification 115kx). Less deformation on the particle was observed. The defocused beam polymerises surface hydrocarbons and prevents them to diffuse toward a focused probe. This will prevent further contamination in the observation area.

Contamination in the glued nanoreactor led to the development of the second generation of nanoreactors, using the wafer bonding method to connect the top and bottom parts of the nanoreactors. This technique resulted in nanoreactors free from contamination under the electron beam[17] (Chapter 2). In Chapter 7, the real in-situ TEM experiment used surface micromachined nanoreactor (SMNR) loaded with tetrammineplatinum (II) nitrate solution. The nitrate compound was decomposed by drying on a hot plate at 300 ^{o}C, leaving platinum oxide particles inside the nanoreactor.

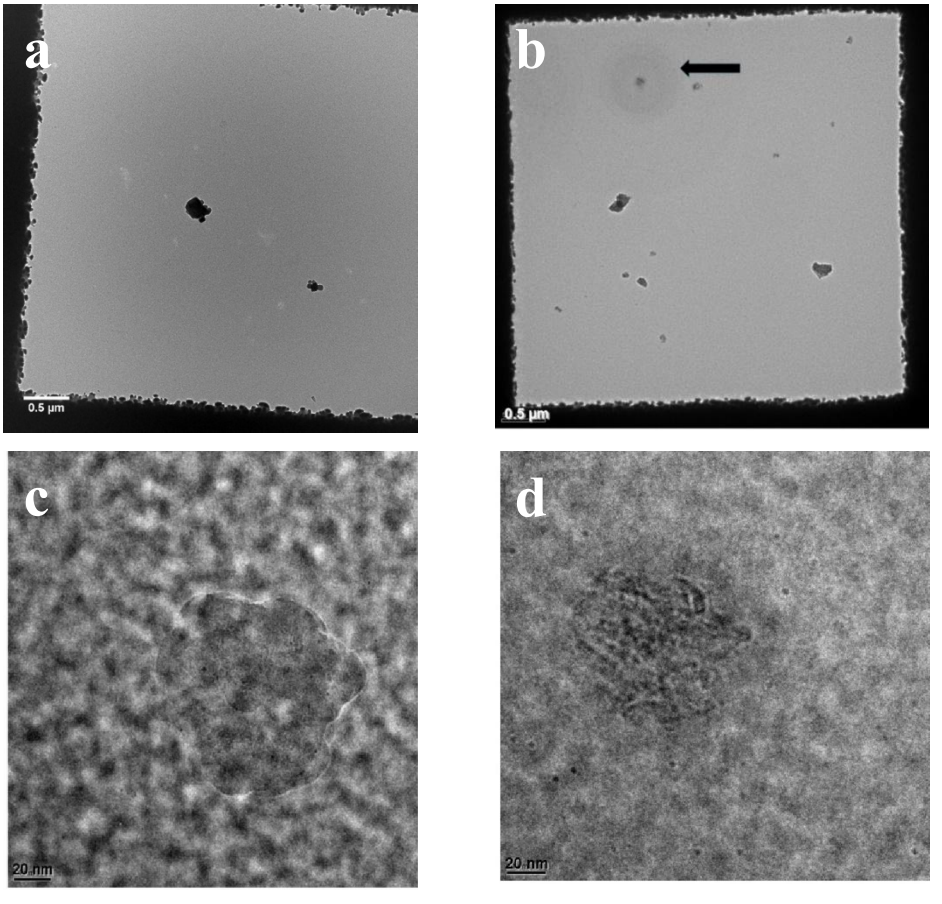

Figure 3.9. (a) TEM image of a window of a glued nanoreactor as received from manufacturer. The black particles are the remains of an uncompleted etching process. (b) Severe carbon contamination is observed after imaging of the particles in a glued nanoreactor. (c) TEM images of Pt/γ-Al_2O_3 in a glued nanoreactor at 50 ^{o}C in H_2, and (d) in artificial air.

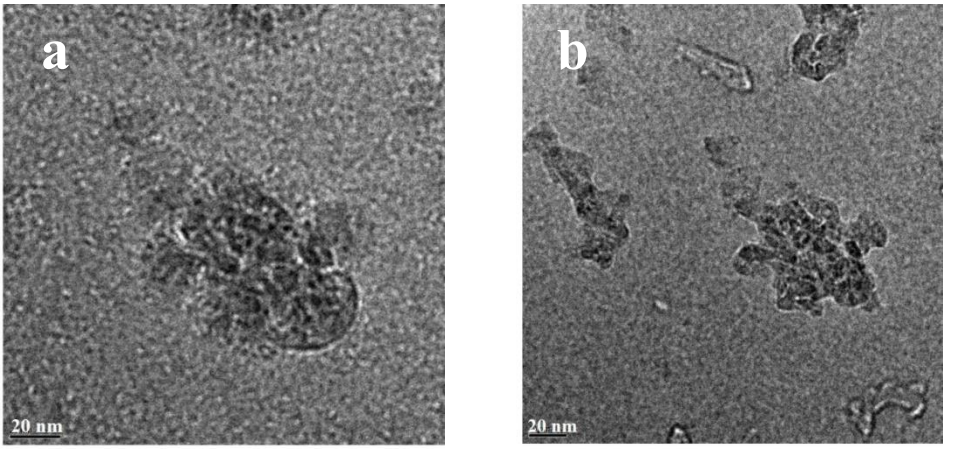

Figure 3.10. TEM image of a Pd/γ-Al_2O_3 catalyst particle at magnification of 145kx (a), and 115kx (b). The imaging was conducted in vacuum and at room temperature.

TEM contamination mechanism

Two hypotheses have been postulated for the contamination mechanism in TEM: hydrocarbon diffusion due to temperature gradient or concentration gradient. In order to understand which gradient drives the contamination mechanism, a contamination experiment was done using inorganic nanotube rods deposited on a TEM grid (Fig. 3.11). An original rod before high-intensity, small diameter beam illumination is indicated as D. After high-intensity, small diameter beam illumination, the rods show semi-circles of carbon deposit protruding from the side where they are attached to the TEM grid. The area indicated as (A) was exposed to a high-intensity, small diameter beam of larger diameter than those denoted (B and C). Nanorod B was exposed to a high-intensity, small diameter beam at the edge of the rod, while nanorod C was illuminated at the center of the rod. Nanorods B and C show semi-circle contamination only at the side of the illuminated spot near the grid, whereas no deposit is visible at the gas-phase side. This shows that hydrocarbon surface diffusion from the TEM grid to the illuminated area causes contamination rather than gas-phase diffusion of hydrocarbons.

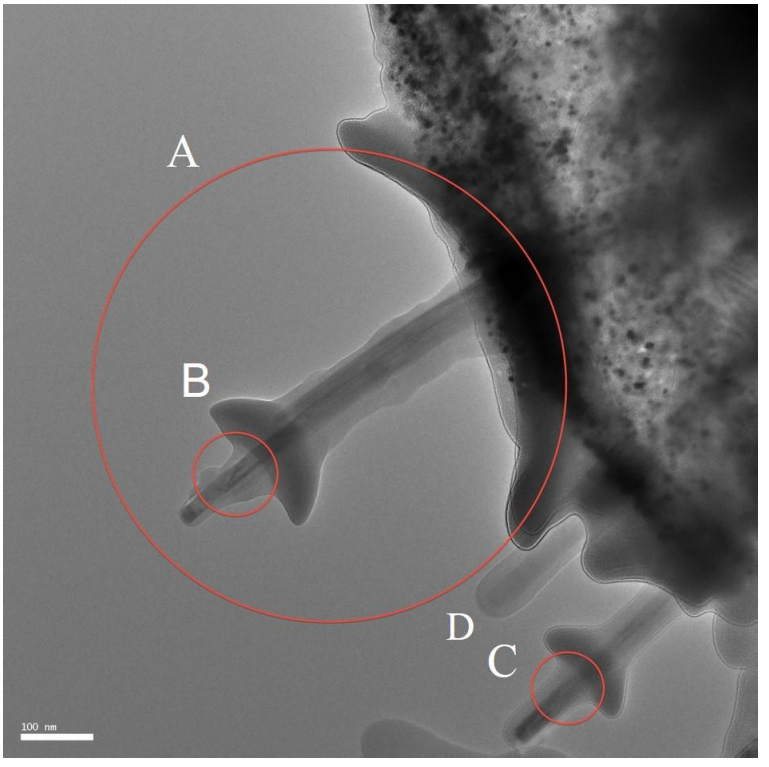

Figure 3.11. Semi-circle hydrocarbon contamination on contaminated TEM grid (S. Vendelbo is acknowledged for recording this image). (See text for description).

3.4 Conclusions

Contamination is one of the important problems in transmission electron microscopy. The phenomenon is the result of hydrocarbon surface diffusion triggered by the concentration gradient. Under the TEM electron beam, molecules in the illumination area are cracked, forming a low hydrogen concentration gradient in the illumination area. Diffusion of molecules from the high concentration area (surrounding the illumination area) to the lower concentration area (inside the illumination area) results in formation of a ring-like or uniform contamination (depending on the beam focus and intensity). The source of hydrocarbon contamination can come from the sample and the equipment used during the TEM imaging. Following high cleanliness standard TEM preparation procedures will reduce the probability of contamination from the sample. Clean and dry TEM equipment is required to prevent contamination. For in-situ TEM

experiments, O-rings and loading equipment should be cleaned in water, acetone and ethanol, followed by drying on a hot plate. It is important to plasma-clean the TEM holder and precautions should be taken during the nanoreactor fabrication process as contamination sources can also be introduced in the clean room. For in-situ TEM experiments, flushing the gas system tubes with nitrogen prior to the experiment is important. The use of high purity gas is a must. Contaminated samples, e.g. metal nanoparticles covered with surfactant molecules that are hard to remove, can still be used for imaging at low magnification.

3.5 References

1 Reimer, L. & Kohl, H. Specimen damage by electron irradiation. *Springer Series Opti.* **36**, 456-487, (2008).

2 Kumao, A., Hashimoto, H. & Shiraishi, K. Studies on specimen contamination by transmission electron microscopy. *J. Electron Microsc.* **30**, 161-170, (1981).

3 Duhr, S. & Braun, D. Why molecules move along a temperature gradient. *PNAS* **103**, 19678-19682, (2006).

4 Geelhoed, P. F., Lindken, R. & Westerweel, J. Thermophoretic separation in microfluidics. *Chem. Eng. Res. Des.* **84**, 370-373, (2006).

5 Waldmann, L. & Schmitt, K. *Aerosol Sci.* (Academic Press, 1966).

6 Jennings, S. G. The mean free path in air. *J. Aerosol Sci.* **19**, 159-166, (1988).

7 Hinds, W. C. *Aerosol technology: Properties, behaviour, and measurement of airbone particles*. (Willey, 1999). ISBN 978-0-471-19410-1

8 Egerton, R. F., Li, P. & Malac, M. Radiation damage in the TEM and SEM. *Micron* **35**, 399-409, (2004).

9 Isabell, T. C., Fischione, P. E., O'Keefe, C., Guruz, M. U. & Dravid, V. P. Plasma cleaning and its applications for electron microscopy. *Microsc. and Microanal.* **5**, 126-135, (1999).

10 Fischione, P. E., Ringnalda, J., Feng, Y., Krekels, T., Hayles, M., Colijn, H. O., Mills, M. J. & Wiezorek, J. M. Use of a cold gas plasma for the final processing of contamination-free TEM specimens. *Mater. Res. Soc. Symp. Proc.* **480**, 225-234, (1997).

11 Isabell, T. C., Fischione, P. E. & Fischione, E. A. Applications of plasma cleaning for electron microscopy. *IEEE International Conference on Plasma Science*, (IEEE, 1998), 127-128, ISBN: 978-0780347922.

12 Debiemme-Chouvy, C., Ballutaud, D., Pesant, J. C., Severac, C. & Etcheberry, A. Modification of GaAs surface stoichiometry and reactivity induced by a hydrogen plasma. *Appl. Surf. Sci.* **65-66**, 643-646, (1993).

13 Zemlyanov, D. Y., Fingland, B. R., Wei, A., Durbin, S. M. & Ribeiro, F. H. Plasma cleaning applications for surface science and model catalyst samples. *Microsc. Microanal.* **15**, 816-817, (2009).
14 Quintanilla, A., Butselaar-Orthlieb, V. C. L., Kwakernaak, C., Sloof, W. G., Kreutzer, M. T. & Kapteijn, F. Weakly bound capping agents on gold nanoparticles in catalysis: Surface poison? *J. Catal.* **271**, 104-114, (2010).
15 Creemer, J. F., Helveg, S., Hoveling, G. H., Ullmann, S., Molenbroek, A. M., Sarro, P. M. & Zandbergen, H. W. Atomic-scale electron microscopy at ambient pressure. *Ultramicroscopy* **108**, 993-998, (2008).
16 Creemer, J. F., Zandbergen, H. W. & Sarro, P. M. Microreactor for a transmission electron microscope and heating element and method of manufacture thereof. *US Patent 01795118 A1*, (2008).
17 Mele, L., Santagata, F., Pandraud, G., Morana, B., Tichelaar, F. D., Creemer, J. F. & Sarro, P. M. Wafer-level assembly and sealing of a MEMS nanoreactor for in situ microscopy. *J. Micromech. Microeng.* **20**, (2010).

4 Loading Nanoreactors for In-situ TEM analysis: A Flow Imaging Study

4.1 Introduction

Much of the catalyst characterisation effort concerns pre- and post-mortem analysis of the catalyst (Chapter 5). Although this yields information about the catalyst before and after use, a direct relation with the catalyst under working conditions cannot be given. In-situ studies provide more direct information, leading to a better understanding of the catalytic phenomena[1-4]. In-situ TEM is a direct method to study the structural and morphological changes of catalysts during catalytic reactions[5-8]. Since TEM requires high vacuum conditions, catalytic reactions operated at atmospheric to high pressures (and high temperature) are incompatible with conventional TEM operation. The gas present inside the TEM would damage the electron gun, scatter the electron beam and perturb the imaging process.

In order to study the catalyst during catalytic reaction under the TEM, Baker et al. introduced in-situ TEM using the Controlled Atmosphere Electron Microscope (CAEM) in the early 1970's[9] (Chapter 1). This method was modified by Gai et al. to perform catalytic reaction in Environmental TEM (ETEM) mode. These instruments needed major modifications with respect to the standard TEM. Giorgio et al. developed closed-window reactors incorporated in the TEM holder[11]. This system has been used to perform TEM experiments at temperatures up to 350 ^{o}C and pressures up to 10 mbar. Saka et al. incorporated a gas injection nozzle inside the TEM holder to study the oxidation of In to InO and the reversible reduction of SiO_2 and oxidation of Si[12].

Further developments in in-situ TEM resulted in a reactor that can be easily inserted to or removed from a dedicated in-situ TEM holder[7,13,14] (Chapter 2). The reactor should be able to withstand high gas pressure and high temperature. It should also have electron transparent windows to be able to perform imaging under the electron beam. These challenges can be addressed using microelectromechanical system (MEMS) techniques, based on the design of a nanoreactor that is a miniaturised version of a real catalytic reactor[7,15,16]. This nanoreactor is a flow reactor design based on the windowed cell. It consists of a gas inlet and outlet, a channel and a heater area. The catalytic reaction is performed inside the cell, which is coated with a thin SiN_x layer. Some parts of the layer have electron transparent windows where TEM imaging can be performed (Fig. 2.2).

Creemer's group at Delft Institute of Microsystems and Nanoelectronics (DIMES) developed several types of nanoreactors for this purpose[7,8]. They are the glued nanoreactor[7,17], the wafer bonded nanoreactor (WBNR)[15] and the surface micromachined nanoreactor (SMNR)[16]. Each of these nanoreactors has advantages and disadvantages in terms of the fabrication process and applications. These different types of nanoreactors are described in detail in Chapter 2.

Loading the catalyst into a nanoreactor is challenging due to the design of the channel and the tendency of the small catalyst particles to agglomerate, which may even block the channel. It is also difficult to get the particles on the transparent window areas for the TEM imaging. The nanoreactor loading technique used here is based on a suspension of small catalyst particles. Therefore, the flow of this suspension into and inside the reactor volume needs to be analysed. In this chapter, we report the utilisation of flow imaging techniques to study the flow of suspensions inside two nanoreactor versions.

Flow imaging is a particle analysis technique using microscopy technology where the images are captured in successive frames as a continuous sample stream passes through a flow cell[18]. The technique has been widely used in pharmaceutical and biomedical applications[19-24]. The fluorescent microscope is one of the instruments usually used for this technique. Fluorescent particles are loaded into the cell, which contains micro channel(s). The fluorescent emissions detected are displayed as real time images of the particle flow inside the channel(s). This gives information about particle velocity and distribution, channel defects and blocking of the channel.

4.2 Experimental methods

The experimental set up consists of a Zeiss Axiovert 200 inverted fluorescence microscope equipped with a mercury lamp, an excitation filter, objective lenses and optical filters, a CCD camera (La Vision VC-Imager Intense) and DAVIS imaging software, as illustrated in Fig. 4.1. The mercury lamp emits polychromatic light with various wavelengths. The excitation filter selects monochromatic green light (wavelength ~ 510 nm) because the fluorescent particles used are red fluorescent (wavelength ~ 650 nm). The light is focused by the objective lens and hits the fluorescent particles inside the nanoreactor. The fluorescent particles absorb the low wavelength light (in this experiment the green light was used) and emit the higher wavelength light (red light). The dichroic filter reflects the illumination light and transmits the red light to the CCD camera. Instead of bottom illumination and view, the illumination of the Zeiss fluorescence

microscope can be set as top illumination and bottom view. This procedure is similar to light optical microscopy and is useful to study non-fluorescent materials.

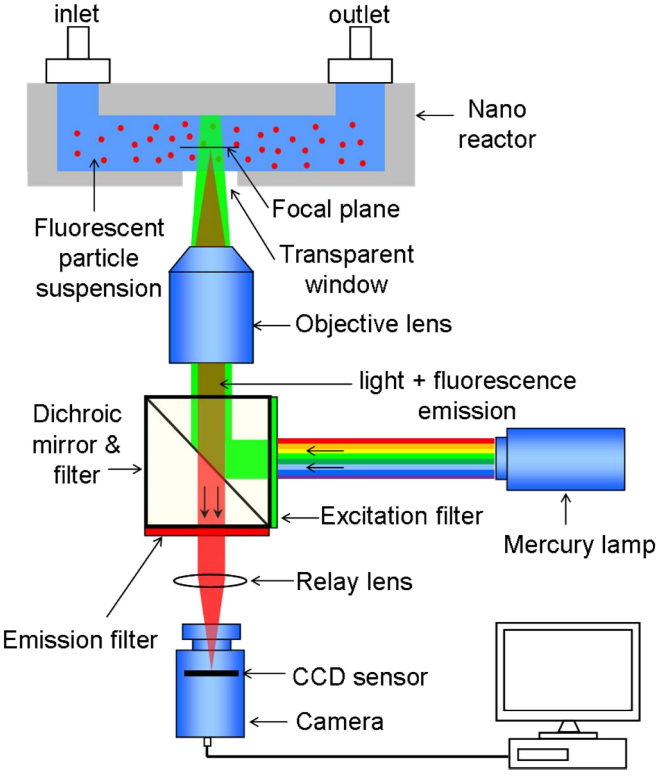

Figure 4.1. The inverted fluorescence microscope set up used in the experiment.

The WBNR and SMNR were studied using this technique. The nanoreactors were loaded with fluorescent polystyrene microspheres (DukeScientific PEG coated Polystyrene Fluorescent particles) suspended in 70% ethanol, 30% water. The suspensions used in this experiment contained about 10% and 2% (v/v) of particles. Three different particle diameters of 0.25, 0.5 and 1 μm were used (< 5% size distribution).

The suspensions were loaded into the nanoreactors using the drop loading technique where the penetration into the nanoreactor was driven by capillary forces. Prior to the loading, the channel was pre-cleaned with some drops of 30% deionised water mixed with 70% ethanol. A nanoreactor was put under the microscope and a drop of suspension was dropped in the inlet using glass

droppers. The particles were illuminated by the light source and their movement along the nanoreactor channel was captured and recorded by CCD camera. The imaging was started as soon as the suspension was dropped at the inlet.

4.3 Results and discussion

The nanoreactor channel wall is a hydrophilic SiN_x membrane[15,16]. But during storage the surface of the membrane can pick up contaminants from the air, which reduces its hydrophilicity[25]. Pre-cleaning the channel with water and ethanol can clean the surface and restore its hydrophilicity. In this experiment, the suspension is ethanol based because ethanol has a low surface tension so it will penetrate easily into the nanoreactor channel. The ethanol is also easy to evaporate due to its low boiling point. This results in dry catalyst particles in the nanoreactor. Using a water-based suspension is also possible, depending on which catalyst will be studied.

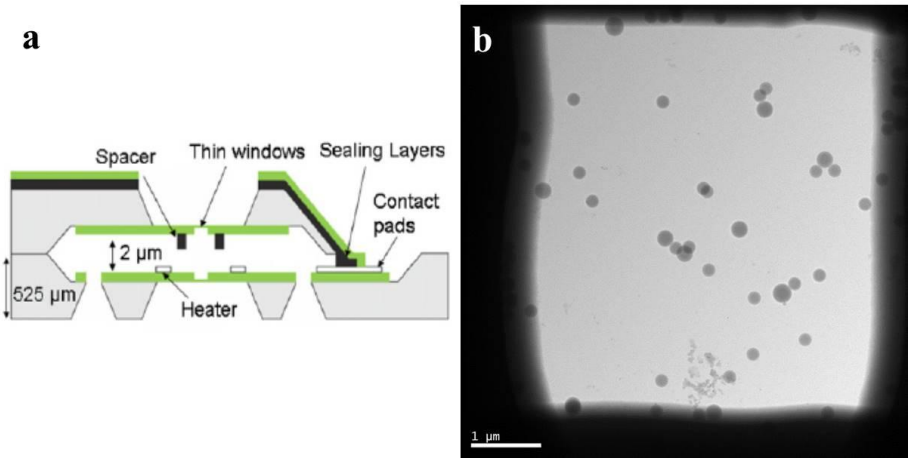

Figure 4.2. (a) The schematic cross-section of the WBNR. (b) TEM image of 0.25 µm polystyrene particles on one of the nanoreactor transparent windows.

The schematic cross section of the WBNR is shown in Fig. 4.2a. The WBNR has a channel height of 2 µm, which enables all different sizes of polystyrene particles to be loaded easily. After loading with 0.25 µm particles, the nanoreactor was studied under the TEM. Particles were found on the electron transparent windows (Fig. 4.2b). Unlike the SMNR, the pillars in the WBNR are not attached to the bottom wafer (in the WBNR the pillars are called spacers). This enables the

particles to flow along the channel without causing a “traffic jam”. In this nanoreactor, the spacers’ function is to prevent membrane collapse, which would permanently block the channel.

Subsequently, the nanoreactor was cleaned by soaking in toluene in order to dissolve the polystyrene particles. The following step was drying at room temperature. The cleaning procedure was proven to be effective since no polystyrene particles were found on the heater area after cleaning. The cleaned nanoreactor was used to study the flow of 0.5 μm and 1 μm particles. The same cleaning steps were performed in between all experiments. The particles could be successfully loaded into the nanoreactors. However, after loading, some bubbles were formed inside the nanoreactor (yellow circles in Fig. 4.3). But, over time, these bubbles disappeared and the complete nanoreactor area was covered with polystyrene particles. The bubbles seem to be due to remaining solution from the cleaning process, which apparently hasn’t evaporated completely.

The presence of the bubbles is unwanted during the loading because it can cause vortex flow in the channel, which disrupts the particle distribution. Furthermore, the areas inside the bubbles remain free of particles and large bubbles need longer time to disappear. After drying, no particles can be found in an area that contained bubbles during the loading. If the bubbles are on the transparent window area, they will decrease the probability of having particles available for the in-situ TEM imaging. Drying the pre-cleaned nanoreactor on a hot plate prevents bubble formation.

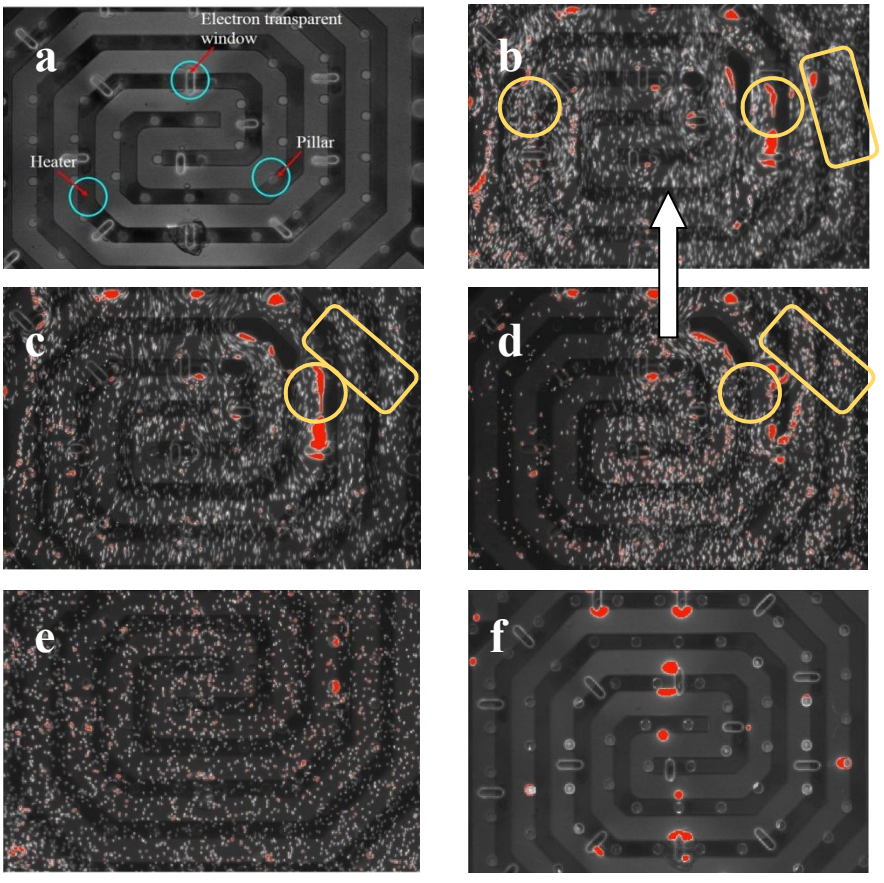

Figure 4.3. Sequential fluorescence images (bottom illumination and view) of the heater area during loading of 0.5 µm polystyrene particles into WBNR. (a) The nanoreactor heater area before loading and (b) soon after loading (white arrow is the flow direction). Yellow contours indicate bubbles (dark areas), red areas indicate high concentrations of particles in stagnant zones. (c, d) The bubbles start to disappear and (e) finally no bubbles are observed any more in this area. (f) The nanoreactor heater area after drying. Movie [4.3 (b-d)]

[4.3 (b-d)] https://www.youtube.com/watch?v=uQ8Ey00jmLw.

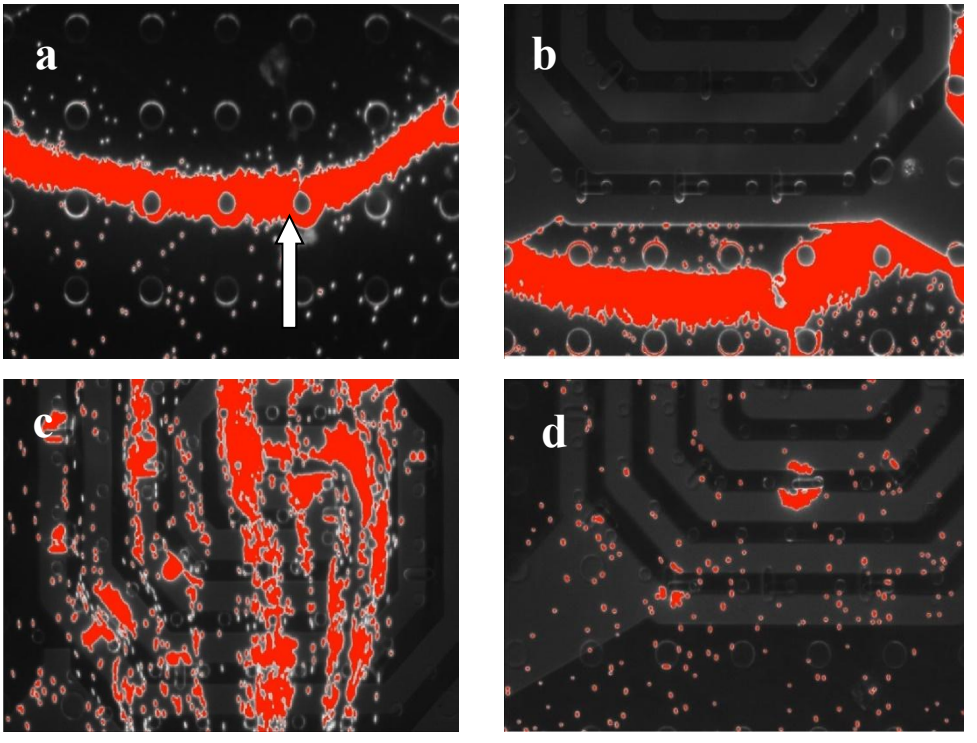

Figure 4.4. (a-d) Sequential fluorescence images (bottom illumination and view) of blockage during loading of 1 μm polystyrene particles into a WBNR. Red areas indicate high concentrations of beads in a stagnant zone; white arrow indicates the flow direction. Movies [4.4a], [4.4b], [4.4c], [4.4d].

[4.4a] https://www.youtube.com/watch?v=_2iwGw9ANyc.

[4.4b] https://www.youtube.com/watch?v=y-5JGCNezyw.

[4.4c] https://www.youtube.com/watch?v=woKZj-Myw4c.

[4.4d] https://www.youtube.com/watch?v=micPQqiEBP8.

During the loading of 1 µm particles, the particles tend to accumulate at the meniscus of the flow front, causing a blockage (Fig. 4.4). This phenomenon is caused by the slow penetration of the larger particles compared with the smaller particles. They also need longer to spread uniformly inside the nanoreactor. The particles accumulate in the area before the heater, but as a function of time the blockage is pushed forward to the heater area. Finally, the blockage is pushed forward completely and in the end the polystyrene flow becomes smooth.

The loading experiments with the SMNR started with loading of 0.25 µm polystyrene particles. The channel design of the nanoreactor is described in Fig. 4.5a. Figure 4.6 shows sequential fluorescence images during loading. The particles move very slowly because there are many pillars and plugs alongside the channel. A heavy "traffic jam" was observed near the inlet (Fig. 4.6b and c). The pillars function to increase the stiffness of the channel and reduce bulging when gas is loaded into the channel. But the placement of the pillars along the channel hampers the particle flow. Since the SMNR is built from a single die silicon wafer, some holes are created during the fabrication to enable the etching process of the nanoreactor interior. After the process is finished, the holes are closed with SiN_x by plasma enhanced chemical vapour deposition (PECVD). The cover layer is called the plug (Fig. 4.5b). The design of the plugs results in a small hole in the middle of the channel side of each plug, causing many of the particles to be trapped there. Only a small amount of the particles is released and continues with the flow of the liquid. But finally they get stuck before reaching the heater area, therefore no particles were found in the heater area (Fig. 4.6d-f).

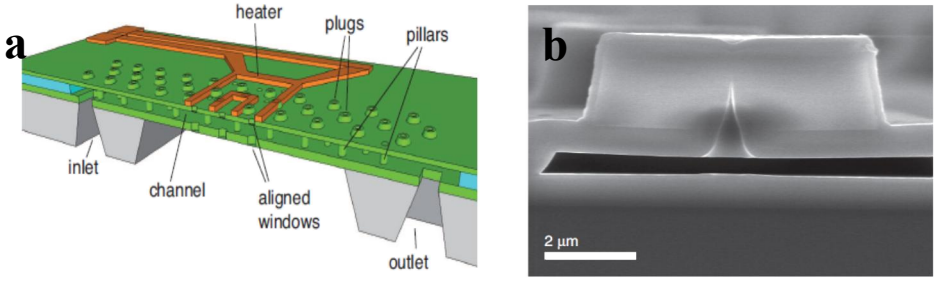

Figure 4.5. (a) The schematic design of the SMNR. (b) Cross section SEM image of a plug inside the nanoreactor.

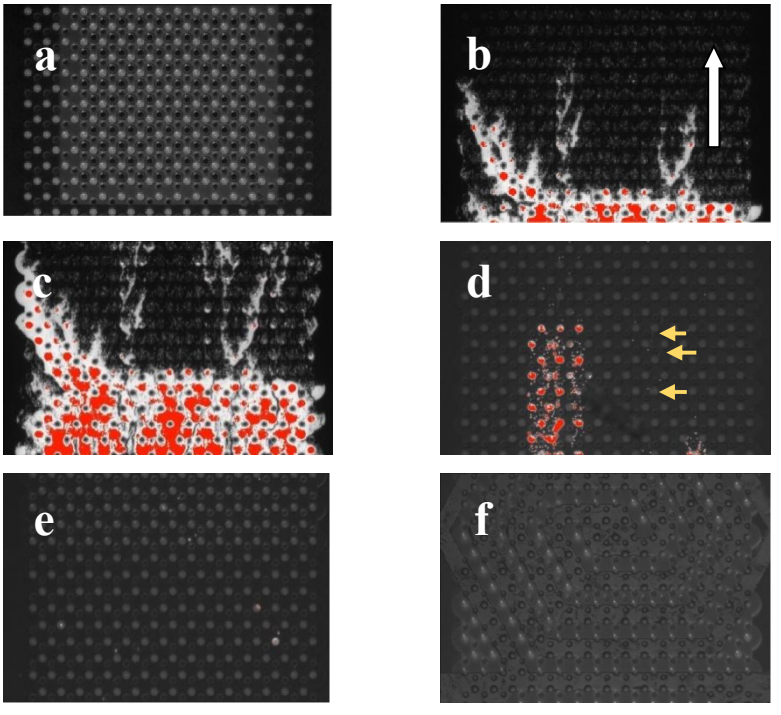

Figure 4.6. Sequential fluorescence images (bottom illumination and view) during loading of 0.25 µm (10%) of polystyrene particles into a SMNR. (a) The inlet area before loading and (b) the channel area near the inlet soon after loading (white arrow is the flow direction). (c) The "traffic jam" along the channel. (d) Some of the particles moved forward as seen in the image as white lines (yellow arrows) between the pillars. (e) The channel area near the heater and (f) the heater area after the loading process, no particles were found in these areas. Movies[4.6b], [4.6c], [4.6d].

[4.6b] https://www.youtube.com/watch?v=0p5rSsGjZdE.

[4.6c] https://www.youtube.com/watch?v=g1_rYvPi708.

[4.6d] https://www.youtube.com/watch?v=gEB3KAl3wEI.

The polystyrene particle suspension was then diluted to 2% (v/v) to obtain a lower concentration. The dilution process was proven to be effective to solve the traffic jam problem. The particles moved smoothly through the nanoreactor channel and reached the outlet very fast. After cleaning, the nanoreactor was used to study the flow of a 0.5 μm particle suspension (2% v/v). The suspension flow was smooth and no traffic jams were observed, which proved that the SMNR channel height was more than 0.5 μm. Figure 4.7 shows the process in sequential images.

Knowledge about the drying process is important to explain the particle distribution over the nanoreactor. In this experiment, the drying process was performed under irradiation by the microscope light. Figure 4.8 shows the drying process after the suspension loading. The dry area was filled with gas and a liquid-gas meniscus was formed. Evaporation also happened at the nanoreactor inlet and outlet. The liquid-gas menisci from the inlet and outlet eventually merged as the drying process along the nanoreactor channel completed. The liquid movement dragged along the particles through the nanoreactor channel, which then ended up at the inlet and outlet. Therefore, sometimes only small amounts of particles are found in the heater area and many particles are found at the inlet and outlet.

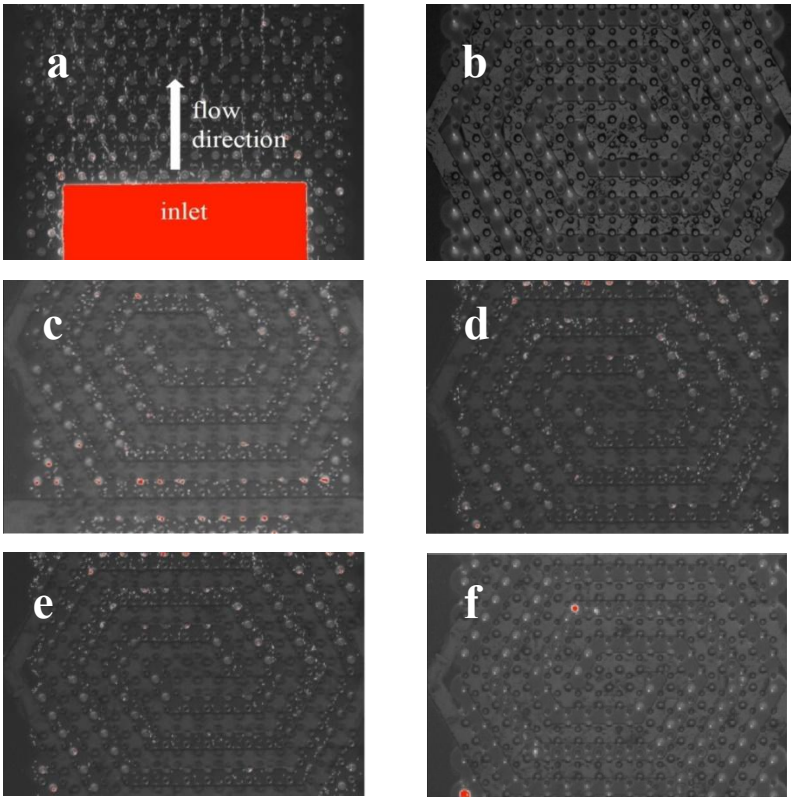

Figure 4.7. Sequential fluorescence images (bottom illumination and view) during loading of a 2% (v/v) suspension of 0.5 µm polystyrene particles into a SMNR. (a) The inlet area directly after loading. The polystyrene particles are white dots that move forward to the outlet. (b) The heater area before loading and (c) soon after the loading. (d, e) The heater area during loading and (f) after drying. Some of the particles are found in this area (red dots). Movies[4.7a], [4.7c], [4.7d-e]

[4.7a] https://www.youtube.com/watch?v=mBOaGnhahhE.

[4.7c] https://www.youtube.com/watch?v=Dbs81iatM9Q.

[4.7d-e] https://www.youtube.com/watch?v=A8jnR1FWClQ.

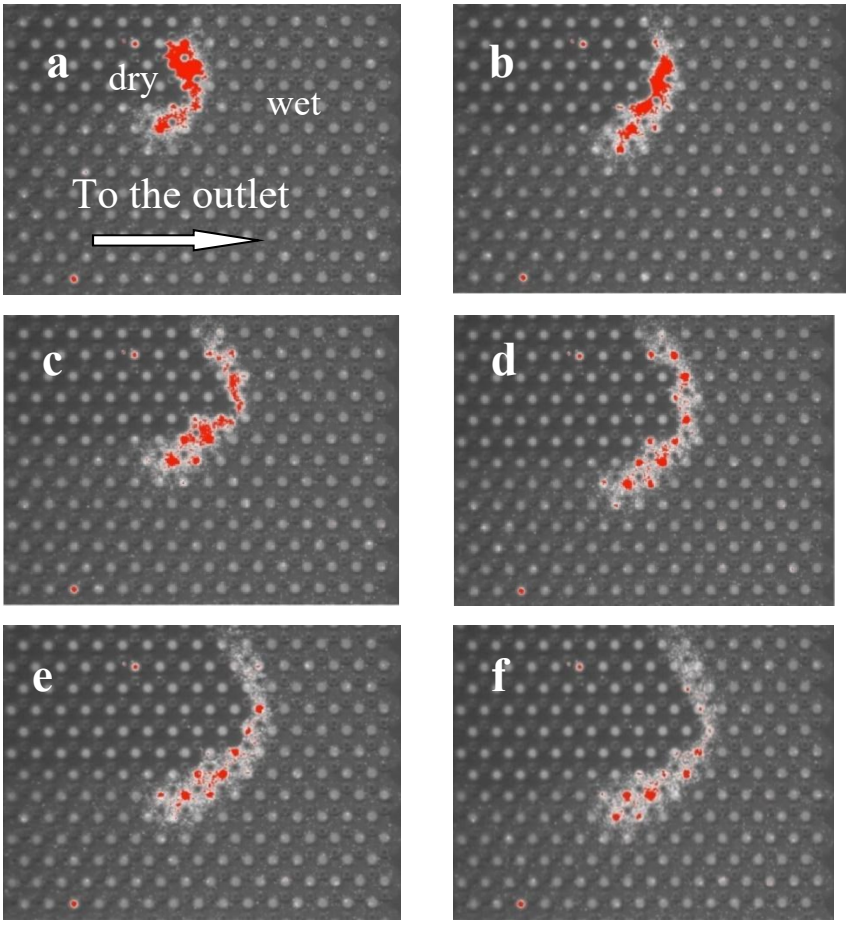

Figure 4.8. (a-f) Sequential fluorescence images (bottom illumination and view) of the drying process in the SMNR channel (near outlet). Movie[4.8a-f].

[4.8a-f] https://www.youtube.com/watch?v=wJMo552HmeY.

Even though a lower suspension concentration solves the loading problem for the SMNR, the low suspension concentration is less favourable since it will give a lower probability of finding catalyst particles inside the nanoreactor. This loading issue led to the development of a new type of nanoreactor that has a similar design as the previous SMNR. But instead of having a channel height of 0.5 μm, the new nanoreactor has a channel height of 4.5 μm. This improvement makes the loading process easier. Figure 4.9a is the fluorescence microscope image of a heater area that shows the arrangement of the 41 windows, the heater and the pillar positions inside the nanoreactor. During the fabrication, an incomplete etching process will result in closed or not transparent windows that cannot be used for imaging under the TEM. The perfect etching process will result in circular transparent windows. The window defects can be determined under the fluorescence microscope and TEM. Figure 4.9b shows a TEM image where only 14 windows are open, confirming the image from the fluorescence microscope.

A preliminary check in the TEM of all the windows before the in-situ TEM experiments is important to make sure sufficient particles are available for the experiments. All the nanoreactor windows were checked before and after loading. This procedure is also to check for problems such as window defects and impurities present in the nanoreactor before loading.

Figure 4.9c shows the drying process viewed in top illumination and bottom view configuration. The liquid front can be seen clearly and as the drying process continues, the liquid front moves towards both inlet and outlet.

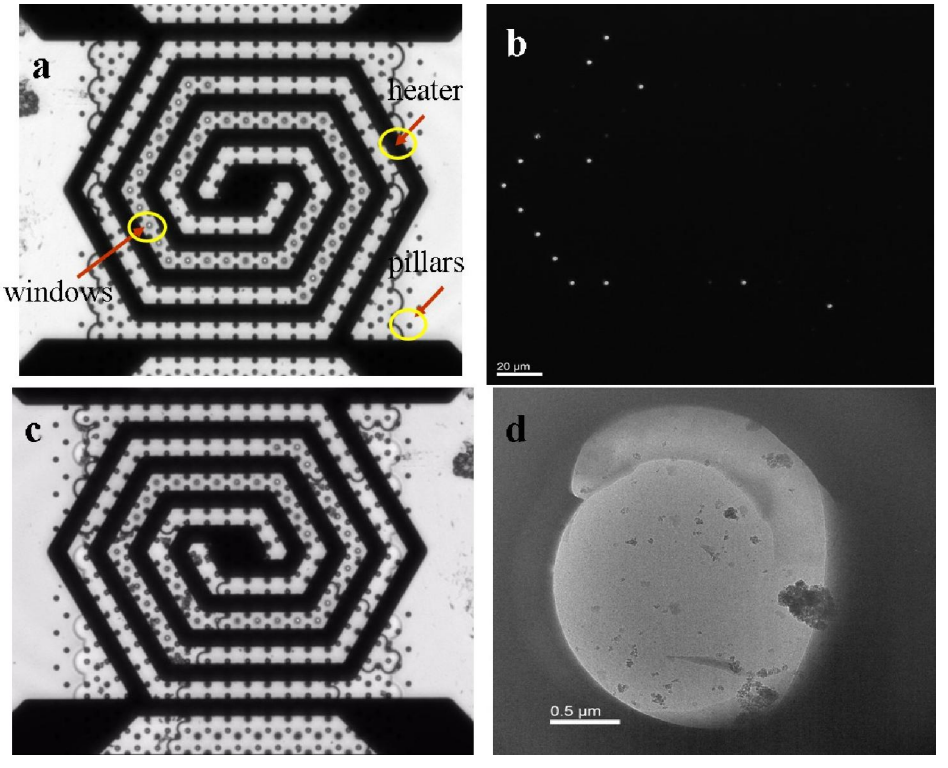

Figure 4.9. (a) Fluorescence image (top illumination and bottom view) of the SMNR heater area showing the transparent windows arrangement, heater and pillar positions. (b) TEM image showing 14 properly etched (transparent) windows out of 41 windows on SMNR. (c) Fluorescence image (top illumination and bottom view) of the drying process in the heater area after polystyrene loading. (d) TEM image of Pt/Al_2O_3 catalyst particles through one of the SMNR windows.

Based on the results, a Pt/Al_2O_3 catalyst was loaded into this last type of SMNR. The suspension was prepared by grinding the Pt/Al_2O_3 catalyst into very fine powder. Ethanol was added to suspend the powder. The suspension was then centrifuged at 2000 rpm for 5 min. The top liquid suspension part of the centrifuged sample, which contains the smallest particles, was taken for loading.

Bigger particles at the bottom of the centrifuged sample could hence be excluded from loading, avoiding blockage of the nanoreactor channel. The suspension preparation step is very important to get enough particles inside the nanoreactor. A

too high suspension concentration may cause nanoreactor channel blocking while a too low concentration may lead to a situation that there are no particles found on the nanoreactor transparent windows.

If needed, the loading process can be repeated, but this can cause channel, inlet or outlet blockage due to particle agglomeration. Before being loaded, the catalyst suspension should be ultrasonicated for 10 minutes to break particle agglomerates in the suspension. A TEM image of the loaded Pt/Al_2O_3 catalyst is shown in Fig. 4.7d. Some particles present on the transparent window prove that even though the drying process swept along the big particles to the inlet and outlet, the small particles stayed on the windows. In terms of the nanoreactor fabrication process, the electron transparent windows are not perfectly etched but the transparent area is wide enough to perform TEM imaging, making the nanoreactor suitable for in-situ TEM experiments.

4.4 Conclusions

Flow imaging using fluorescence microscopy is a suitable technique to study the flow of particle suspensions inside microchannels during loading of the in-situ TEM nanoreactors. Ethanol based monodisperse polystyrene suspensions (0.25, 0.5, 1 μm polystyrene particle size) were successfully loaded into the different in-situ TEM nanoreactors. Drying of these suspensions showed that many particles were dragged away during the liquid evaporation and ended up at the inlet and outlet of the nanoreactors, instead of staying at the heater area on the electron transparent windows. Nevertheless, some particles can still be found on the transparent windows. Polystyrene inside the nanoreactor can be removed by soaking the nanoreactor in toluene, flushing and then drying on a hot plate to prevent bubble formation. Cleaned nanoreactors can be re-used for other loading tests.

For the in-situ TEM experiments, the catalyst suspension preparation is important to get enough catalyst particles inside the nanoreactor and on the TEM transparent windows. During the loading, catalyst particles tend to agglomerate causing blockage at the inlet, outlet or along the nanoreactor channel.

These flow visualisation studies help to understand the suspension behavior inside the nanoreactor channel and the development of in-situ TEM nanoreactors that can be used to study real changes of catalyst particles during catalytic reactions.

4.5 References

1 Almeida, A. R., Moulijn, J. A. & Mul, G. In situ ATR-FTIR study on the selective photo-oxidation of cyclohexane over anatase TiO_2. *J. Phys. Chem. C* **112**, 1552-1561, (2008).

2 De Smit, E., Swart, I., Creemer, J. F., Hoveling, G. H., Gilles, M. K., Tyliszczak, T., Kooyman, P. J., Zandbergen, H. W., Morin, C., Weckhuysen, B. M. & De Groot, F. M. F. Nanoscale chemical imaging of a working catalyst by scanning transmission X-ray microscopy. *Nature* **456**, 222-225, (2008).

3 Dent, A. J., Diaz-Moreno, S., Evans, J., Fiddy, S. G., Jyoti, B. & Newton, M. A. In situ monitoring of oxide-supported platinum-group metal catalysts by energy dispersive EXAFS. *Phys. Scripta T* **T115**, 72-75, (2005).

4 Hendriksen, B. L. M. & Frenken, J. W. M. CO Oxidation on Pt(110): Scanning Tunneling Microscopy Inside a High-Pressure Flow Reactor. *Phys. Rev. Lett.* **89**, 046101, (2002).

5 Baker, R. T. K. In Situ Electron Microscopy Studies of Catalyst Particle Behavior. *Catal. Rev.* **19**, 161-209, (1979).

6 Gai, P. L. Environmental high resolution electron microscopy of gas-catalyst reactions. *Top. Catal.* **8**, 97-113, (1999).

7 Creemer, J. F., Helveg, S., Hoveling, G. H., Ullmann, S., Molenbroek, A. M., Sarro, P. M. & Zandbergen, H. W. Atomic-scale electron microscopy at ambient pressure. *Ultramicroscopy* **108**, 993-998, (2008).

8 Vendelbo, S. B., Elkjær, C. F., Falsig, H., Puspitasari, I., Dona, P., Mele, L., Morana, B., Nelissen, B. J., Van Rijn, R., Creemer, J. F., Kooyman, P. J. & Helveg, S. Visualization of oscillatory behaviour of Pt nanoparticles catalysing CO oxidation. *Nat. Mater.* **13**, 884-890, (2014).

9 Baker, R. T. K. & Harris, P. S. Controlled atmosphere electron microscopy. *J. Phys. E.* **5**, 793, (1972).

10 Boyes, E. D., Gai, P. L. & Hanna, L. G. Controlled environment [ECELL] TEM for dynamic in-situ reaction studies with HREM lattice imaging. *Mater. Res. Soc. Symp. Proc.* ***404****, (Cambridge Journals Online, 1996), 53-60.*

11 Giorgio, S., Sao Joao, S., Nitsche, S., Chaudanson, D., Sitja, G. & Henry, C. R. Environmental electron microscopy (ETEM) for catalysts with a closed E-cell with carbon windows. *Ultramicroscopy* **106**, 503-507, (2006).

12 Kamino, T., Yaguchi, T., Konno, M., Watabe, A., Marukawa, T., Mima, T., Kuroda, K., Saka, H., Arai, S., Makino, H., Suzuki, Y. & Kishita, K. Development of a gas injection/specimen heating holder for use with transmission electron microscope. *J. Electron Microsc.* **54**, 497-503, (2005).

13 Li, P., Liu, J., Nag, N. & Crozier, P. A. Atomic-scale study of in situ metal nanoparticle synthesis in a Ni/TiO_2 system. *J. Phys. Chem. B* **109**, 13883-13890, (2005).
14 Chenna, S. & Crozier, P. A. In situ environmental transmission electron microscopy to determine transformation pathways in supported Ni nanoparticles. *Micron* **43**, 1188-1194, (2012).
15 Mele, L., Santagata, F., Pandraud, G., Morana, B., Tichelaar, F. D., Creemer, J. F. & Sarro, P. M. Wafer-level assembly and sealing of a MEMS nanoreactor for in situ microscopy. *J. Micromech. Microeng.* **20**, (2010).
16 Creemer, J. F., Santagata, F., Morana, B., Mele, L., Alan, T., Iervolino, E., Pandraud, G. & Sarro, P. M. An all-in-one nanoreactor for high-resolution microscopy on nanomaterials at high pressures. *Proc. IEEE Micr. Elect.*, (2011) 1103-1106, ISBN: 978-1-4244-9632-7.
17 Creemer, J. F., Zandbergen, H. W. & Sarro, P. M. Microreactor for a transmission electron microscope and heating element and method of manufacture thereof. *US Patent 01795118 A1*, (2008).
18 Sharma, D. K., King, D., Oma, P. & Merchant, C. Micro-flow imaging: Flow microscopy applied to sub-visible particulate analysis in protein formulations. *AAPS J.* **12**, 455-464, (2010).
19 Hoffmann, D., O'Brien, J., Brennan, D. & Loughran, M. Optically encoded silicon microbeads: Detection and characterisation in a microfluidic system. *Sensors Actuat. B: Chem.* **122**, 653-658, (2007).
20 Kühn, S., Phillips, B. S., Lunt, E. J., Hawkins, A. R. & Schmidt, H. Ultralow power trapping and fluorescence detection of single particles on an optofluidic chip. *Lab Chip* **10**, 189-194, (2010).
21 Lima, R., Wada, S., Tanaka, S., Takeda, M., Tsubota, K., Ishikawa, T. & Yamaguchi, T. in *World Congress on Medical Physics and Biomedical Engineering 2006* Vol. 14 *IFMBE Proc.* (eds. R. Magjarevic & J. H. Nagel) Ch. 79, 283-286 (Springer Berlin Heidelberg, 2007). ISBN: 978-3-540-36839-7.
22 Rao, A. N., Rodesch, C. K. & Grainger, D. W. Real-time fluorescent image analysis of DNA spot hybridization kinetics to assess microarray spot heterogeneity. *Anal. Chem.* **84**, 9379-9387, (2012).
23 Hornbæk, T., Dynesen, J. & Jakobsen, M. Use of fluorescence ratio imaging microscopy and flow cytometry for estimation of cell vitality for Bacillus licheniformis. *FEMS Microbio. Lett.* **215**, 261-265, (2002).
24 Westerweel, J., Elsinga, G. E. & Adrian, R. J. Particle image velocimetry for complex and turbulent flows. *Ann. Rev. Fluid Mech.* **45**, 409-436, (2013).
25 Jeon, J., Watanabe, S., Tanishima, M., Sugimoto, F. & Ogle, B. Organic Contamination on Si Wafers in Fab Environments and its Effects on Gate

Oxide Integrity. *Silicon nitride and silicon dioxide thin insulating films, Proceedings of the fifth International Symposium*, 250-259, (Electrochemical Society Inc., New Jersey, 1999), ISBN: 1-56677-228-1.

5 Au Capping Agent Removal at Mild Temperature Conditions

5.1 Introduction

Synthesis of metallic nanoparticles has been the subject of intensive research due to their potential interesting applications[1]. These particles can be applied in chemical and biological fields such as nanoparticles for catalysis, chemical sensors, drug delivery, bio-sensing, etc.[2-4]. In the preparation of metal nanoparticles, capping agents are commonly used[5-7]. The function of the capping agent is to avoid aggregation of the nanoparticles in the solution and to control the size as well as the shape of the nanoparticles[8-11]. The size and shape of the nanoparticles are important factors in catalytic activity and selectivity. At the end of the preparation steps, the capping agent is still attached to the surface of the nanoparticles.

When the metal nanoparticles are used in catalytic reactions, the presence of the capping agent can affect the catalytic activity and selectivity because it hinders the chemical and physical access to the metal particle surface, and modifies the surface chemistry of the metal surface[12]. Therefore, methods to remove the capping agents are important issues. Washing with chemicals (acid, base or salt solution)[13-15], calcination[16-19], and combination of UV and ozone treatments[20-23] have been reported to remove the capping agents. But these techniques require special equipment and sometimes the morphology of the nanoparticles is not preserved due to harsh treatment conditions. Clearly, low temperature capping agent removal is important to prevent agglomeration of the nanoparticles.

Ozone has been used to remove unwanted organic compounds from inorganic surfaces[24,25]. In this method, a sample is contacted with an oxygen/ozone mixture at a certain temperature where ozone decomposes into atomic oxygen and radical species, which are highly reactive[26,27]. Kuhn et al. used ozone treatment at 200 ^{o}C to remove the DD3R template from zeolites in a 38 h detemplation process[24]. In comparison with the ozone treated samples, the synthesised samples were also calcined at 550-700 ^{o}C for 6-16 h. They reported that the porosity characteristics of the ozone treated samples were equal to those of the calcined samples, which verifies that the ozone treatment at low temperature is a powerful detemplation method.

In the 1980s, Haruta showed that oxide-supported gold nanoparticles with particle size smaller than 5 nm have a remarkable catalytic activity even at low temperatures. Since then gold nanoparticles have been recognised as catalysts for

many reactions, including oxidation of propene[28,29], CO oxidation[30], NO_x reduction[31,32], selective hydrogenation of acetylene[33,34], and the water-gas shift reaction[35,36]. Gold nanoparticles have been successfully prepared using several capping agents. Dodecylamine (DDA) is one of the most commonly used capping agents[37-39] and has been used for the current study. The capping agent removal was performed by an ozone treatment[12].

CO oxidation is one of the structure-sensitive catalytic reactions that is widely used to test the activity of gold catalysts. The rate and selectivity of this reaction are defined by three factors: the size and structure of the Au nanoparticles and the selected support[40]. Clearly, the Au catalyst preparation is an important step. In this investigation, the gold nanoparticles were prepared using a colloidal method and deposited on γ-Al_2O_3 support at room temperature condition. With this route, the desired particle size and shape were obtained. The γ-Al_2O_3, which was chosen as the support material, is expected to have an influence on the activity[12,41].

In this chapter, we report on the DDA capping agent removal from the surface of Au nanoparticles by ozone treatment in relation to their catalytic performance. The experiments were conducted at mild conditions to prevent structural and morphological changes as well as agglomeration of the nanoparticles. Catalyst characterisation was performed using Transmission Electron Microscopy (TEM), Fourier Transform Infrared Spectroscopy (FTIR), and X-ray Photoelectron Spectroscopy (XPS). CO oxidation and selective oxidation of benzyl alcohol to benzaldehyde were selected to study the catalytic performance before and after capping agent removal in a gas phase and a liquid phase reaction.

5.2 Experimental methods

Catalyst preparation

The gold catalysts were prepared following the methodology described by Chen[7] and Quintanilla[12]. 0.75 g of DDA (99.5% Sigma-Aldrich) was dissolved in 25 mL of cyclohexane (anhydrous, 99.5% Sigma-Aldrich). Then 6 mL of formaldehyde solution (37 wt% in water, 10-15% methanol as stabiliser, Sigma-Aldrich) was added to the mixture. The mixture was then stirred at room temperature for 30 minutes. The reaction of the mixture is described in the mechanism as shown in Figure 1.

Two phases of suspensions were separated by decantation. The top phase (transparent) was the cyclohexane phase and contained the desired

dodecylaminomethanol. The bottom phase (white) was the water phase, also containing the excess formaldehyde. Then 10 mL of 4 g/L $HAuCl_4$ (0.04 g $HAuCl_4$ (Sigma-Aldrich) in 10 mL of Milli-Q water) was added into the cyclohexane phase under stirring at room temperature. Soon after addition, the suspension colour turned yellow. The $-NHCH_2OH$ was oxidised to -NHCOOH by Au^{3+} which at the same time was reduced to Au^0. The -NHCOOH was not stable and decomposed into $-NH_2$ and CO_2. Then the $-NH_2$ was released and adsorbed on the Au^0 nanoparticle surface. After stirring for at least 1 h, the colour changed to ruby red, indicating the formation of small gold particles.

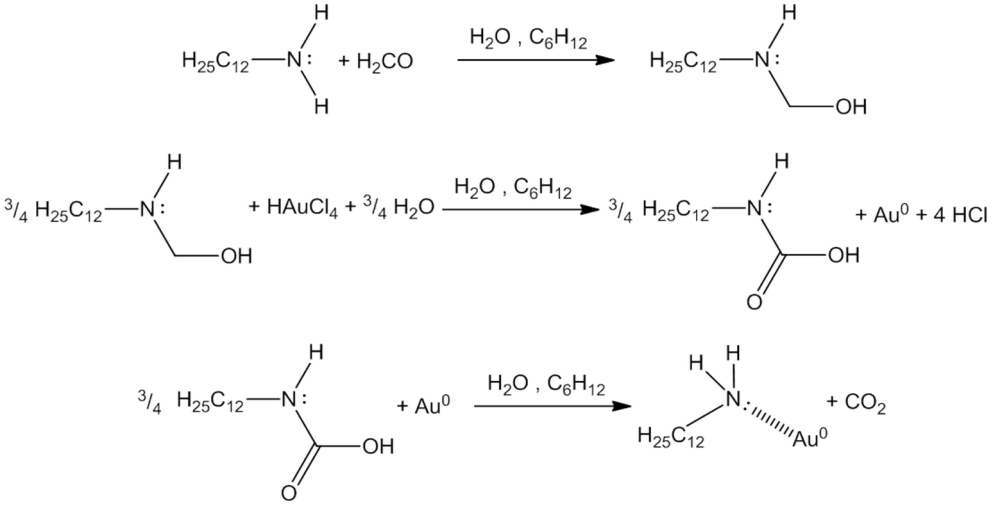

Figure 1. Au-DDA formation mechanism.

The mixture had two separated phases. The top part (ruby red colour) was the cyclohexane phase, which contained the Au-DDA, and the bottom part was the water phase. The suspension was left overnight in a separator funnel until the separation of the two phases was completed. The result was a ruby red suspension of Au-DDA colloid in cyclohexane. The Au-DDA colloid was washed using acetone. The acetone (about 3x the colloid volume) was added to the colloid suspension, and then the mixture was centrifuged for 5 minutes at 10,000 rpm to precipitate the nanoparticles. After the supernatant was removed, the nanoparticles were redispersed in 25 mL of cyclohexane. The Au nanoparticles were immobilised on γ-Al_2O_3. 1.5 g γ-Al_2O_3 (previously calcined at 500 ^oC, 6 h, < 7.1 µm, Akzo Chemical) was added to the cyclohexane mixture under vigorous stirring. The stirring was left overnight. The suspension was filtered resulting in a

pink catalyst powder (Au-DDA/γ-Al_2O_3). The powder was washed with 100 mL cyclohexane and 100 mL acetone, then left to dry in a vacuum desiccator at room temperature overnight.

DDA/γ-Al_2O_3 was also prepared for blank experiments. 0.9 g DDA was dissolved in 25 mL cyclohexane. 0.9 g γ-Al_2O_3 was then added to the mixture and stirred overnight. The suspension was filtered and left to dry overnight in a vacuum desiccator.

Capping agent removal

The removal of the capping agent from the supported catalyst was conducted by loading the 1% Au-DDA/γ-Al_2O_3 catalyst into a U-tube glass reactor, which was installed in the ozone detemplation setup (Fig. 5.2). Oxygen from a gas cylinder was passed through a Corona discharge ozone generator (A2Z Ozone Systems, SOZ -16GLAB). The check valves (CV1 and CV2) prevent back flow of the ozone to the mass flow controllers (MFC1 and MFC2). The ozone concentration at the outlet was monitored using an ozone detector (Lenntech, BMT 964), after which it was sent through a manganese dioxide / copper oxide catalytic ozone destructor. The U-tube glass reactor was placed inside the oven (Binder FP53) equipped with a temperature controller. The experiment was conducted at 30 ^{o}C while the ozone concentration was 7 g/Nm^3 (0.35%). The reaction time was varied from 6-10 h.

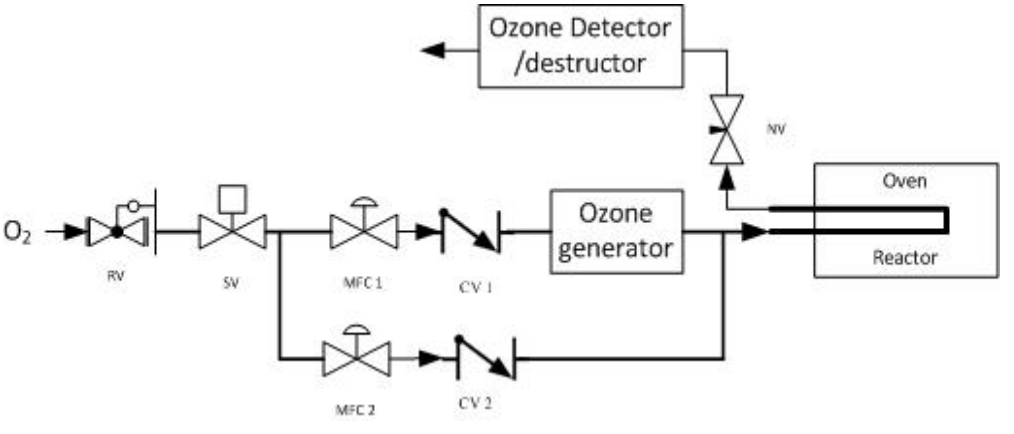

Figure 5.2. The flow scheme of the ozone setup.

Catalyst characterisation

The morphological characterisation of the gold catalysts was performed using an FEI TECNAI F20 transmission electron microscope (TEM) operated at 200 kV with a Field Emission Gun (FEG) and a Gatan ultra scan camera.

The samples were prepared by depositing one drop of washed gold colloid onto a microgrid Quantifoil® carbon film supported on a copper TEM grid and left to dry at room temperature. In case of the powder catalysts (as-synthesised Au-DDA/γ-Al_2O_3 and ozone treated catalyst), a finely crushed catalyst suspension in ethanol was used. A drop of the suspension was deposited on a Quantifoil® covered copper TEM grid and left to dry at room temperature. The particle size distributions and average particle sizes were determined from the TEM images by measuring the size of 300 particles from each sample.

The infrared spectra of the catalysts were recorded using a Thermo Scientific Nicolet Fourier Transform Infrared (FTIR) spectrophotometer. Prior to the FTIR characterisation, the background spectrum of the pure KBr pellet was recorded under He flow at room temperature. Then about 0.050 g catalyst was evenly spread on top of the KBr powder. The KBr background spectrum was automatically subtracted from the spectrum obtained from the measurement, resulting in the sample spectrum only. The catalyst oxidation states were studied using a Thermo Scientific K-Alpha X-ray photoelectron spectrometer (XPS). The measurements were done by using a line scan at four areas with each area having a spot size of 400 μm at ambient temperature and chamber pressure of about 10^{-7} mbar. The binding energy of the XPS spectra was calibrated using the C 1*s* peak (binding energy = 285.1 eV). The spectra were analysed and processed using Thermo Avantage v5.903 software (Thermo Fischer Scientific). The peaks were fitted using a Lorentzian-Gaussian product function. A Shirley type background was then subtracted from the spectra and the Au 4*f* spectra were deconvoluted.

Catalytic test

The CO oxidation reaction was chosen to test the catalyst activity. Approximately 25 mg catalyst (as-synthesised Au-DDA/γ-Al_2O_3 or ozone treated catalyst) was placed in a flow glass tube reactor (inner diameter ~0.4 mm, Fig. 5.3). The reactor was first loaded with SiC (~ 50 mg) then a mixture of catalyst (25 mg) and SiC (~100mg) was added on top of it. The dilution with SiC is to facilitate heat removal, preventing hot spots. The last layer was again SiC (~ 50 mg) and quartz wool. The gas mixture used in the experiment was 0.5% O_2, 1% CO and 98.5% He at 35 mL/min. The reactor was at a total pressure of 2 bar

during the test. The reaction temperature was increased fast (5 °C/min) from room temperature to 300 °C, then increased slowly (1 °C/min) from 300 °C to 500 °C. After maintaining the temperature at 500 °C for 1 h, the reactor was cooled down to 330 °C (1 °C/min). The setup was connected to a Chrompack CP 9001 GC equipped with a TCD detector, sampling every 12 minutes. Helium was used as carrier gas through a dual column system consisting of a Parabond Q column (Chrompack, 25 m in length, 0.53 mm in diameter and 10 µm of coating thickness) and a Molsieve 5A column (Chrompack 10 m in length, 0.53 mm in diameter and 50 µm of coating thickness). The CO oxidation using a reference catalyst (1% AUROlite™ from Strem Chemicals) and blank experiments (using γ-Al_2O_3 and DDA/γ-Al_2O_3) were also performed as comparison.

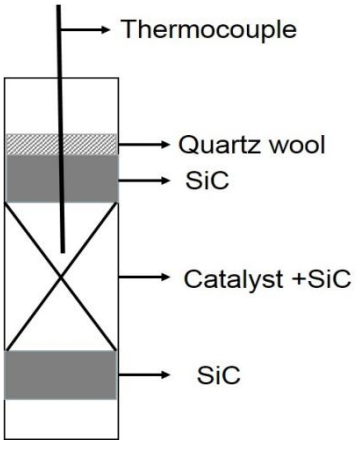

Figure 5.3. CO oxidation catalyst bed.

A reaction to evaluate catalytic performance in the liquid phase was the benzyl alcohol oxidation. In a round-bottom flask (60 mm inner diameter, equipped with baffles and stirrer shaft), approximately 0.6 g catalyst (as-synthesised Au-DDA/γ-Al_2O_3 or ozone treated catalyst) was mixed with 3.04 g K_2CO_3 (>99.0%, Sigma-Aldrich). 80 mL Toluene (anhydrous, 99.8% Sigma Aldrich) was added to disperse the mixture. The flask was stirred at 1200 rpm and heated to 80 °C. 200 mL/min of air was bubbled through the mixture. When the temperature was stable, 22 mmol (2.4 g) of benzyl alcohol was added (t = 0 min). Small samples of 300 µL were taken at recorded times and filtered from catalyst and K_2CO_3 powders with a 13 mm syringe Teflon filter of 0.2 µm pore size (diameter: 13 mm; pore size: 0.2 µm; PTFE membrane VWR international) and introduced in a GC sample vial together with 20 µL of tetradecane, the latter being used as internal standard.

They were analysed by a Varian CP-3380 GC equipped with FID. Helium was used as carrier gas through a CP-SIL 8 CB column (Chrompack) of 50 m in length, 0.25 mm in diameter and 0.25 μm of coating thickness. In the chromatograms, the main product (benzaldehyde) and the consecutive products (benzoic acid and benzyl benzoate) were detected in the product mixture. Previous work showed that no conversion of benzyl alcohol occurs over pure γ-Al_2O_3[12], therefore no blank experiment was performed.

The turnover frequency (*TOF*) was calculated as follows:

$$TOF = \frac{\Delta n_{BnOH}}{\Delta t} \times \frac{M_{Au}}{w_{cat} \times x_{Au}} \qquad \text{(Eq. 5.1)}$$

Where $\frac{\Delta n_{BnOH}}{\Delta t}$ is the benzyl alcohol reaction rate (mol/h), M_{Au} is the molar mass of gold (g/mol), w_{cat} is the amount of catalyst in the reactor (g), and x_{Au} is the gold loading of the catalyst (wt.%).

5.3 Results and discussion

Catalyst characterisation

The use of capping agent yields a uniform particle shape as shown in Fig. 5.4. The unwashed Au-DDA colloid showed severe carbon contamination under the TEM beam because the excess of DDA was still present in the colloid (Fig. 5.4a). The average particle size of the unwashed colloid is 3.3 nm (St.Dev. = 0.5). Figure 5.4b shows a TEM image and particle size distribution of the washed colloid. The average particle size is 3.8 nm (St.Dev. = 0.5). The inset in figure 5.4b shows that the Au nanoparticles are monocrystalline as reported by Quintanilla and coworkers[12]. As expected, the immobilisation of the catalyst on γ-Al_2O_3 support does not drastically change the particle size (Fig. 5.5a) because the gold particles had been produced before the deposition and the deposition process should not alter the particle sizes and distributions[41]. The average particle size of as-prepared supported particles and after capping agent removal using ozone treatment (Au-DDA/γ-Al_2O_3 (O_3, 8 h)) at 30 °C was 4.0 nm (St.Dev. = 0.8) and 4.3 nm (St.Dev. = 1.0) respectively (Fig. 5.5a-b). Even though the average particle size before and after ozone treatment are similar, the broadening of the particle size distribution after ozone treatment shows that some sintering occurred. However, since the ozone treatment is at mild temperature, the agglomeration is

less than at high temperatures[42]. For a sulphur-containing capping agent, Menard et al. showed a tripling of the nanoparticle size (from 0.8 to 2.7 nm) upon calcination at 400 °C, whereas the particle size increase was limited to 1.2 nm after ozone treatment[22]. Figure 5.5b (inset) shows lattice fringes on the Au nanoparticles, indicating that the ozone treatment does not change the Au nanoparticle crystallinity.

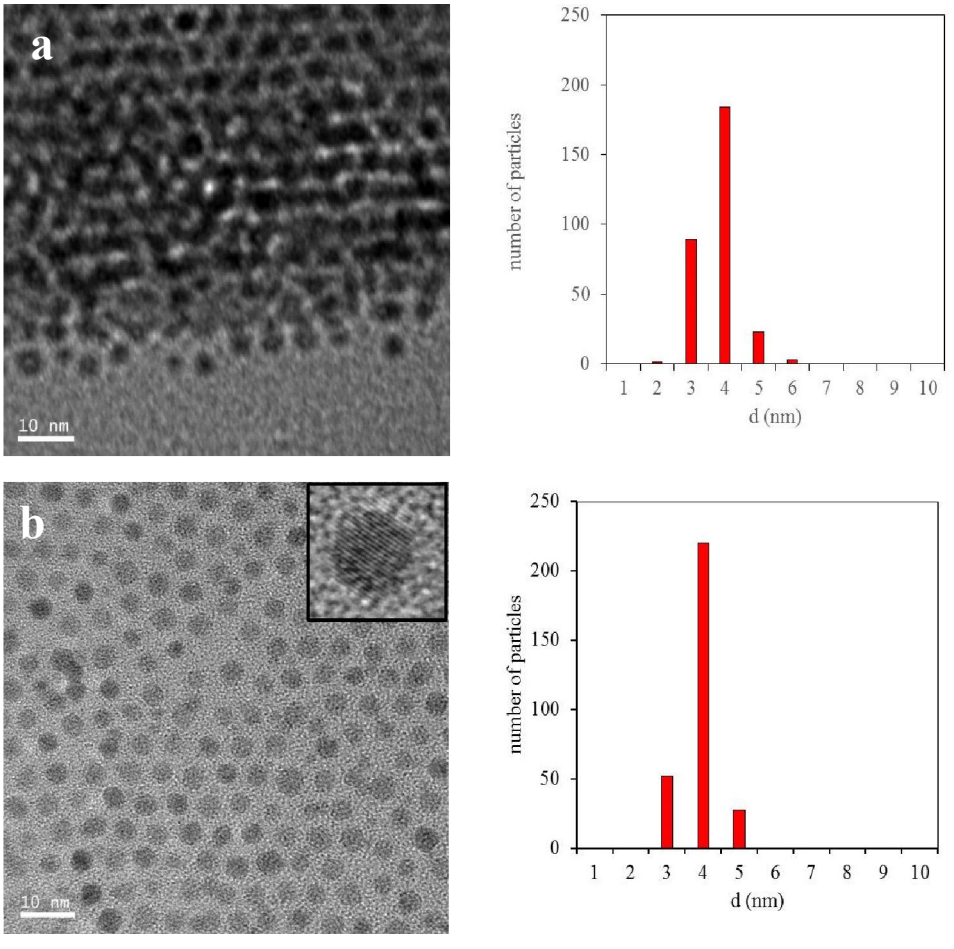

Figure 5.4. TEM images and particle distribution of (a) unwashed Au-DDA colloid and (b) washed Au-DDA colloid.

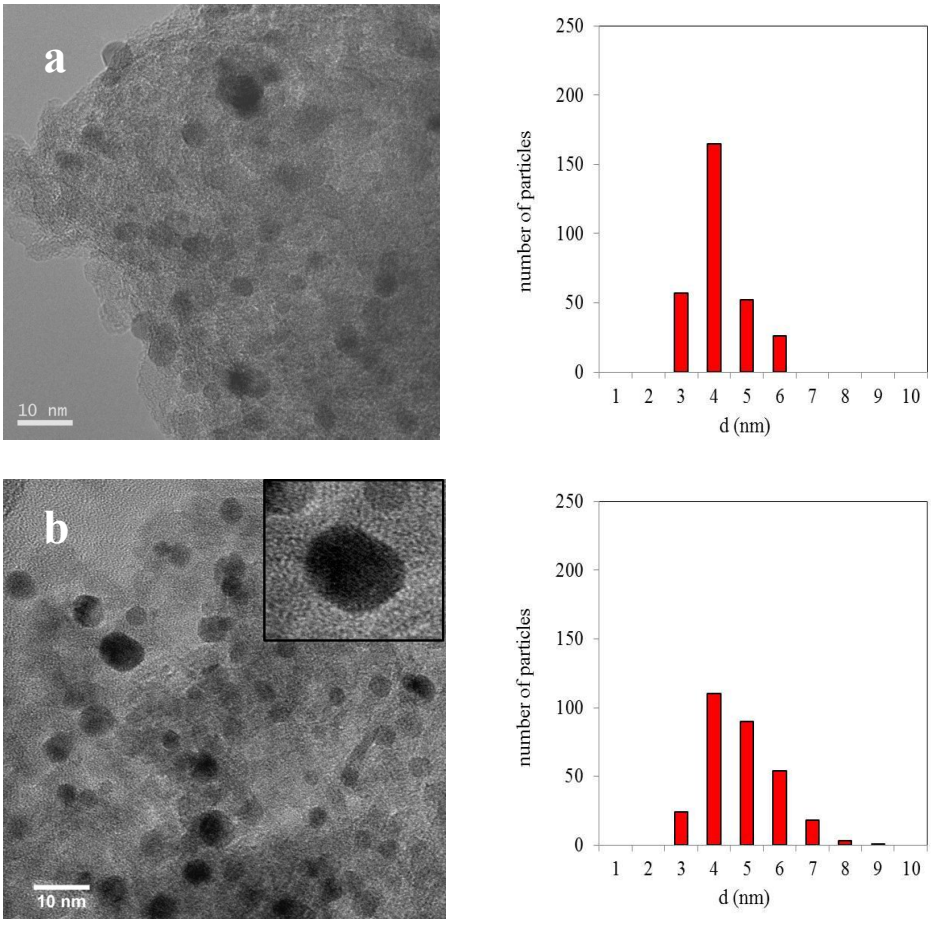

Figure 5.5. TEM images and particle size distribution of (a) as prepared Au-DDA/γ-Al_2O_3, (b) Au-DDA/γ-Al_2O_3 (O_3, 8 h, 30 °C).

The TEM images of the catalysts after CO oxidation (Fig. 5.6a-b) show that the high temperature CO oxidation caused sintering. However, the particle size does not change drastically. After use, the average particle size is 5.5 nm (St.Dev. = 1.9) for the as-prepared catalyst and 4.7 nm (St.Dev. = 1.3) for the ozone treated catalyst.

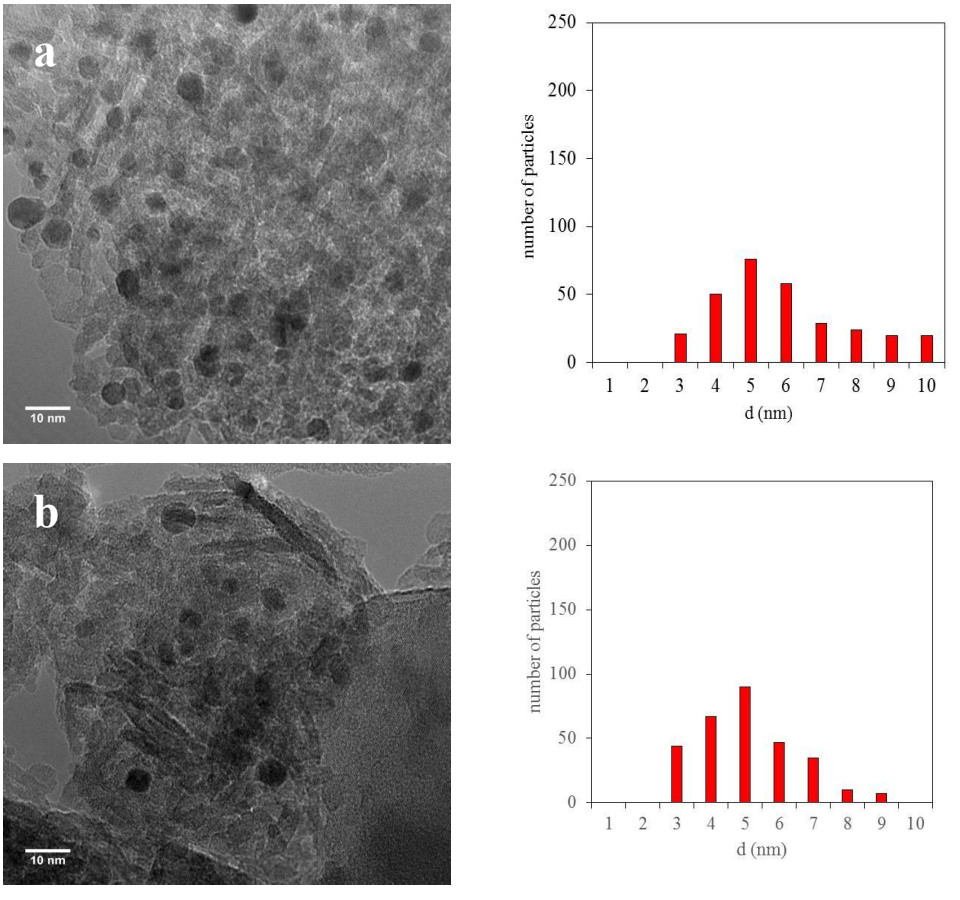

Figure 5.6. TEM images and particle size distribution of (a) as-prepared Au-DDA/γ-Al_2O_3 after CO oxidation and (b) Au-DDA γ-Al_2O_3 (O_3, 8 h) after CO oxidation.

Figure 5.7 shows infrared spectra of Au-DDA/γ-Al_2O_3 after different duration of ozone treatment. The changes in the absorbance below 1600 cm^{-1} are due to water vapour interactions on the surface of the γ-Al_2O_3 support. The DDA/γ-Al_2O_3 spectrum was used to determine the vibration energy signals of -CH_2- and -CH_3 groups from the DDA at the wavenumbers 2858 cm^{-1} and 2930 cm^{-1} [43,44] (Fig. 5.6a). The intensity of these peaks disappeared after 7 h of treatment, showing that the DDA has been removed. But to make sure that all of the DDA have been removed, 8 h of treatment was chosen as the experimental time to remove the DDA. Combining the information from TEM and FTIR, we conclude that DDA

has been removed from the surface of the Au nanoparticles after 8 h ozone treatment at 30 °C without drastically changing the diameter of the Au particles.

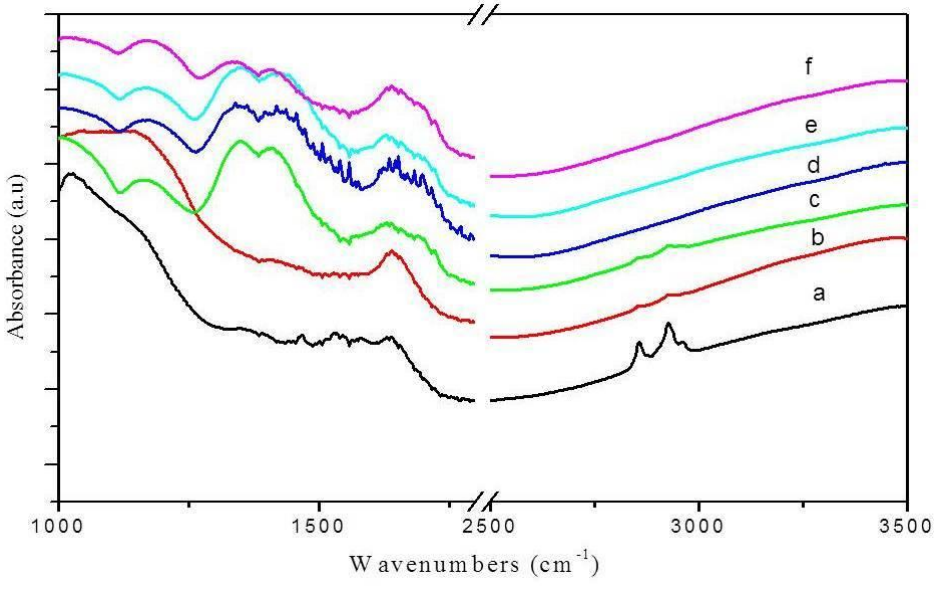

Figure 5.7. FTIR spectra of (a) DDA/γ-Al_2O_3, (b) Au-DDA/γ-Al_2O_3 as prepared, (c) after O_3 treatment at 30 °C for 6 h, (d) for 7 h, (e) for 8 h and (f) for 10 h.

XPS was used to study the oxidation state of the gold. Figure 5.8 shows the Au 4*f* photoelectron spectra from as-prepared Au-DDA/γ-Al_2O_3 and ozone treated catalysts. For the ozone treated catalyst, the peaks shifted to higher binding energies. The deconvolution of these peaks leads to the FWHM measurement which indicates that the Au in the as-prepared catalyst is metallic (Au^o, binding energy 836 and 871 eV), while after ozone treatment the Au is cationic ($Au^{\delta+}$, binding energy 841 and 878 eV). The results are in line with previous studies, which concluded that surfactant-encapsulated gold and platinum nanoparticles surface act as metals while supported nanoparticles are cationic[12,45-47].

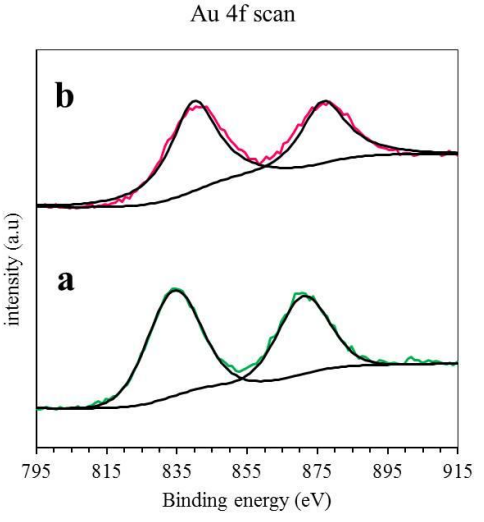

Figure 5.8. XPS spectra of the Au 4*f* binding energy region for (a) Au-DDA/γ-Al_2O_3 as prepared and (b) after O_3 treatment for 8 h (30 ^oC).

Catalytic tests

Figure 5.9 shows the CO conversion against temperature for several samples. The blank samples (γ-Al_2O_3 and DDA/γ-Al_2O_3) show very low conversion because the active phase for this reaction is the nanoparticulate Au, and the Au nanoparticle-support interface enhances the activity of the Au nanoparticles[40,48]. As expected the conversion increases after introduction of Au nanoparticles, but no significant conversion changes can be seen between the as-prepared Au-DDA/γ-Al_2O_3 and ozone treated catalysts. This can be explained by the similarity in Au particle size and crystallinity. The 1% AUROlite^{TM} catalyst (reference catalyst, average particle size 2-3 nm[49]) gives the highest CO oxidation activity. This result was due to the presence of chloride (from the Au precursor during catalyst preparation) on the surface of the Au nanoparticles which lowers the catalytic activity by stimulating the agglomeration of Au nanoparticles during the heat treatment (> 100 ^oC) and hinders the reduction of Au cations by poisoning[50-52]. Figure 5.10 shows the CO oxidation performance of the as-prepared Au-DDA/γ-Al_2O_3 and Au-DDA/γ-Al_2O_3 ozone treated for 8h catalysts during heating and cooling cycling. The CO conversion during cooling is slightly lower than during heating, which is attributed to some sintering, as witnessed by TEM observations.

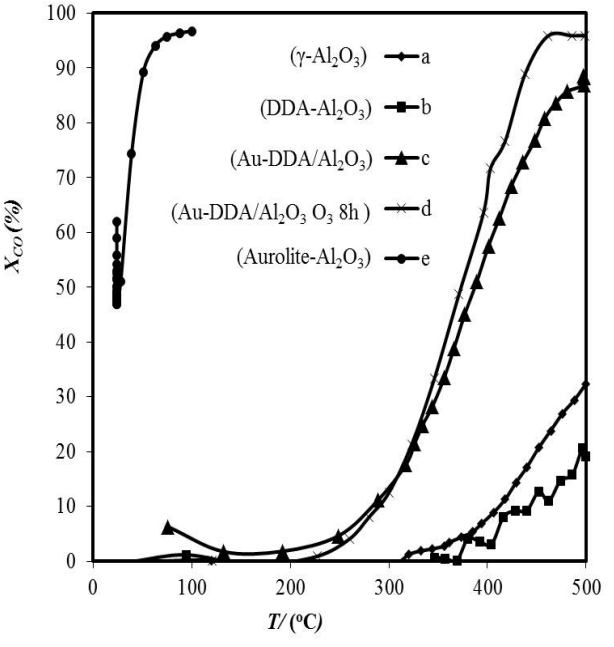

Figure 5.9. CO conversion versus temperature for (A) γ-Al_2O_3, (B) DDA/γ-Al_2O_3, (C) as-prepared Au-DDA/γ-Al_2O_3catalyst, (D) Au-DDA/γ-Al_2O_3 ozone treated for 8h and (E) AUROlite^{TM}.

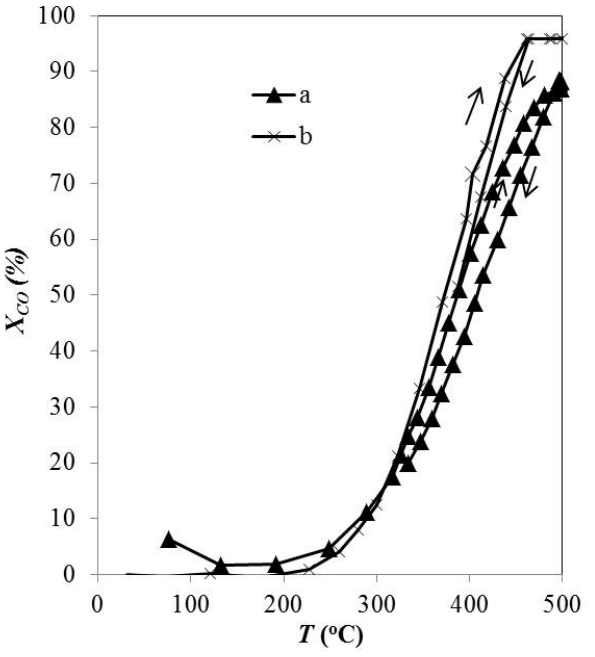

Figure 5.10. CO oxidation versus temperature during heating and cooling treatment (a) as-prepared Au-DDA γ-Al_2O_3 and (b) Au-DDA/γ-Al_2O_3 ozone treated for 8h.

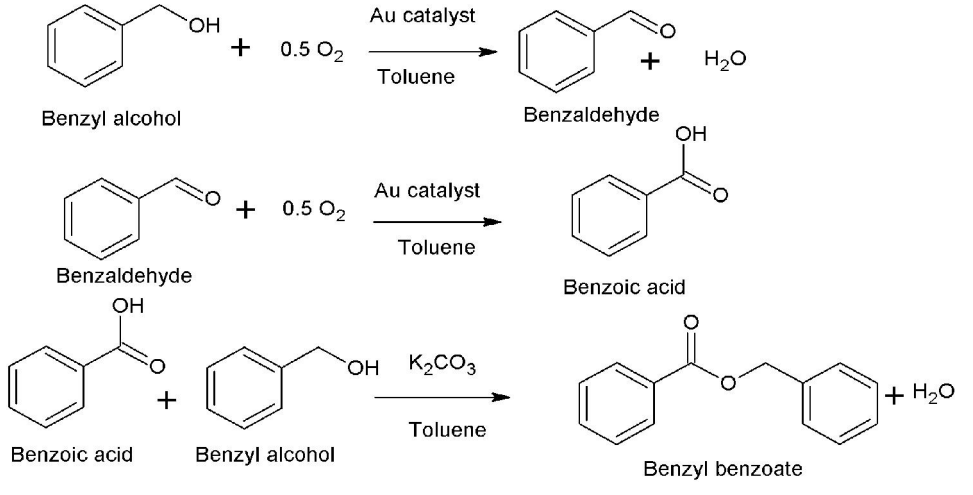

Figure 5.11. Benzyl alcohol oxidation pathways.

The benzyl alcohol oxidation mechanism is presented in Fig. 5.11. The main product is benzaldehyde while the side products, benzoic acid and benzyl benzoate, are formed in consecutive reactions. The as-prepared Au-DDA colloid is not active for this reaction while supported Au-DDA is slightly active as reported in a previous study[12]. This confirms the influence of a metal-support interaction, which contributes to the catalyst activity. After capping agent removal, the interaction is stronger, therefore the activity is slightly higher than for the as-prepared sample. Similar to the CO oxidation results, the as-prepared Au-DDA/γ-Al_2O_3 and the ozone-treated samples present a similar activity with *TOF* = 894 h^{-1} for Au-DDA/γ-Al_2O_3 and *TOF* = 1106 h^{-1} for Au-DDA/γ-Al_2O_3 O_3 8h. The benzyl alcohol conversions at 240 min are in the range of 65-70% (Fig. 5.12). For comparison, the benzyl alcohol conversion over AUROlite™ at 240 min is 78% and its TOF 682 h^{-1} [49].

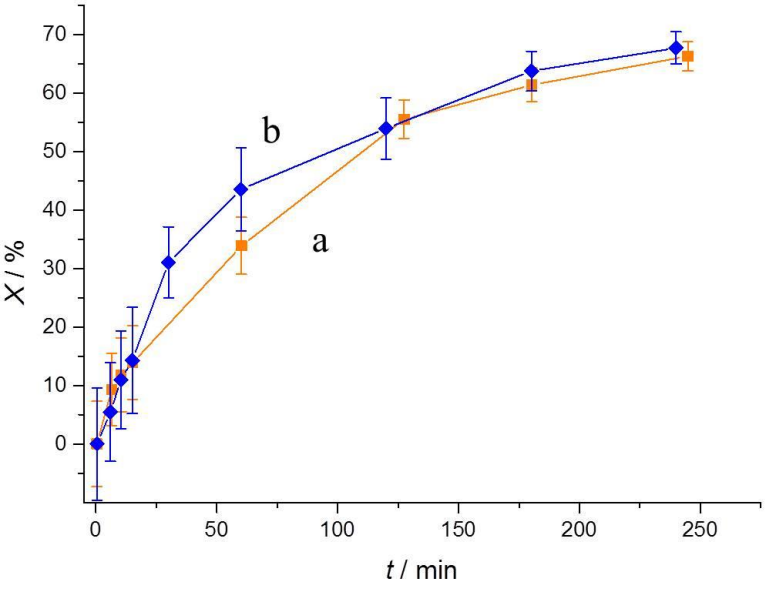

Figure 5.12. Benzyl alcohol conversion as a function of reaction time for (a) as-prepared Au-DDA/γ-Al_2O_3 catalyst and (b) Au-DDA/γ-Al_2O_3 O_3 8h catalyst.

The activity of the supported gold catalyst is often attributed to cationic gold species in the catalyst[12]. Quintanilla and coworkers reported that the Au-DDA colloid is not catalytically active, but after immobilisation it appears to be slightly active because some cationic Au species are formed. The alumina support induces the formation of cationic Au and more surface Au atoms. The concentration of the

cationic Au species in the catalyst is responsible for the activity of the catalyst during the catalytic reaction. The Au-DDA/γ-Al_2O_3 shows activity during CO oxidation and benzyl alcohol oxidation despite the XPS results showing that the Au is in the metallic state, which is also what Quintanilla et al. concluded[12]. The Au cationic species might also be present in small concentrations in the catalyst. Then it increases after ozone treatment, resulting in the shift of the XP spectrum and a slight increase of the catalyst activity.

5.4 Conclusions

Ozone treatment at mild temperature was shown to remove the capping agent from the surface of supported gold nanoparticles. The average particle size, shape and crystallinity of the gold nanoparticles were relatively preserved after the capping agent removal. Even so, some particles agglomerated with nearby particles. But since the capping agent removal occurred at mild temperature, the agglomeration process can be minimised. This leads to stability of the particles during selected catalytic reactions. The ozone treated catalysts did not sinter significantly during the high temperature CO oxidation reaction and benzyl alcohol oxidation. The activity of ozone-treated Au-DDA γ-Al_2O_3 was slightly increased compared to the as-prepared catalyst, probably due to the increased concentration of Au cationic species on the surface of the catalyst after the ozone treatment. Repeated catalytic test are needed to analyse the possibility of deactivation due to sintering on both catalyst samples.

5.5 References

1 Hutchings, G. J. & Haruta, M. A golden age of catalysis: A perspective. *Appl. Catal. A.* **291**, 2-5, (2005).

2 Bond, G. C., Louis, C. & Thompson, D. T. *Catalysis by Gold*. (Imperial College Press, 2006). ISBN: 978-1860946585.

3 Otieno, B. A., Krause, C. E., Latus, A., Chikkaveeraiah, B. V., Faria, R. C. & Rusling, J. F. On-line protein capture on magnetic beads for ultrasensitive microfluidic immunoassays of cancer biomarkers. *Biosens. Bioelectron.* **53**, 268-274, (2014).

4 Nagelli, E., Naik, R., Xue, Y., Gao, Y., Zhang, M. & Dai, L. Sensor arrays from multicomponent micropatterned nanoparticles and graphene. *Nanotechnology* **24**, (2013).

5 Lee, I., Morales, R., Albiter, M. A. & Zaera, F. Synthesis of heterogeneous catalysts with well shaped platinum particles to control reaction selectivity. *PNAS* **105**, (2008), 15241-15246, ISSN: ISSN-0027-8424.

6 Polavarapu, L. & Xu, Q. H. A simple method for large scale synthesis of highly monodisperse gold nanoparticles at room temperature and their electron relaxation properties. *Nanotechnology* **20**, (2009).
7 Chen, Y. & Wang, X. Novel phase-transfer preparation of monodisperse silver and gold nanoparticles at room temperature. *Mater. Lett.* **62**, 2215-2218, (2008).
8 Sun, Y., Mayers, B., Herricks, T. & Xia, Y. Polyol synthesis of uniform silver nanowires: A plausible growth mechanism and the supporting evidence. *Nano Lett.* **3**, 955-960, (2003).
9 Sun, Y. & Xia, Y. Shape-controlled synthesis of gold and silver nanoparticles. *Science* **298**, 2176-2179, (2002).
10 Bratlie, K. M., Lee, H., Komvopoulos, K., Yang, P. & Somorjai, G. A. Platinum nanoparticle shape effects on benzene hydrogenation selectivity. *Nano Lett.* **7**, 3097-3101, (2007).
11 Tao, A. R., Habas, S. & Yang, P. Shape control of colloidal metal nanocrystals. *Small* **4**, 310-325, (2008).
12 Quintanilla, A., Butselaar-Orthlieb, V. C. L., Kwakernaak, C., Sloof, W. G., Kreutzer, M. T. & Kapteijn, F. Weakly bound capping agents on gold nanoparticles in catalysis: Surface poison? *J. Catal.* **271**, 104-114, (2010).
13 Naresh, N., Wasim, F. G. S., Ladewig, B. P. & Neergat, M. Removal of surfactant and capping agent from Pd nanocubes (Pd-NCs) using tert-butylamine: Its effect on electrochemical characteristics. *J. Mat. Chem. A* **1**, 8553-8559, (2013).
14 Mazumder, V. & Sun, S. Oleylamine-Mediated Synthesis of Pd Nanoparticles for Catalytic Formic Acid Oxidation. *JACS* **131**, 4588-4589, (2009).
15 Nalajala, N., Gooty Saleha, W. F., Ladewig, B. P. & Neergat, M. Sodium borohydride treatment: A simple and effective process for the removal of stabilizer and capping agents from shape-controlled palladium nanoparticles. *Chem. Comm.* **50**, 9365-9368, (2014).
16 Lange, C., De Caro, D., Gamez, A., Storck, S., Bradley, J. S. & Maier, W. F. Polymer-Induced Selectivity Enhancement in the Hydrogenation of 2-Hexyne Catalyzed by Poly(vinylpyrrolidone)-Stabilized Platinum Colloids in an Amorphous Mixed Metal Oxide Support. *Langmuir* **15**, 5333-5338, (1999).
17 Yu, R., Song, H., Zhang, X. F. & Yang, P. Thermal Wetting of Platinum Nanocrystals on Silica Surface. *J. Phys. Chem. B* **109**, 6940-6943, (2005).
18 Joo, S. H., Park, J. Y., Tsung, C. K., Yamada, Y., Yang, P. & Somorjai, G. A. Thermally stable Pt/mesoporous silica core-shell nanocatalysts for high-temperature reactions. *Nat. Mater.* **8**, 126-131, (2009).

19 Kim, C., Min, M., Chang, Y. W., Yoo, K. H. & Lee, H. Chemical and thermal stability of Pt nanocubes synthesized with various surface-capping agents. *J. Nanosci. Nanotech.* **10**, 233-239, (2010).
20 Aliaga, C., Park, J. Y., Yamada, Y., Lee, H. S., Tsung, C. K., Yang, P. & Somorjai, G. A. Sum frequency generation and catalytic reaction studies of the removal of organic capping agents from Pt nanoparticles by UV-Ozone treatment. *J. Phys. Chem. C* **113**, 6150-6155, (2009).
21 Crespo-Quesada, M., Andanson, J. M., Yarulin, A., Lim, B., Xia, Y. & Lioubov, K. W. UV–Ozone Cleaning of Supported Poly(vinylpyrrolidone)-Stabilized Palladium Nanocubes: Effect of Stabilizer Removal on Morphology and Catalytic Behavior. *Langmuir* **27**, 7909-7916, (2011).
22 Menard, L. D., Xu, F., Nuzzo, R. G. & Yang, J. C. Preparation of TiO_2-supported Au nanoparticle catalysts from a Au_{13} cluster precursor: Ligand removal using ozone exposure versus a rapid thermal treatment. *J. Catal.* **243**, 64-73, (2006).
23 Niu, Z. & Li, Y. Removal and Utilization of Capping Agents in Nanocatalysis. *Chem. Mater.* **26**, 72-83, (2014).
24 Kuhn, J., Gascon, J., Gross, J. & Kapteijn, F. Detemplation of DDR type zeolites by ozonication. *Micropor. Mesopor Mat.* **120**, 12-18, (2009).
25 Heng, S., Lau, P. P. S., Yeung, K. L., Djafer, M. & Schrotter, J. C. Low-temperature ozone treatment for organic template removal from zeolite membrane. *J. Membrane Sci.* **243**, 69-78, (2004).
26 Benson, S. W. & Axworthy, A. E. Reconsideration of the rate constants from the thermal decomposition of ozone. *J. Chem. Phys.* **42**, 2614-2615, (1965).
27 Benson, S. W. & Axworthy Jr, A. E. Mechanism of the gas phase, thermal decomposition of ozone. *J. Chem. Phys.* **26**, 1727-1733, (1957).
28 Nijhuis, T. A., Sacaliuc, E., Beale, A. M., van der Eerden, A. M. J., Schouten, J. C. & Weckhuysen, B. M. Spectroscopic evidence for the adsorption of propene on gold nanoparticles during the hydro-epoxidation of propene. *J. Catal.* **258**, 256-264, (2008).
29 Delannoy, L., Fajerwerg, K., Lakshmanan, P., Potvin, C., Méthivier, C. & Louis, C. Supported gold catalysts for the decomposition of VOC: Total oxidation of propene in low concentration as model reaction. *Appl. Catal. B: Environ.* **94**, 117-124, (2010).
30 Valden, M., Lai, X. & Goodman, D. W. Onset of catalytic activity of gold clusters on titania with the appearance of nonmetallic properties. *Science* **281**, 1647-1650, (1998).
31 Go, M. J., Lee, B. K., Kumar, P. A., Lee, W. K., Joo, O. S., Ha, H. P., Lim, H. B. & Hur, N. H. Immobilization of nanocatalysts on cordierite

honeycomb monoliths for low temperature NO_x reduction. *Appl. Catal. A: Gen.* **370**, 102-107, (2009).

32 Miquel, P., Granger, P., Jagtap, N., Umbarkar, S., Dongare, M. & Dujardin, C. NO reduction under diesel exhaust conditions over Au/Al_2O_3 prepared by deposition-precipitation method. *J. Mol. Catal. A: Chem.* **322**, 90-97, (2010).

33 Sárkány, A. Acetylene hydrogenation on SiO_2 supported gold nanoparticles. *React. Kinet. Catal. Lett.* **96**, 43-54, (2009).

34 Gluhoi, A. C., Bakker, J. W. & Nieuwenhuys, B. E. Gold, still a surprising catalyst: Selective hydrogenation of acetylene to ethylene over Au nanoparticles. *Catal. Today* **154**, 13-20, (2010).

35 Mohamed, M. & Khairou, K. S. Morphological Characteristics of Gold Nanowires and Nanoparticles: Structure Elucidation and Reactivity Toward Water-gas Shift Reaction. *Energ. Fuel* **23**, 4413-4419, (2009).

36 Rodriguez, J. A. Gold-based catalysts for the water-gas shift reaction: Active sites and reaction mechanism. *Catal. Today* **160**, 3-10, (2011).

37 Osmic, M., Kolny-Olesiak, J. & Al-Shamery, K. Size control and shape evolution of single-twinned platinum nanocrystals in a room temperature colloidal synthesis. *Cryst. Eng. Comm* **16**, 9907-9914, (2014).

38 Lee, H., Kim, C., Yang, S., Han, J. W. & Kim, J. Shape-Controlled Nanocrystals for Catalytic Applications. *Catal. Surv. Asia*, 1-14, (2011).

39 Kremser, G., Rath, T., Kunert, B., Edler, M., Fritz-Popovski, G., Resel, R., Letofsky-Papst, I., Grogger, W. & Trimmel, G. Structural characterisation of alkyl amine-capped zinc sulphide nanoparticles. *J. Coll. Interf. Sci.* **369**, 154-159, (2012).

40 Haruta, M. Nanoparticulate gold catalysts for low-temperature CO oxidation. *J. New Mater. Electrochem. Syst.* **7**, 163-172, (2004).

41 Comotti, M., Li, W. C., Spliethoff, B. & Schüth, F. Support effect in high activity gold catalysts for CO oxidation. *JACS* **128**, 917-924, (2006).

42 Quintanilla, A., Butselaar-Orthlieb, V. C. L., Kwakernaak, C., Sloof, W. G., Kreutzer, M. T. & Kapteijn, F. Gold Nanoparticles for the selective Oxidation of Alcohols to Aldehydes: Effect of the Capping Agent. *Poster presentation at 6th World Congress on Oxidation Catalysis*, 2009 July 5-10, Lille, France.

43 Mo, L., Liu, D., Li, W., Li, L., Wang, L. & Zhou, X. Effects of dodecylamine and dodecanethiol on the conductive properties of nano-Ag films. *Appl. Surf. Sci.* **257**, 5746-5753, (2011).

44 Dablemont, C., Lang, P., Mangeney, C., Piquemal, J. Y., Petkov, V., Herbst, F. & Viau, G. FTIR and XPS study of Pt nanoparticle functionalization and interaction with alumina. *Langmuir* **24**, 5832-5841, (2008).

45 Leff, D. V., Brandt, L. & Heath, J. R. Synthesis and characterization of hydrophobic, organically-soluble gold nanocrystals functionalized with primary amines. *Langmuir* **12**, 4723-4730, (1996).
46 Borodko, Y., Habas, S. E., Koebel, M., Yang, P., Frei, H. & Somorjai, G. A. Probing the Interaction of Poly(vinylpyrrolidone) with Platinum Nanocrystals by UV−Raman and FTIR. *J. Phys. Chem. B* **110**, 23052-23059, (2006).
47 Calla, J. T. & Davis, R. J. X-ray absorption spectroscopy and CO oxidation activity of Au/Al_2O_3 treated with NaCN. *Catal. Lett.* **99**, 21-26, (2005).
48 Liu, X., Liu, M. H., Luo, Y. C., Mou, C. Y., Lin, S. D., Cheng, H., Chen, J. M., Lee, J. F. & Lin, T. S. Strong metal-support interactions between gold nanoparticles and ZnO nanorods in CO oxidation. *JACS* **134**, 10251-10258, (2012).
49 Skupien, E., Berger, R., Santos, V., Gascon, J., Makkee, M., Kreutzer, M. T., Kooyman, P. J., Moulijn, J. A. & Kapteijn, F. Inhibition of a Gold-Based Catalyst in Benzyl Alcohol Oxidation: Understanding and Remediation. *Catalysts* **4**, 89-115, (2014).
50 Oxford, S.M., Henao J.D., Yang J.H., Kung M.C., Kung H.H., Understanding the effect of Halide poisoning in CO oxidation over Au/TiO_2. *Appl. Catal. Lett.* A., 339, 180-186 (2008)
51 Oh. D.H., Yang J.H., Costello C.K., Wang Y.M., Bare S.R., Kung H.H., Kung M.K., Selective catalytic osidation of CO: Effect of Choride onsupported Au catalysts. *J. Catal.* 210 (2002) 375.
52 Lina C.H., Lina S. D., Lee J.F Clorine residue in the Au/Al_2O_3 prepared by $AuCl_2$ impregnation-EFS analysis. *Catal. Lett.,* 89 (20016), 235-242.

6 Reduction of Noble Metal Catalysts, a Quasi In-situ TEM Study

6.1 Introduction

Noble metal catalysts have been widely used in industries such as refining, production of bulk and fine chemicals and pharmaceuticals and in environmental applications[1]. One important use of noble metal catalysts is as three-way catalyst in the automotive industry[2]. Platinum and palladium catalysts play roles in the complete combustion of CO and hydrocarbons to CO_2 and H_2O as well as the reduction of NO_x to N_2[3]. Besides their high activity and selectivity, noble metal catalysts are relatively stable. They do not easily form oxides by oxidation, do not easily dissolve in acid and alkaline solutions, and have high melting points.

To strengthen the mechanical properties of the metal catalysts and maintain the metal dispersion, the metal nanoparticles are applied to support materials. Alumina, silica and carbon are three commonly used support materials due to their refractory character, with high melting and decomposition temperatures. Aluminium oxide is widely used as a catalyst support in the form of γ-Al_2O_3, because the alumina surface has Lewis acid sites, which affects the distribution and state of the active metal catalyst[4,5]. The interactions between support and active metal catalysts, especially noble metal catalysts, have been studied for decades[6-9].

Considering the importance of the metal-support interaction, metal particle morphology and particle size distribution, catalyst preparation becomes a crucial step. Precipitation, impregnation and sol-gel manufacturing techniques are frequently used catalyst preparation methods[10-12]. Each method has advantages and disadvantages, which can be tuned to synthesise the desired catalyst for a specific application.

Reduction is part of the catalyst preparation, which is essential in the activation and regeneration of metallic catalysts. Temperature programmed reduction (TPR), Ultra Violet and Visible light spectroscopy (UV-Vis) and Fourier Transform Infra-Red spectroscopy (FTIR) are some of the characterisation techniques used to study this process[13-16]. The effective reduction temperature and the state of the metal catalyst during the process can be deduced from these characterisation results but the particle morphology and structural changes are still largely unknown. Extended X-ray Absorption Fine Structure spectroscopy (EXAFS) and Transmission Electron Microscopy (TEM) are among the techniques suitable to extract information during these processes. While EXAFS is a bulk analysis

technique, TEM is a relatively straightforward method to visualise these changes. In order to study the real changes in the particles during catalyst preparation and catalytic reaction, in-situ methods are the best option. Unfortunately, in-situ TEM methods need advanced equipment that is not easy to build (Chapters 1, 2 and 7) and not widely available. Therefore, quasi in-situ TEM experiments are sometimes applied as an alternative, in spite of their limitations. In this chapter, two examples are given of supported metal catalysts and the procedure to study their preparation by quasi in-situ TEM.

For the current study, Pt/γ-Al_2O_3 and Pd/γ-Al_2O_3 catalyst precursors were prepared by impregnation to obtain adequate particle size and high loading. The catalysts were reduced in the quasi in-situ TEM mode to study the effect of the reduction process on the particle morphology. The quasi in-situ TEM experiment is a cycle of two main parts[17,18]. The first part is the catalyst activation, which is conducted outside the TEM, and the second part is the TEM imaging, whereby the TEM samples are prepared inside a controlled-atmosphere glove box to avoid exposure to ambient conditions (Fig. 6.1). The sample is transferred from the reduction setup to the glove box using a leak-tight U-tube reactor, while a specially developed protective-atmosphere-transfer specimen holder is used to transfer the sample from the glove box to the TEM[17,18] (Fig. 6.2). In this way, the sample is prevented to have contact with air. After imaging under the TEM, the protective-atmosphere-transfer holder was closed and the sample was brought back to the glove box. The sample was put again inside the U-tube reactor. Then the reactor was attached to the reduction setup for further reduction. By repeating these procedures, quasi in-situ cycles were completed.

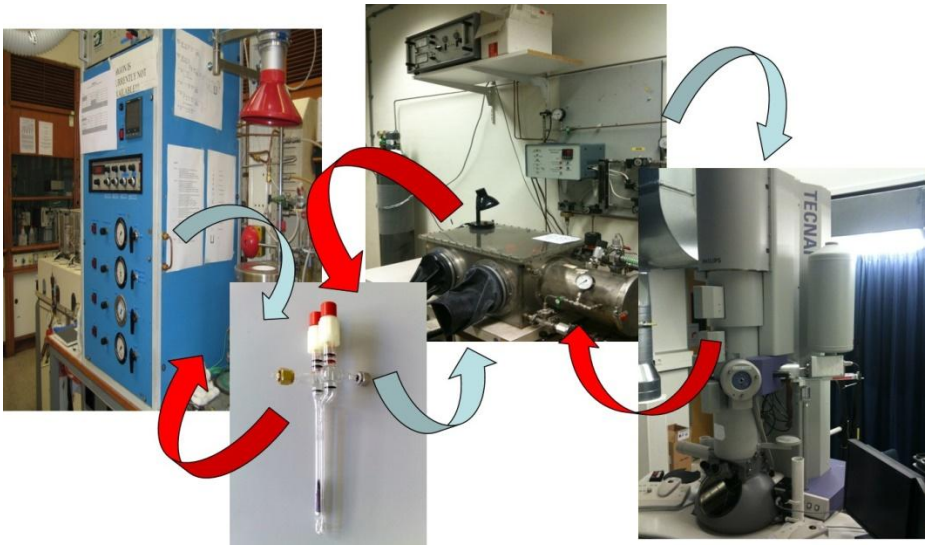

Figure 6.1. The quasi in-situ TEM cycle.

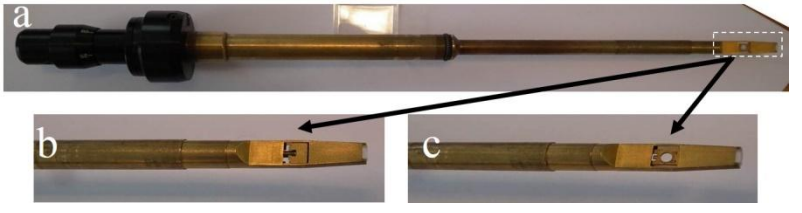

Figure 6.2. (a) The TEM protective-atmosphere-transfer specimen holder and the specimen position when it is (b) closed and (c) open.

6.2 Experimental methods

The catalyst precursors were prepared using impregnation. 1.3 g $H_2PtCl_6.6H_2O$ (Alfa Aesar, 99.95%) was dissolved in 15 ml distilled water. The suspension was added slowly to 9.5 g γ-Al_2O_3 (Ketjen CK300, particle size < 63 μm). The mixture was stirred by hand until all Al_2O_3 powder was wetted. Prior to the impregnation, the Al_2O_3 powder was dried in flowing air at 120 ^oC for 1 h to remove adsorbed water. The catalyst precursor was then dried at room temperature overnight, followed by drying in flowing air at 120 ^oC for 1 h (ramp rate 1 ^oC/min). The catalyst precursor was then calcined in flowing air at 500 ^oC for 3 h (ramp rate 5 ^oC/min).

Similar to the synthesis of the Pt/Al_2O_3, 1.2 g $Pd(NO_3)_2 \bullet 2H_2O$ (Alfa Aesar, 99.95%) was dissolved in 15 ml distilled water. The suspension was then added to 9.9 g of the pre-dried γ-Al_2O_3 powder followed by drying at room temperature overnight and at 120°C for 1 h. Calcination was performed in a flow of air at 500°C for 3 h. Atomic absorption spectrometry (AAS) was used to determine the concentration of the main components. About 50 mg of a catalyst was mixed with 1 ml concentrated hydrochloric acid (36-38%). After two hours, 50 ml of an acid mixture containing 1% hydrofluoric acid and 1.3% sulphuric acid was added and the flasks were shaken for 12 h. These digested samples were analysed using a Perkin Elmer Analyst 100 flame AAS.

The oxidation states of the catalysts were analysed using TPR. About 0.5 g of catalyst was loaded into a quartz tube reactor and connected to the TPR setup. The catalyst was heated in a gas flow of H_2/Ar gas mixture (7.7%) at a heating rate of 10 °C/min from room temperature up to 300 °C. The gas mixture at the outlet passed through a cold trap to completely retain any formed water vapour, followed by a thermal conductivity detector (TCD) to determine the consumption (or production) of hydrogen.

The quasi in-situ TEM samples were prepared in the following order. The catalysts were finely ground and suspended in ethanol. The suspensions were dropped onto Quantifoil® microgrid carbon film on mixed mesh Au TEM grids. These grids consist of four different mesh areas, which allowed us to trace the same particle after the different steps of the experiment (Fig. 6.3a). Area I has the smallest squares (the highest mesh number), while area IV has the biggest squares (the lowest mesh number). Since area IV was easily damaged, area I was chosen as the observation area (indicated by an arrow in Fig. 6.3a). The sample was then analysed under the TEM (FEI Tecnai F20) operated at 200 kV and equipped with a Field Emission Gun (FEG). After analysis, the grid was removed from the TEM, and was placed in a platinum wire gauze basket. The basket was inserted into the leak-tight U-tube quartz reactor. The reactor tube has an inner diameter of 4 mm and wall thickness of 1 mm, therefore it can withstand 1 atm reaction overpressure. Then the reactor was connected to the small activation setup for the first reduction step.

The small activation setup is usually used for pre-treatment and catalytic reaction tests of small amounts of catalyst. Several catalyst treatment procedures using single or mixed gases can be performed in this setup. The diagram of the setup is shown in Fig. 6.4.

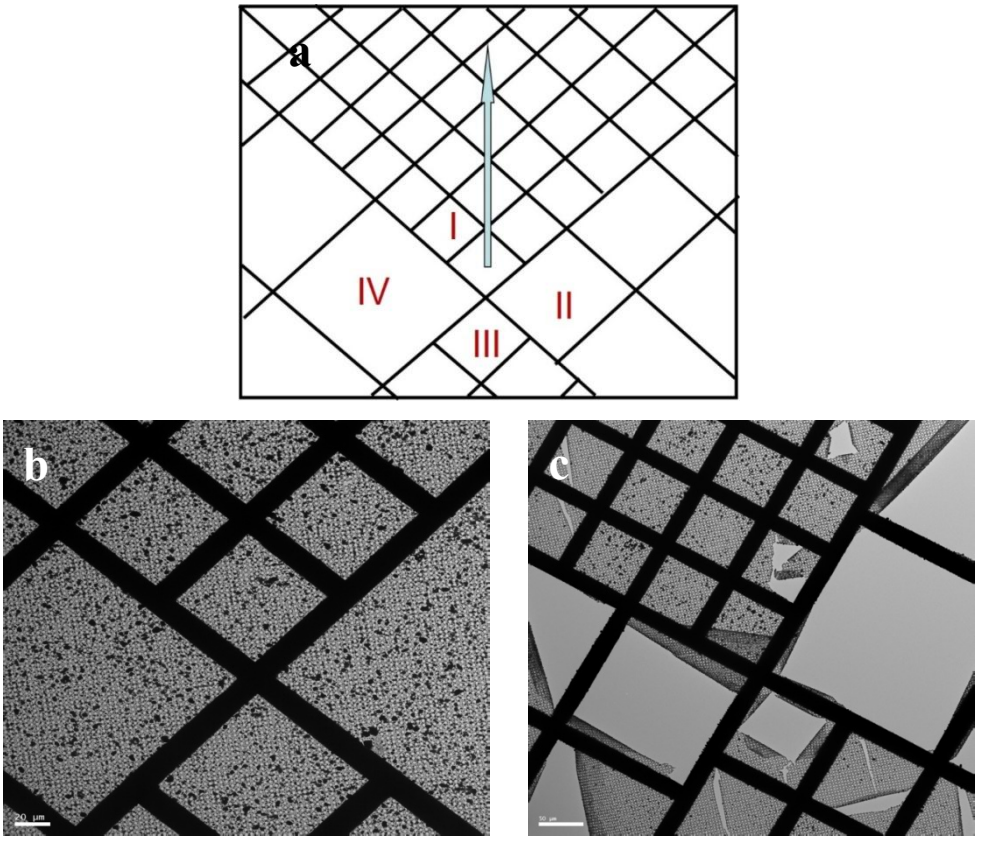

Figure 6.3. (a) The schematic design of the mixed mesh Au grids. (b) An overview TEM image of the grid and (c) a partially damaged grid after several steps from the experimental procedure.

In the small activation setup, the H_2 gas is supplied through the needle valve (NV3a). The gas flow is regulated by F1 and is set to 15 ml/min. The gas then flows to the reactor (R1). The reactor is placed in a stainless steel oven. The oven maximum temperature is 1000 ^{o}C. The oven temperature is measured by an alarm thermocouple (Ta) and a control thermocouple (Tc) and regulated by a Eurotherm 2404 controller. The check valve (CV7) is placed to avoid a too high overpressure in the gas system in case of blockage in the reactor. The valve will open to allow the gas to the vent if the gas system pressure reaches 0.7 barg = 1.7 bar absolute pressure. The product gas flows from the reactor to the vent line via two gas washing bottles.

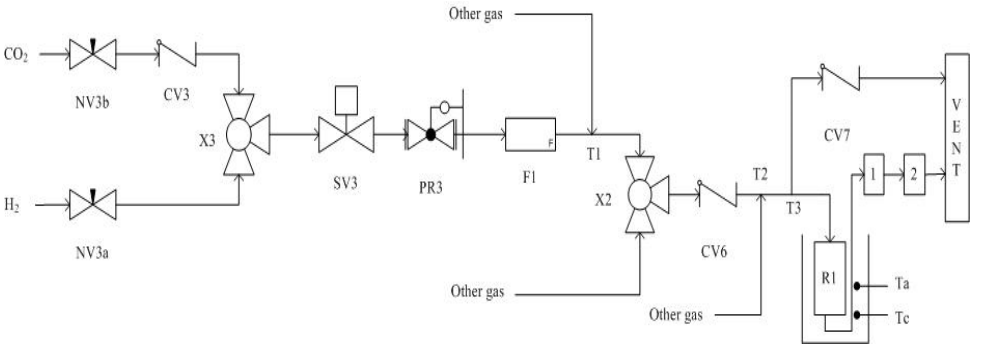

Figure 6.4. Schematic diagram of the small activation setup. (See text for description).

After the reactor was connected to the setup, the H_2 gas was passed over the sample while the oven temperature was increased step-wise from room temperature until 250 ^oC at a 5 ^oC/min heating rate. The reduction temperature was divided into several targeted steps of 50 ^oC. The dwell time at each targeted temperature (step) was 15 minutes before the reactor was cooled down to room temperature (under the same gas flow). Then N_2 was fed to the reactor for flushing. After that the reactor was tightly closed before being taken out of the small activation setup. Then the reactor was transferred into a dedicated glove box where the TEM grid was taken out of the reactor and placed in a specially developed protective-atmosphere-transfer specimen holder. Using this holder, the sample was transferred into the TEM under exclusion of air[17,18]. The grid was then analysed under the TEM.

After TEM analysis, the holder was closed before removing it from the TEM and returning it to the glove box. The TEM grid was put back in the platinum basket, and then the basket was inserted into the reactor. The reactor was tightly closed and connected again to the small activation setup. Further reduction was performed and the above procedure was repeated. By repeating these treatments, we were able to study the morphology and structure changes of the samples, in exactly the same areas, before and after reduction at increasing temperature.

6.3 Results and discussion

A small catalyst particle size is desirable for the catalytic reaction since that gives a high specific active surface area. In this study, the Pt/γ-Al_2O_3 and Pd/γ-

Al_2O_3 catalysts were prepared using straightforward impregnation with a precursor solution. After calcination, small metal crystallites with average particle size of 0.54 nm for Pt in Pt/Al_2O_3 and 7.27 nm for Pd in $Pd/\gamma\text{-}Al_2O_3$ were obtained. Apparently, the applied preparation procedure yielded very small Pt particles. The metal loading of the $Pt/\gamma\text{-}Al_2O_3$ and $Pd/\gamma\text{-}Al_2O_3$ catalysts was 4.8 wt.% and 5.0 wt.% respectively.

The temperature programmed reduction profiles in H_2 of the $Pt/\gamma\text{-}Al_2O_3$ and $Pd/\gamma\text{-}Al_2O_3$ catalysts are similar to those reported by Huizinga et al.[14] and Hong et al.[14,19]. The TPR profile of $Pt/\gamma\text{-}Al_2O_3$ shows a reduction peak of platinum oxide or oxychloride (PtO_xCl_y) to Pt^0 in the temperature range of 150-250 °C[20] (Fig. 6.5). It is known that palladium oxide already reduces at room temperature[8,21,22]. At 50 °C palladium hydride formation occurs. The TPR(H_2) profile of $Pd/\gamma\text{-}Al_2O_3$ shows a negative signal around 100 °C (Fig. 6.5), which corresponds to a release of hydrogen due to the decomposition of palladium hydrides (PdH_x) to metallic palladium[23]. Then a slender peak at high temperature (above 300 °C) relates to reduction of crystalline PdO, in strong interaction with the support[22,24]. The intensity of these peaks depends on the catalyst metal loading. Higher metal loading will give larger peaks. Based on the TPR results, the final reduction temperature for the quasi in-situ experiment was set to be 250 °C for both the $Pt/\gamma\text{-}Al_2O_3$ and the $Pd/\gamma\text{-}Al_2O_3$ catalyst.

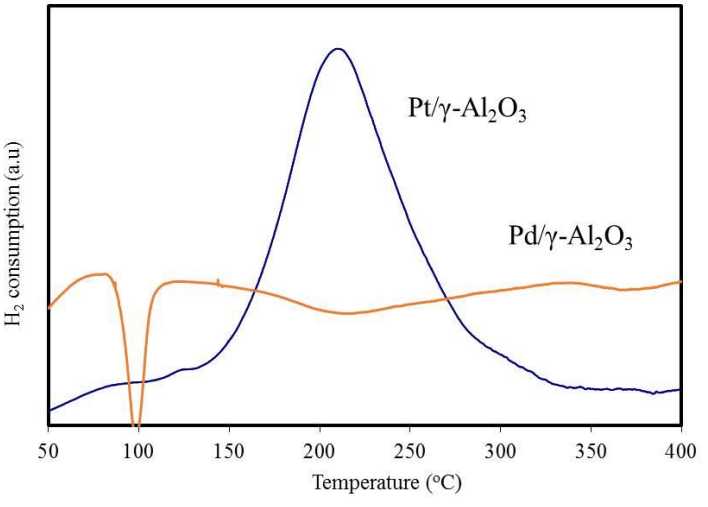

Figure 6.5. TPR(H_2) profiles of the $Pt/\gamma\text{-}Al_2O_3$ and $Pd/\gamma\text{-}Al_2O_3$ catalysts.

Mixed-mesh Au TEM grids were used for TEM analysis (Fig. 6.3). Handling the grid was a delicate process since it is easily damaged especially when it is moved to and from the reactor several times. Often the observation area was lost due to a damaged grid (Fig. 6.3b and c). In such a case, the experiment had to be repeated from the start. From our experience area I, with the smallest squares, is more robust than the other areas (Fig. 6.3). Therefore, it is suggested to choose particles in area I as observation objects.

Before imaging the observation particles, it is useful to take some overview images of the grid to pin-point the observation area and check any damage. After that, the carbon contamination test (see Chapter 3) should be performed outside the observation area. If contamination occurred, illumination of a wide area (including the observation area) for several minutes can help to decrease the contamination effect. However, if the contamination is severe, the grid is considered to be useless and the experiment should be repeated from the start. Details on the contamination tests are discussed in Chapter 3.

Figure 6.6 shows sequential images of Pt/γ-Al_2O_3 particles during the reduction process. We were able to capture and observe the same area (and the same particles, for example the particle inside the red circle) for each step in the temperature increase and measure the particle size. The average particle size collected from 25 particles is summarised in Fig. 6.7a. During reduction, the increase of the particle size already occurs at room temperature and continues as the temperature increases. The sintering mechanism is commonly explained by crystallite migration followed by coalescence, and by atomic migration (Ostwald ripening)[25,26]. In the atomic migration mechanism, the atomic species of smaller metal crystallites migrate over the surface of the support and become incorporated into a larger metal crystallite upon collision with the stationary metal crystallites. When metal crystallites randomly migrate along the surface of the support, collisions and fusion of metal particles can take place. This phenomenon explains the sintering due to crystallite migration. The processes of these sintering mechanisms are depicted in Fig. 6.8. The sintering of Pt/γ-Al_2O_3 in the current study can be categorised as atomic migration sintering because some large particles are observed to remain in the same position. Even though it is difficult to observe, the Pt atoms from smaller particles migrate over the surface of the support and are captured by larger Pt particles nearby. This can be stimulated by the presence of chlorine from the precursor[27]. The atomic migration is also triggered by changes in gas atmosphere and temperature[28]. The particle size at the end of the reduction process is less than 1 nm, which is still considered to be a good size for catalytic reactions.

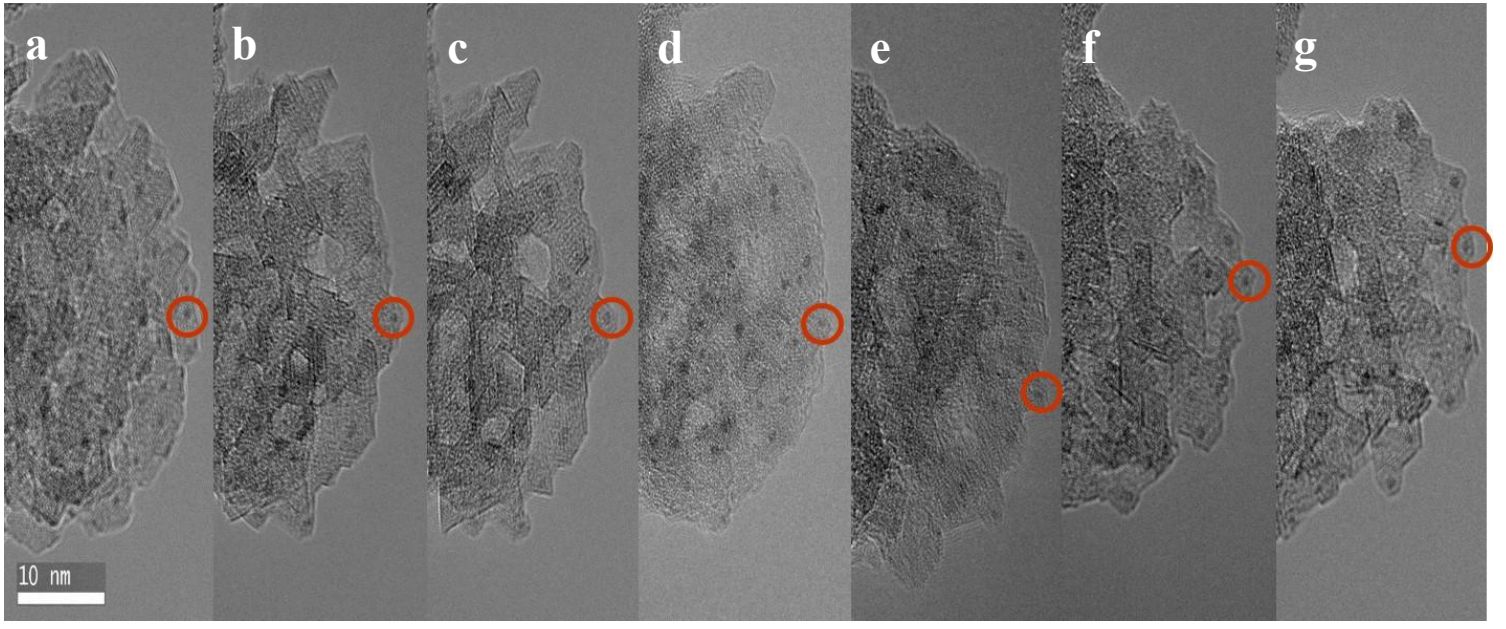

Figure 6.6. Sequential images of Pt/γ-Al_2O_3 catalyst reduction in the quasi in-situ mode. (a) As prepared catalyst; after stepwise exposure to H_2 (b) at room temperature, (c) at 50 ^oC, (d) at 100 ^oC, (e) at 150 ^oC, (f) at 200 ^oC, (g) at 250 ^oC.

For the quasi in-situ TEM experiments with Pd/γ-Al_2O_3, the settings were slightly changed from the Pt/γ-Al_2O_3 experiments in order to get (almost) complete sequential data for each reduction temperature step. As for the Pt/γ-Al_2O_3 experiments, the reduction temperature step was 50 °C. The reduction of Pd/γ-Al_2O_3 at room temperature was skipped because preliminary experiments on other Pd/γ-Al_2O_3 samples showed that there was no particle size change in this step.

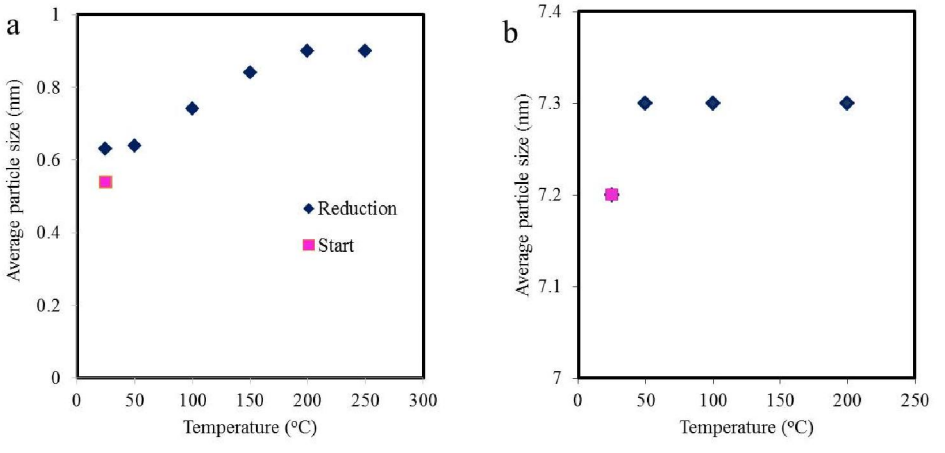

Figure 6.7. (a) Average particle size of Pt/γ-Al_2O_3 reduced stepwise to 250 °C and (b) Pd/γ-Al_2O_3 reduced stepwise to 200 °C. Particle sizes of both samples were determined using the quasi in-situ TEM mode.

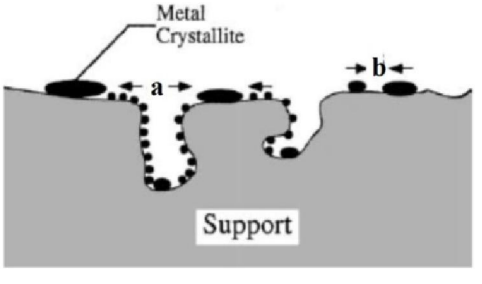

Figure 6.8. (a) Atomic migration (Ostwald ripening) and (b) crystallite migration models (reprinted from[26]).

Due to technical problems, the temperature step was also set to 50 °C higher at the fourth step. Unfortunately the Pd/γ-Al_2O_3 TEM grid was broken after reduction at 200 °C (Fig. 6.9), therefore the data point for reduction at 250 °C was not obtained.

In view of the average particle size of the observed particles, introduction of H_2 to the Pd/γ-Al_2O_3 catalyst did not induce sintering. Only after the first temperature increase to 50 °C, the particle size increased by 0.1 nm. An in-situ TEM experiment should be able to visualise this small increase and explain the phenomena in detail. In the following steps, no significant particle size increase was observed with increasing temperature up to 200 °C (Fig. 6.7b).

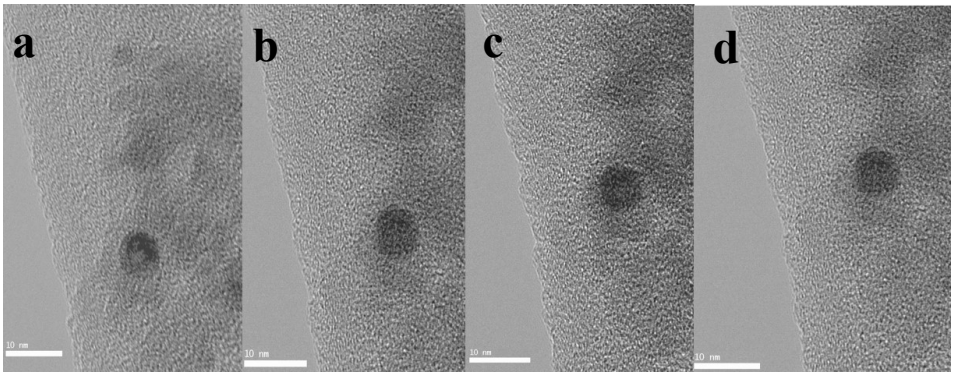

Figure 6.9. Sequential images of Pd/γ-Al_2O_3 catalyst reduction in the quasi in-situ mode. (a) As prepared catalyst, (b) after exposure to H_2 at 50 °C, (c) 100 °C and (d) 200 °C.

6.4 Conclusions

Quasi in-situ TEM is an alternative method to visualise morphological changes of individual catalyst particles during a catalyst treatment, as shown here for reduction with hydrogen. The catalyst treatment was performed outside the TEM. Then the sample was taken out of the reaction setup to the TEM for measurement, excluding exposure to ambient air. Therefore, the real particle changes during catalyst reduction or other treatment steps can be observed. In this study, the particle size of Pt in Pt/γ-Al_2O_3 was shown to gradually increase after introduction of H_2 at room temperature and with increasing reduction temperature. The Pd particle size in Pd/γ-Al_2O_3 also increased when the reduction temperature increased to 50 °C. The particle size remained the same when the reduction temperature was increased further. Despite the useful results from this method, quasi in-situ TEM is a laborious, time-consuming method. The chance of losing the observation area is significant. Once the observation area is missing, the work should restart from the beginning. A highly skilled operator is needed. Only the real-time observation of the reduction of Pt/γ-Al_2O_3 and Pd/Al_2O_3 using real in-situ TEM will be able to show the sintering process in detail.

6.5 References

1 Muroi, T. *Role of Precious Metal Catalysts, Noble Metals*. (InTech, 2012). ISBN: 978-953-307-898-4

2 Cooper, J. & Beecham, J. A Study of Platinum Group Metals in Three-way Autocatalysts. *Platin. Met. Rev.* **57**, 281-288, (2013).

3 Burch, R. Knowledge and know-how in emission control for mobile applications. *Cat. Rev. Sci. Eng.* **46**, 271-333, (2004).

4 Satterfield, C. N. *Heterogeneous Catalysis in Practice*. (McGraw-Hill, 1980). ISBN: 9780070548756

5 Bartholomew, C. H. & Farrauto, R. J. *Fundamentals of Industrial Catalytic Process*. 2nd edn., (John Wiley and Sons. Inc, 2006). ISBN: 978-0-471-45713-8.

6 Alexeev, O. S., Chin, S. Y., Engelhard, M. H., Ortiz-Soto, L. & Amiridis, M. D. Effects of reduction temperature and metal-support interactions on the catalytic activity of $Pt/\gamma\text{-}Al_2O_2$ and Pt/TiO_2 for the oxidation of CO in the presence and absence of H_2. *J. Phys. Chem. B* **109**, 23430-23443, (2005).

7 Ammendola, P., Barbato, P. S., Lisi, L., Ruoppolo, G. & Russo, G. Alumina contribution to CO oxidation: A TPR and IR study. *Surf. Sci.* **605**, 1812-1817, (2011).

8 Baker, R. T. K., Prestridge, E. B. & McVicker, G. B. The Interaction of palladium with alumina and titanium oxide supports. *J. Catal.* **89**, 422-432, (1984).

9 Boudart, M. Catalysis by Supported Metals. *Adv. Catal.* **20**, 153-166, (1969).

10 Toebes, M. L., Van Dillen, J. A. & De Jong, K. P. Synthesis of supported palladium catalysts. *J. Mol. Catal. A: Chem.* **173**, 75-98, (2001).

11 Schwarz, J. A., Contescu, C. & Contescu, A. Methods for Preparation of Catalytic Materials. *Chem. Rev.* **95**, 477-510, (1995).

12 Bass, R. J., Dunn, T. M., Lin, Y. C. & Hohn, K. L. Syngas production from catalytic partial oxidation of n-butane: Comparison between incipient wetness and sol-gel prepared Pt/Al_2O_3. *Ind. Eng. Chem. Res.* **47**, 7184-7189, (2008).

13 Chang, T. C., Chen, J. J. & Yeh, C. T. Temperature-programmed reduction and temperature-resolved sorption studies of strong metal-support interaction in supported palladium catalysts. *J. Catal.* **96**, 51-57, (1985).

14 Huizinga, T., Van Grondelle, J. & Prins, R. A temperature programmed reduction study of Pt on Al_2O_3 and TiO_2. *Appl. Catal.* **10**, 199-213, (1984).

15 Lietz, G., Lieske, H., Spindler, H., Hanke, W. & Völter, J. Reactions of platinum in oxygen- and hydrogen-treated $Pt/\gamma\text{-}Al_2O_3$ catalysts: II.

Ultraviolet-visible studies, sintering of platinum, and soluble platinum. *J. Catal.* **81**, 17-25, (1983).
16 Venkov, T., Klimev, H., Centeno, M. A., Odriozola, J. A. & Hadjiivanov, K. State of gold on an Au/Al_2O_3 catalyst subjected to different pre-treatments: An FTIR study. *Catal. Comm.* **7**, 308-313, (2006).
17 Janbroers, S., Louwen, J. N., Zandbergen, H. W. & Kooyman, P. J. Insights into the nature of iron-based Fischer-Tropsch catalysts from quasi in situ TEM-EELS and XRD. *J. Catal.* **268**, 235-242, (2009).
18 Kooyman, P. J., Buglass, J. G., Reinhoudt, H. R., Van Langeveld, A. D., Hensen, E. J. M., Zandbergen, H. W. & Van Veen, J. A. R. Quasi in situ sequential sulfidation of $CoMo/Al_2O_3$ studied using high-resolution electron microscopy. *J. Phys. Chem. B* **106**, 11795-11799, (2002).
19 Hong, C. T., Yeh, C. T. & Yu, F. H. Effect of Reduction and Oxidation Treatments on Pd/ZnO Catalysts. *Appl. Catal.* **48**, 385-396, (1989).
20 Yao, H. C., Sieg, M. & Plummer Jr, H. K. Surface interactions in the Pt/Al_2O_3 system. *J. Catal.* **59**, 365-374, (1979).
21 Chen, J. & Ruckenstein, E. Sintering of palladium on alumina model catalyst in a hydrogen atmosphere. *J. Catal.* **69**, 254-273, (1981).
22 Ferrer, V., Moronta, A., Sanchez, J., Solano, R., Bernal, S. & Finol, D. Effect of the reduction temperature on the catalytic activity of Pd-supported catalysts. *Catal. Today* **107-108**, 487-492, (2005).
23 Wang, Y., Zhang, J. & Xu, H. Interaction between Pd and ZnO during Reduction of Pd/ZnO Catalyst for Steam Reforming of Methanol to Hydrogen. *Chin. J. Catal.* **27**, 217-222, (2006).
24 Lieske, H., Lietz, G., Spindler, H. & Völter, J. Reactions of platinum in oxygen- and hydrogen-treated $Pt/y\text{-}Al_2O_3$ catalysts: I. Temperature-programmed reduction, adsorption, and redispersion of platinum. *J. Catal.* **81**, 8-16, (1983).
25 Hansen, T. W., Delariva, A. T., Challa, S. R. & Datye, A. K. Sintering of catalytic nanoparticles: Particle migration or Ostwald ripening? *Acc. Chem. Res.* **46**, 1720-1730, (2013).
26 Bartholomew, C. H. Mechanisms of catalyst deactivation. *Appl. Catal. A* **212**, 17-60, (2001).
27 Moulijn, J. A., van Diepen, A. E. & Kapteijn, F. Catalyst deactivation: is it predictable?: What to do? *Appl. Catal. A* **212**, 3-16, (2001).
28 Wanke, S. E. & Flynn, P. C. Sintering of supported metal catalysts. *Catal. Rev.* **12**, 93-135, (1975).

7 Atomic-Scale Visualisation of Pt Nanoparticles Catalysing the Oscillatory CO Oxidation

7.1 Introduction

Understanding how nanometer-sized particles catalyse chemical reactions is important for the development of efficient catalytic materials for a wide range of energy and environmental technologies. These nanoparticles generally expose different surface sites simultaneously, each with distinct reactivity for the turnover of reactants[1]. A detailed characterisation of the nanoparticle surface and the site-specific reactivity is therefore required to describe the catalytic performance of nanoparticles. However, nanoparticles often respond dynamically to changes in the surrounding environment, because changes in the gas composition affect the free energy of the exposed surfaces[2-5]. The surface structure and reactivity are therefore intimately coupled to the reaction conditions, emphasising the need for identification of active sites and their properties in-situ, during catalysis. Although many in-situ and operando techniques are available[6-10], it remains a challenge to simultaneously obtain atomic-scale information about the surface structure and reactivity of nanoparticles under relevant reaction conditions.

The role of Pt nanoparticle surfaces in the catalytic oxidation of carbon monoxide is the focus of the current study. This reaction is considered a prototype reaction for understanding fundamental concepts in heterogeneous catalysis and is relevant for automotive emission control[11]. Intriguingly, under fixed reaction parameters (flow, pressure, temperature), the Pt-catalysed CO oxidation can proceed at conversions that spontaneously oscillate as a function of time[12]. This oscillatory behaviour is commonly perceived as a periodic transformation between the two different conversion levels of a bistable reaction. The bistable reaction is caused by nonlinear kinetics[12], possibly in conjunction with mass transport[13,14]. The periodic transformation has been attributed to dynamic changes in the catalyst surface[12]. So far, the more detailed information has been obtained from studies of extended single-crystal Pt surfaces. Those studies have proposed that the oscillatory reaction is caused by an adsorbate-induced restructuring at low pressures (below 10^{-4} mbar)[12] and is related to switching between a metallic and an oxidic state at higher pressures (above 1 mbar)[15,16]. In contrast, direct observation of Pt nanoparticles during oscillatory CO oxidation is lacking. Therefore, the role of the Pt surface structure still remains unsolved.

A direct visualisation of the shape and surface structure of the nanoparticles can be obtained by means of transmission electron microscopy (TEM), which can provide two-dimensional projected images of nanoparticles with a resolution and sensitivity at the atomic level[17-19]. Such images can even be acquired during the exposure of the nanoparticles to reactive gas atmospheres, confined to the vicinity of the nanoparticle specimen using a differential pumping system[4-6] or a closed, electron-transparent cell[20-23]. Although the in-situ TEM capability has provided unprecedented time-resolved observations of gas-induced surface processes on nanoparticles[4-6,24,25], the high-resolution TEM studies have so far been limited to pressures of a few mbar (which is well below the atmospheric pressure levels used in heterogeneous catalysis) and to a complex gas-flow geometry (which hampers the structural information to be uniquely correlated with concurrent activity measurements[26]).

In the present study, a recently developed nanoreactor (Chapter 2)[21,22] is employed to study the surface structure of Pt nanoparticles during the oscillatory oxidation of carbon monoxide. The nanoreactor is a microelectromechanical system[21-23,27] and includes a unidirectional gas-flow channel with a reaction zone at 1 bar pressure and elevated temperatures, representative for automotive exhaust catalysis. The nanoreactor is functionalized for simultaneous high-resolution TEM observations of the Pt nanoparticles, quantitative mass spectrometry (MS) of the gas exiting the nanoreactor and reaction calorimetry. From such time-resolved observations, the oscillatory CO oxidation reaction is shown to be synchronised with a periodic refacetting of the Pt nanoparticles in such a way that the higher conversion is associated with a transformation towards more extended close-packed facet terminations of the Pt nanoparticles, and the lower conversion is associated with a transformation towards more higher-index and stepped terminations of the Pt nanoparticles, respectively. A comparison with density functional theory (DFT) and mass transport calculations suggests that the refacetting is due to the site-dependency of CO adsorption energy and oxidation rate, and represents a mechanism for oscillatory shifts between the conversion levels. A significant implication of this study is therefore that dynamic structure-functionality relationships in heterogeneous catalysis can now be directly determined at the atomic level and under relevant reaction conditions.

7.2 Experimental methods

The new generation of SMNR (Chapter 2) was used in this experiment. The nanoreactors have a 280 µm wide channel, which is 4.5 µm high. An image of the channel with the heather zone is shown in Fig. 7.1a. The arrow indicates the flow

direction. The channel is interfaced to a gas supply at the inlet and a mass spectrometer (MS) at the outlet. At the nanoreactor centre, a thin film Mo resistor enables heating and temperature measurement of the reaction zone of 0.34 nL at 1 bar pressure. The nanoreactor has 18 nm thick electron-transparent windows for TEM imaging.

The drop-loading method (Chapter 2) was used to load the nanoreactor with a 4% aqueous tetrammineplatinum (II) nitrate solution. The nitrate compound was decomposed by drying on a hot plate at 300 ^{o}C, leaving platinum oxide particles inside the nanoreactor.

The loaded nanoreactor was checked in the TEM prior to the in-situ experiment, to confirm sufficient particles had been deposited on the nanoreactor electron transparent windows. A contamination test was also performed to make sure no contaminants were introduced during the loading step (Chapter 3.2). After that, the nanoreactor was inserted into a dedicated in-situ TEM holder (Fig. 2.7). The holder was then connected to the gas system. The CO, O_2 and He gas mixtures were supplied into the TEM holder with an inlet pressure of 2 bar. The outlet tubes were connected to the mass spectrometer (MS) that operated at a pressure of 10^{-5} mbar. During the experiment, the pressure at the nanoreactor inlet and outlet was assumed to be the same as the pressure at the holder inlet and outlet. The pressure drop over the gas tubes was assumed to be negligible. The pressure in the centre of the nanoreactor was assumed to be the average of the pressures at the nanoreactor inlet and outlet[21,28].

The reaction temperature was controlled by a custom-made PID controller (Chapter 2.2.4) with 1 ms response time. The average temperature of the nanoreactor was determined through measurement of the (calibrated) electrical resistance of the Mo heating element in the nanoreactor[29]. For each temperature change, the nanoreactor temperature settled within a few ms due to the low thermal mass of the nanoreactor reaction area. A LabView script was used to regulate the temperature changes with 0.5 s readout time. The CO oxidation is an exothermic reaction that released 0.8 mW heat during the reaction (based on the heat of reaction which was calculated from the p_{CO2} (from MS data) or from the lower heater power required at full conversion), which is at least one order of magnitude lower than the electrical power required by the Mo heater to maintain a constant temperature (Fig. 7.5). A constant temperature in the nanoreactor was maintained by adjusting the power to the Mo heater. The measured changes in heating power were treated as calorimetric data from the experiment.

For CO oxidation experiments, two different gas mixtures were used:

1. Gas mixture A: A premixed gas with CO: O_2: He = 4.2%: 21.0%: 74.8% (gas purity 99.99% for O_2 and He, and 99.97% for CO).
2. Gas mixture B: The premixed gas (A) mixed with pure O_2 (gas purity 99.99%). Resulting gas composition CO: O_2: He = 3%: 42%: 55%.

Before being fed to the nanoreactor inlet, the gases were passed through an active carbon filter to remove Ni-carbonyls. A Pfeiffer Prisma QME200 quadrupole mass spectrometer (MS) was used for gas analysis. The signals from He, CO, O_2 and CO_2 were monitored continuously. The MS dwell time was 0.1 s with 1.8 s total spectrum acquisition time.

The in-situ TEM experiments were performed using an FEI Titan 80-300 environmental transmission electron microscope, operated at 300 keV[30]. During the experiments, the pressure around the nanoreactor was kept below ca. 1 x 10^{-5} mbar. Prior to each experiment, the aberration corrector was tuned using a Au/C cross-grating (Agar S106). The spherical aberration coefficient was in the range of -16 to -24 µm and flat information transfer was established at electron scattering angles up to at least 11 mrad. The high-resolution images were acquired with dose rates of 5-300 e/Å^{2}s and at 0.1-0.5 s exposure time with or without zero-loss peak filtering by a 15 eV energy slit. The dose rate measured through vacuum with the nanoreactor retracted from the electron beam path was within 1% of the value measured through a nanoreactor containing 1 bar of reaction gas. The TEM images were acquired at different magnifications, corresponding to a pixel size extending down to 0.05 nm. This detection limit is sufficient for resolving the Pt (111) and Pt (200) lattice planes having lattice spacings of 0.23 nm and 0.20 nm, respectively. These conditions were set to avoid electron beam induced effects on the nanoparticles. The Pt facet images were taken to confirm the more facetted nanoparticles (modelled by Pt(111)) and the more spherical nanoparticles (modelled by Pt(211)).

The TEM images, MS and heater power data were recorded on separate computers. Prior to the experiment, the clocks in all computers were synchronised. Furthermore, the data were post-synchronised to achieve a precision of 1 s in the temporal resolution. The heater controller responded to power changes on the millisecond time-scale, which was faster than the readout of the charge-coupled device (CCD) camera and MS. The post-synchronisation was therefore done by first relating MS data to heater power data (Fig. 7.8). Subsequent alignment of TEM data to heater power data was done by exploiting the small detectable specimen drift that occurs upon changes in the heater power.

Reactor simulations

The global partial pressures measured by the MS will differ from the local pressures at the different electron transparent windows, because the conversion of CO occurs as the gas flow passes the reaction zone in the nanoreactor. Likewise, a thermal gradient will exist between the gas inlet (which is kept at room temperature) and the centre of the reaction zone (which is kept at an elevated temperature). A significant thermal gradient within the reaction zone will be present as well[29]. Thus, the local temperature at the electron transparent windows differs from the global temperature (measured by the resistivity of the Mo thin film heater)[29].

To estimate the difference between the local and global conditions, simulations of temperature and concentration gradients were done using Matlabs's PDE module. Energy and mass balance equations were solved iteratively until convergence as outlined below, using the finite element method on a mesh of triangles representing the nanoreactor geometry.

The first step is to determine the temperature distribution across the nanoreactor. Assuming steady-state conditions in the nanoreactor, the temperature gradient can be modelled independently using the two-dimensional energy balance over the nanoreactor, assuming negligible contributions from the catalytic reaction and heat capacity of the gas flow:

$$-\lambda \nabla^2 T = Q \qquad \text{(Eq. 7. 1)}$$

where λ is the thermal conductance ($W.K^{-1}$), T is the temperature (K), and Q is the heat input by the heater ($W.K.m^{-2}$). The inevitable variation in temperature across the nanoreactor results in a spatial variation of the reaction rate. For a uniform distribution of Pt, the reaction rate at the particles close to the walls in the nanoreactor channel will be lower than that at the centre of the heater.

The gradients in gas composition over the reaction zone and concentration dependency on the gas flow and diffusion inside the nanoreactor are also addressed by the finite element simulations. The two-dimensional concentration profile inside the nanoreactor is simulated, assuming a constant flow along the gas channel (the x direction), using the following molar balance:

$$D_{CO}\nabla^2 c_{CO} - v\frac{dcCO}{dx} - r(T.C_{CO}) = 0 \qquad \text{(Eq. 7.2)}$$

where D_{CO} is the CO diffusivity of the gas entering the reaction zone ($m^2.s^{-1}$) and c_{CO} is the normalised CO pressure (the ratio between the local CO pressure in the nanoreactor and the CO pressure at the inlet). The flow field is assumed to be

constant, with an average gas velocity (v) (m.s^{-1}) in the gas flow direction. The reaction rate at a specific spot in the nanoreactor is denoted as $r(T,c_{CO})$ (s^{-1}) and is described by a simplified Langmuir-Hinshelwood expression:

$$r(T,c_{CO}) = \frac{k_1 \exp\left(-\frac{E_a}{k_B T}\right) c_{CO}}{\left(1 + k_2 c_{CO}\right)^2} \qquad \text{(Eq. 7.3)}$$

where E_a is the apparent activation energy of the reaction (eV), which is determined experimentally. k_B is the Boltzmann constant (8.6 x 10^{-5} eV.K^{-1}) and T is the local temperature (K) given by the simulation described by Eq. 7.1. Parameter k_1 is a pre-exponential factor (s^{-1}) and k_2 represents an adsorption constant.

The boundary conditions and an initial value for the CO concentration in the nanoreactor are required to solve the transport equation (Eq. 7.2) using the numerical solver implemented in the Matlab software package[31]. The iterative procedure requires an initial guess for the solution as well as boundary conditions and the temperature distribution defined by the nanoreactor geometry and experimental conditions. With respect to the choice of the initial guess, it is important that it does not directly affect the iterative derived solution. A chemical flow reactor under a self-inhibiting catalytic reaction as described by Eq. 7.3 can sustain multiple steady-states in which the intrinsic catalytic rate equals the mass transport rate, even for the same catalyst and temperature[13,14]. Thus, the initial guess determines which steady-state solution is obtained, i.e. which is the one closer to the guess than any other. One obvious initial guess is therefore a CO concentration representing the state of high conversion at the highest temperatures and this initial guess is taken as 0 mbar (full conversion).

The boundary conditions are as follows:

1. The CO concentration at the inlet is 42 mbar.
2. The diffusion and flow through the walls are zero.
3. The diffusion (concentration gradient) is set to be zero at the outlet[32].
4. The uniformly heated Pt layer has a diameter of 320 μm.
5. The total input power is chosen such that the global temperature is in the interval 308-457 °C.

Initially k_1 and k_2 are set to physically relevant values. With these conditions, Eq. 7.2 and 7.3 are solved in the following way: Starting at the lowest temperature in the experiment (at 308 °C) the temperature distribution of the reaction zone was found by solving the energy balance (Eq. 7.1). The mass balance equation (Eq. 7.2) was then iteratively solved until convergence was reached (i.e. the difference

between the terms on the left and right hand side of Eq. 7.2 is below 10^{-11}). The solution is a CO concentration profile with minimum conversion due to the low temperature. Subsequently the temperature was stepped up. At the increased temperature, the temperature distribution was first determined. The CO concentration profile found at the previous temperature was used as a new initial guess for the next iterative solution of Eq. 7.3, resulting in slightly higher CO conversion due to the increase in temperature. This procedure was repeated for increasing temperatures up to 457 ^{o}C. Then an initial guess of 0 mbar CO (full conversion) was employed and the same iterative procedure applied to solve Eq. 7.3 for decreasing temperatures down to 308 ^{o}C (or the temperature at which convergence failed). The outlet CO pressure from the two sets of simulations was compared to experimental data presented in Fig. 7.2. Based on the comparison, k_1 and k_2 (Eq. 7.3) were altered and the two sets of simulations were repeated. The iterative procedure was terminated when the simulated exit CO concentration qualitatively matched the experimental values over the entire temperature range, as demonstrated in Fig. 7.3a. The values of k_1 and k_2 are found to be 2.66 x 10^{14} s^{-1} and 20, respectively.

Micro-kinetic models

To model the CO oxidation rate on Pt(111) and Pt(211), a steady-state micro-kinetic model based on Density Functional Theory (DFT) calculated adsorption and transition state energies is employed. The more facetted nanoparticles are modelled by the Pt(111) facet and the more spherical nanoparticles are modelled by the Pt(211) facet. A Langmuir-Hinshelwood type model is assumed for the CO oxidation, described by the following elementary steps:

1. $CO(g) + * \leftrightarrow CO*$
2. $O_2(g) + * \leftrightarrow O_2*$
3. $O_2* + * \leftrightarrow 2O*$
4. $CO * + O* \leftrightarrow CO_2(g) + 2*$

where * denotes a free surface site, and X* denotes an adsorbed species X. The rates for these elementary steps are given by:

$$r_1 = p_{CO}\theta_* k_1^+ - \theta_{CO} k_1^-$$
$$r_2 = p_{O_2}\theta_* k_2^+ - \theta_{O2} k_2^-$$
$$r_3 = \theta_{O2}\theta_* k_3^+ - (\theta_O)^2 k_3^-$$
$$r_4 = \theta_O \theta_{CO} k_4^+ - (\theta_*)^2 p_{CO_2} k_4^-$$

Where k_1, k_2, k_3 and k_4 are the rate constants. The θ_{CO}, θ_{O2}, θ_O, and θ_* are the surface occupancies of CO, O_2, O and free adsorption sites, respectively. We assume that each adsorbed species occupies one surface site, so the site balance becomes:

$$\sum_i \theta_i = 1 \Rightarrow \theta_* + \theta_O + \theta_{O2} + \theta_{CO} = 1$$

The forward rate constant for each elementary step is given by $k_i^+ = k_B T \exp\left(-\Delta G_i^{act} / k_B T\right)$ and the equilibrium constant by $K_i = \exp\left(-\Delta G_i / k_B T\right)$, where the reverse rate constant is given consistently by $k_i^- = \frac{k_i^+}{K_i}$. The reaction free energy, ΔG_i, and the activation free energy, ΔG_i^{act}, for each elementary step were obtained from the free energies of the reactants, transition state and products from:

$$G(T) = E_{DFT} + E_{ZPE} + \int_0^T C_{v,vib} dT - T \cdot S$$

where E_{DFT} is the electronic energy[33], E_{ZPE} is the zero-point energy, $C_{v,vib}$ is the heat capacity and S is the entropy. The vibrational energy comes from the heat capacity. For each adsorbed species the heat capacity and entropy are calculated using:

$$\int_0^T C_{v,vib} dT = \sum_i^{vib.energies} \frac{\varepsilon_i}{\exp^{\varepsilon_i / k_B T} - 1}$$

$$S(T) = k_B \sum_i^{vib.energies} \left(\frac{\varepsilon_i}{k_B T\left(\exp^{\varepsilon_i / k_B T} - 1\right)} - \ln\left(1 - \exp^{-\varepsilon_i / k_B T}\right) \right)$$

The zero-point energy, heat capacity and entropy for the transition state and the dissociated state are assumed to be the same. For the gas phase, the entropy and heat capacity contributions were calculated using the Shomate equation with the parameterisation from NIST[34].

Time-dependent reactor simulations

A two-dimensional time-dependent reactor model describes the temperature profile and partial pressure inside the nanoreactor. But the pressure- and site-dependent reaction rate (from the micro-kinetic model), and time-dependent changes in the catalyst morphology would make the computations extremely time-consuming.

Therefore, the gas-dependent Pt nanoparticle shape (from the micro-kinetic model) and the total mass transport through the nanoreactor are combined in a simplified and generic time-dependent one-dimensional chemical reactor model, to address whether the gas-dependent Pt nanoparticle shape can sustain an oscillatory CO oxidation reaction in the nanoreactor. The model describes the nanoreactor as a one-dimensional system, with time-dependent CO concentration and temperature of the reaction zone. The latter is a simplification of the temperature profile in that zone, determined by the resistance of the heater (Figure 7.4). Then the Pt nanoparticles are considered to consist of a combination of facet and step sites. The distribution of surface sites exposed to the reaction environment is therefore described by one parameter (α), which acts as a simple shape descriptor for the Pt nanoparticle and which is defined as the fraction of (111) sites to the sum of (111) and (211) sites. Combining this model for the Pt surface morphology with the site-dependent reaction rates (r_{hkl}) obtained from the DFT calculations allows the total reaction rate, r, (or turn-over-frequency, TOF) to be calculated as a simple linear combination of the two considered facets:

$$r = \alpha \cdot r_{111} + (1 - \alpha) \cdot r_{211}$$

The nanoparticles are assumed to obtain an equilibrium shape that depends on the CO pressure[4] and therefore changes as the CO pressure changes during the reaction. Because the surface coverage of O and CO changes markedly at a critical CO pressure $P_{CO,cri}$ = 1 mbar at both sites (Fig. 7.15), the equilibrium shape is assigned with a facetted shape ($\alpha_{facetted}$) for P_{CO} < 1 mbar and a rounded shape ($\alpha_{rounded}$) for P_{CO} > 1 mbar. To describe the dynamic evolution in nanoparticle shape during the reaction, the temporal evolution in α is assumed to be proportional to the deviation between the actual and the equilibrium value of α.

Thus, the dynamic shape of the nanoparticles is described by the following equations:

$$\alpha_{eq}(y) = \begin{cases} \alpha_{rounded}, & y > y_{CO,cri} \\ \alpha_{faceted}, & y < y_{CO,cri} \end{cases} \quad \text{(Eq. 7.4)}$$

$$k\frac{d\alpha}{dt} = \alpha_{eq}(y) - \alpha \quad \text{(Eq. 7.5)}$$

where y is the ratio of the CO pressure at a given spot in the nanoreactor and the inlet CO pressure, $y_{CO,cri}$ is $P_{CO,cri}$ normalised with respect to the inlet pressure, t is the time normalised with the residence time ($\tau = 2.69\times10^{-4}$ s) and k is a constant governing the rate of change in the site distribution.

For the simulation, k is chosen to be $100*Pe = 132$.

$$Pe = \frac{L.u}{D}$$

where Pe is the Péclet number, L is the nanoreactor heating zone length (320 µm), u is the flow rate (1.119 $m.s^{-1}$) and D is the dispersion coefficient ($2.88x10^{-4}$ $m^2.s^{-1}$, corresponding to the diffusivity of CO in He). A Péclet number of 1.32 means that diffusion and convection in the gas phase are of similar importance. With this choice of k, the morphology change is slower than the residence time in the reactor, as is actually observed. Choosing a larger value for k is only expected to increase the period of the oscillations, whereas a lowering of k will decrease the period as long as the change in catalyst shape is much slower than the residence time.

The dimensionless reaction rate, r, is obtained from the turn-over-frequency (TOF) by:

$$r = \varphi \cdot TOF \qquad \varphi = \frac{\rho_{Sites} \cdot \beta_{loading} \cdot L^2 \cdot k_b T}{D \cdot P_0} \quad \text{(Eq. 7.6)}$$

Where ρ_{sites} is the number of sites per volume in the reactor, i.e. the number of atoms on the Pt surface, 1×10^{15} sites per cm^2, divided by the reactor height (4.5 µm). $\beta_{Loading}$ is the Pt loading and is set to 10.5 vol.%, which corresponds to an estimation of the amount of platinum in a nanoreactor. P_0 is the total inlet CO pressure (P_0 = 42 mbar). In summary, the multiplication factor φ=7.93×10^{-5} s.

To describe the gas composition throughout the nanoreactor, the following generic time-dependent and one-dimensional convection-diffusion equation, including the two-site reactivity micro-kinetic model, is used[35]:

$$\frac{d^2y}{dx^2} - Pe\frac{dy}{dx} - \alpha r(y)_{111} - (1-\alpha)r(y)_{211} = Pe\frac{dy}{dt} \qquad \text{(Eq. 7.7)}$$

where x is the position along the reactor divided by the reactor length (L) and t is the time normalised to the residence time (τ). r_{111} and r_{211} are the dimensionless reaction rates for the (111) and (211) surfaces, respectively, from the micro-kinetic model (sub chapter 7.2.2). For the simulations, the boundary conditions at the inlet to the reaction zone are: 1) $y = 1$, i.e. the partial pressure is set to the inlet pressure and 2) α is calculated using the inlet gas composition. The boundary condition at the outlet sets the gradient of y and α equal to zero. Moreover, to ensure diffusion-free boundary conditions, the inlet and outlet of the reactor are set four times L in front of the reaction zone entrance and five times L behind the reaction zone exit. Eq. 7.5 and 7.7 are solved using Matlab, with an absolute tolerance on the solution smaller than 10^{-8} [36].

7.3 Results and discussion

Figure 7.1a shows the nanoreactor channel and the direction of the gas flow from the inlet to the outlet. Observation windows were selected where Pt nanoparticles in the size range of 3-30 nm were present (Figs. 7.1b and c). The reactor simulation of the CO concentration at 437 °C along the nanoreactor channel shows that there are two conversion levels, low conversion (Fig. 7.1d) and high conversion (Fig. 7.1e), which is referred to as the bistable regime.

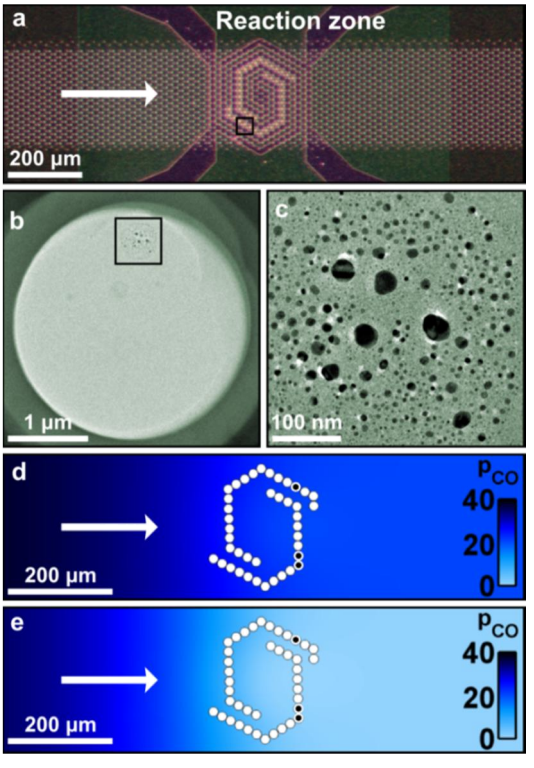

Figure. 7.1. (a) Light optical image of the nanoreactor with the gas channel and the reaction zone; (b) A TEM image of the framed window in (a) showing that Pt nanoparticles (dark contrast) are dispersed heterogeneously on the electron-transparent window; (c) A close-up of the specific area in the window framed in (b) showing as-prepared Pt nanoparticles; 1-D steady-state simulation of the CO concentration profile ($[P_{CO}]$: mbar) in the nanoreactor at a (d) low and (e) high conversion of the bistable regime at 437 ^{o}C (bistable regime is in the range of 433-439 ^{o}C). The white arrows indicate the gas flow direction. The dark circles in d) and e) show the observation windows. The gas entering the reaction zone is 1 bar of gas mixture A.

To initialize the CO oxidation reaction, 1 bar of gas mixture A is fed to the reaction zone at temperatures above 300 ^{o}C (Fig. 7.2a). An increase of the CO_2 signal is detected by MS in the outlet gas. At temperatures lower than 300 ^{o}C, the signal-to-noise ratio in the MS data is too low to determine the variations in the CO_2 signal with changes in temperature. Therefore the signal is then divided by the He signal and normalized to the maximum value of that ratio at 455 ^{o}C. At

temperatures above 450 °C, the CO_2 signal does not change anymore with an increase in temperature, indicating full conversion of CO. Data from the temperature increase (grey triangles) and temperature decrease (grey circles) are used to draw the Arhenius plot (Fig. 7.2b) which shows that in the temperature range 320-420 °C the CO conversion fits the exponential dependency of the inverse temperature (black curve). The measured activation energy (E_a) is 1.3 eV.

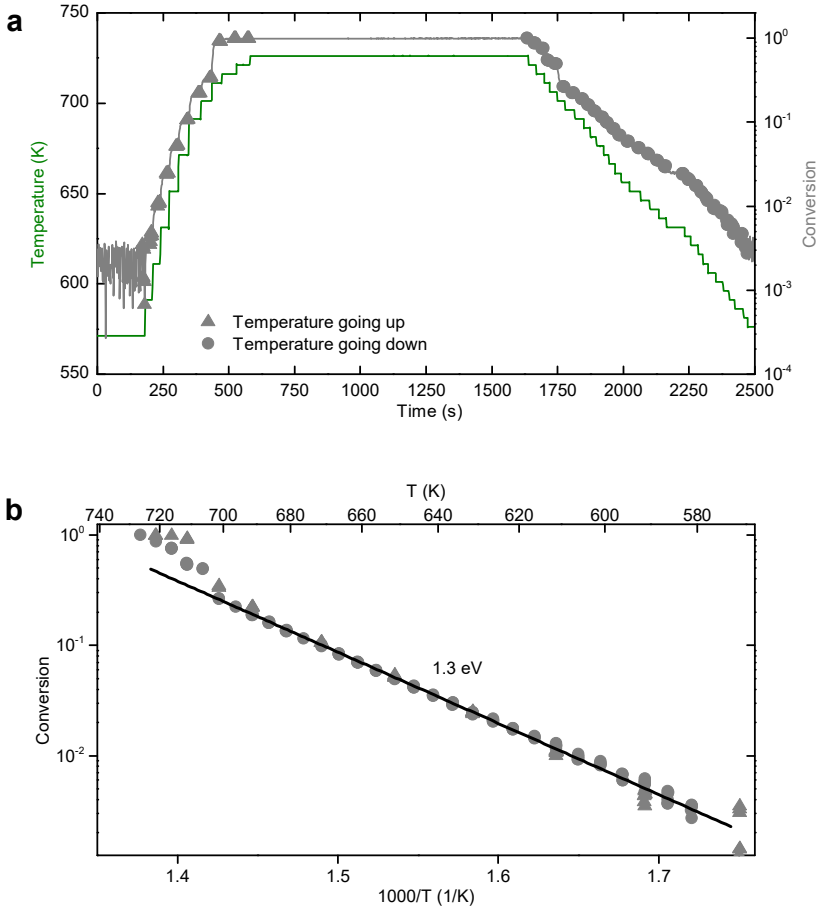

Figure 7.2. (a) Temperature dependence of the CO oxidation reaction when the nanoreactor was exposed to 1 bar of gas mixture A and operated at different temperatures (green line) as function of time. The grey line is calculated as the CO_2 signal divided by the He signal and normalised with respect to the maximum value of that ratio at 455 °C; (b) The Arrhenius plot of the CO conversion versus the inverse temperature.

Assuming a homogeneous distribution of the Pt nanoparticles over the reaction zone, the CO oxidation reactor simulation is presented in Fig. 7.3. The temperature distribution across the nanoreactor is modelled by Eq. 7.1 (Fig. 7.3a). The calculation neglects the effect of the CO conversion and only considers the thermal conduction of the membrane and the heater. The thermal conduction results in a temperature profile along the nanoreactor even though there is no CO conversion (Fig. 7.3b). The total input power is 18.9 mW, resulting in a simulated global temperature of the nanoreactor of 437 ^{o}C. The maximum temperature difference between the warmest and coldest electron transparent window is 72 ^{o}C. The global measured temperature of the nanoreactor is 438 ^{o}C at a total input power between 19.0 mW (at low CO conversion) and 18.7 mW (at high CO conversion). The numbers demonstrate good agreement between modelling and experimental results.

The line-scans of the temperature distribution in the nanoreactor along the channel and through the reaction zone (Fig. 7.3b) correspond to the global temperature at 437 ^{o}C at zero CO conversion (black line), at the low CO conversion (blue line) and at the high CO conversion (red line). An enlargement of the top part of the peak is shown in Fig. 7.3c. The temperature distribution across the nanoreactor at a global temperature of 454 ^{o}C is described in Fig. 7.3d, where the black circle corresponds to 520 ^{o}C.

The CO conversions from the simulation and MS data are compared as a function of temperature in Fig. 7.4a. The match of the two results shows that the model is sufficient to capture the overall conditions in the nanoreactor. The inset shows that in the temperature range of 433-439 ^{o}C two conversion levels are observed, which explains the bistable regime[14]. The CO conversion simulation at the low CO conversion level is shown in Fig. 7.4b and the high CO conversion level is shown in Fig. 7.4c. The CO pressure profiles of both CO conversion levels are shown in Fig. 7.4d, where the orange line corresponds to the low conversion level and the red line corresponds to the high conversion level. The dip in the CO pressure at the outlet windows is due to the CO depletion close to the hot centre.

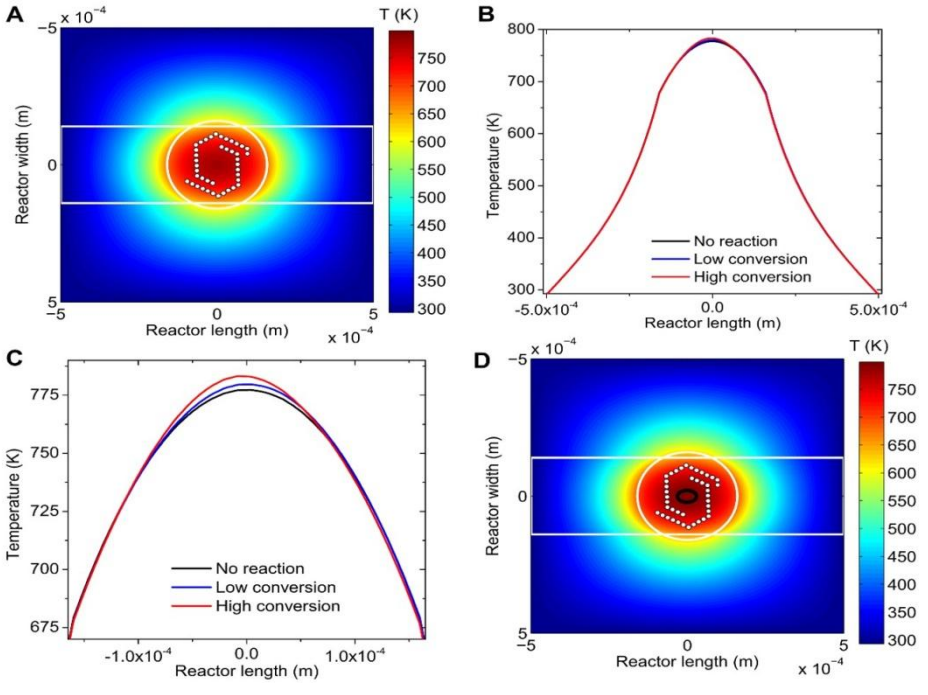

Figure 7.3. (a) 2-D simulation of the temperature profile across the nanoreactor reaction zone at a global temperature of 437 °C. The colour scale indicates the temperature in K. The large white circle outlines the periphery of the heater, the straight white lines outline the gas channel and the small white disks show the positions of the windows; (b) Line-scans of the axial temperature profile in the nanoreactor along the centreline of the channel and (c) the enlargement of the top part of the curve; (d) Temperature distribution across the reaction zone at a global temperature of 454 °C. The black oval (in the middle) corresponds to the 520 °C isotherm.

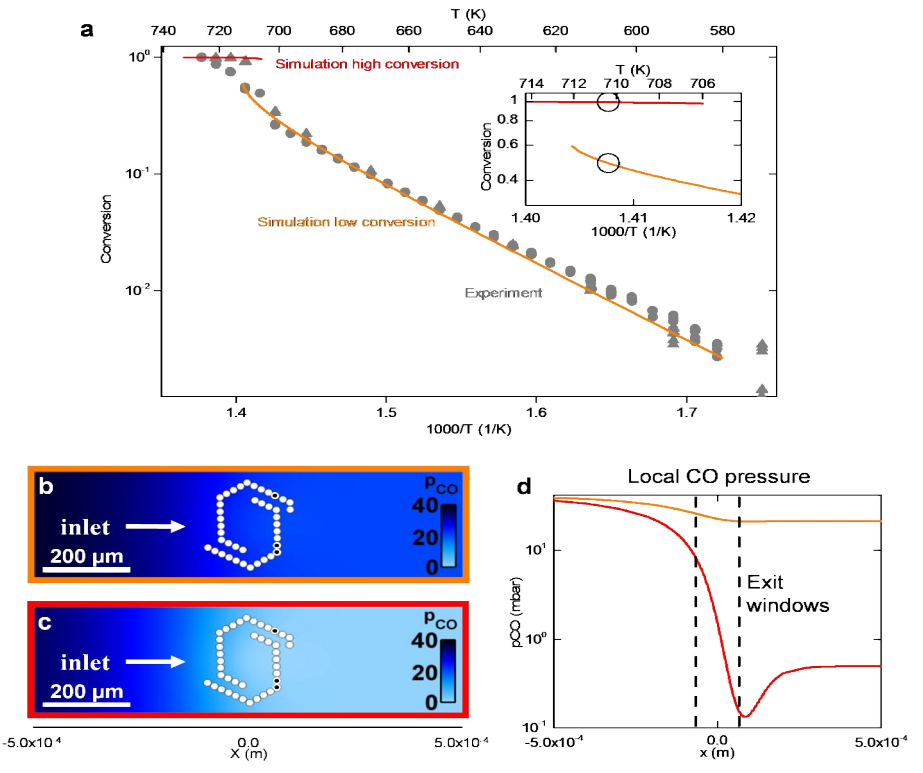

Figure 7.4. (a) Comparison of the simulations and MS data of the CO conversion at the nanoreactor outlet as a function of temperature. The inset shows the bistable regime where the two conversion levels were observed; The 1-D simulated CO concentration profile in the nanoreactor at (b) low and (c) high conversion of the bistable regime at 437 °C; (d) The CO profile along the centre of the nanoreactor (2-D simulation). The orange line corresponds to the low conversion branch in (b) and the red line corresponds to the high conversion branch in (c). The dashed lines outline the region containing the electron transparent windows. The gas entering the reaction zone is 1 bar of gas mixture A. The dip in the CO pressure at the outlet windows is due to the CO depletion close to the hot centre (see Fig. 7.3)

The heat of reaction is the energy released per unit time by the CO oxidation reaction. The heat of reaction can be calculated from the CO_2 pressure as measured by MS. But this approach requires the quantification of the gas flow rate through the nanoreactor to determine the amount of CO_2 produced. Alternatively, the heat of reaction can be approximated from the heater power. At constant

temperature, the sum of the heater power and heat of reaction is a constant offset power. The nanoreactor loaded with Pt nanoparticles is exposed to 1 bar of gas mixture A at 427.5 °C. The gas flow rate is 0.09 ml_n/min, corresponding to a space velocity of 4500 s^{-1} for the 0.34 nL reaction zone. The heater offset power is 18.8 mW. The heat of reaction from the gas flow rate (blue curve) of this nanoreactor matches the heat of reaction from the offset power (black curve) (Fig. 7.5).

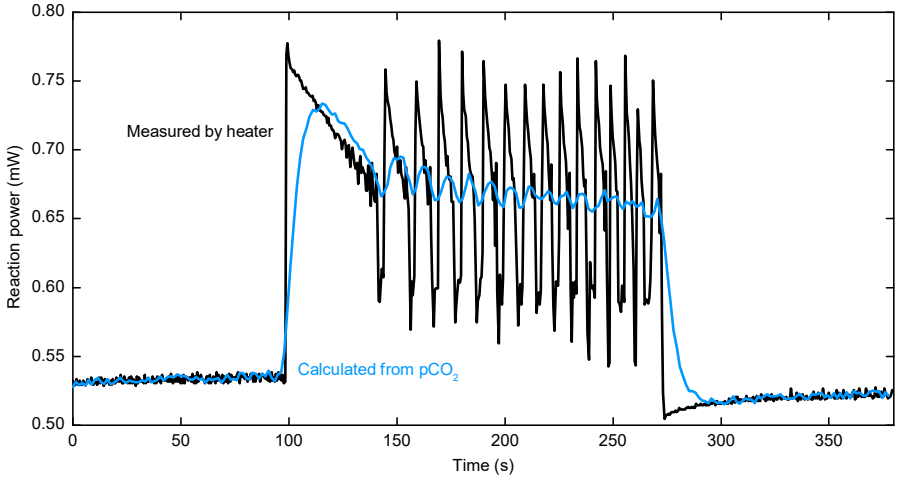

Figure 7.5. The heat of reaction determined from the CO_2 pressure as measured by the MS (blue curve) matches the heat of reaction measured from the heater power (black curve).

Oscillatory CO oxidation reaction

MS results demonstate periodic oscillations in O_2 and CO pressures, which are in anti-phase to similar variations in the CO_2 pressure (Fig. 7.6). These oscillations appeared spontaneously, or by imposing a minor temperature increase of 0.5-1.0 °C. The oscillations were observed at temperatures in the range of 386-456 °C (Fig. 7.8). This broad temperature range can be attributed to the effect of the nanoreactor loading and distribution of nanoparticles as well as reaction conditions and ageing times.

During the oscillatory reactions, the global nanoreactor temperature was kept constant by compensating the heat production by the exothermic reaction with a reduction in the heater power. The heater equilibrated within a few miliseconds, which is at least 3 orders of magnitude smaller than the time-scale of the observed

reaction oscillations. Therefore, the reaction oscillations occurred under constant temperature conditions[37] and the heater power measures the heat of reaction. These data provide calorimetric information (Fig. 7.6b). The heat of reaction oscillates asymetrically, showing a fast rise in CO conversion and a subsequent slower decay. The heat of reaction peaks at the maximum global reaction rate where the CO pressure is maximal. However, the minimum CO pressure observed is delayed by the residence time of the gas in the tubing from the nanoreactor to the MS and broadened by Taylor-Aris dispersion (Fig. 7.7), so the time-resolved CO pressure is smeared out in the MS as compared to the measured power (heater readout time, 0.5 s). Thus, the heat of reaction profile from the heater power variation provides a more distict fingerprint of the oscillatory reaction.

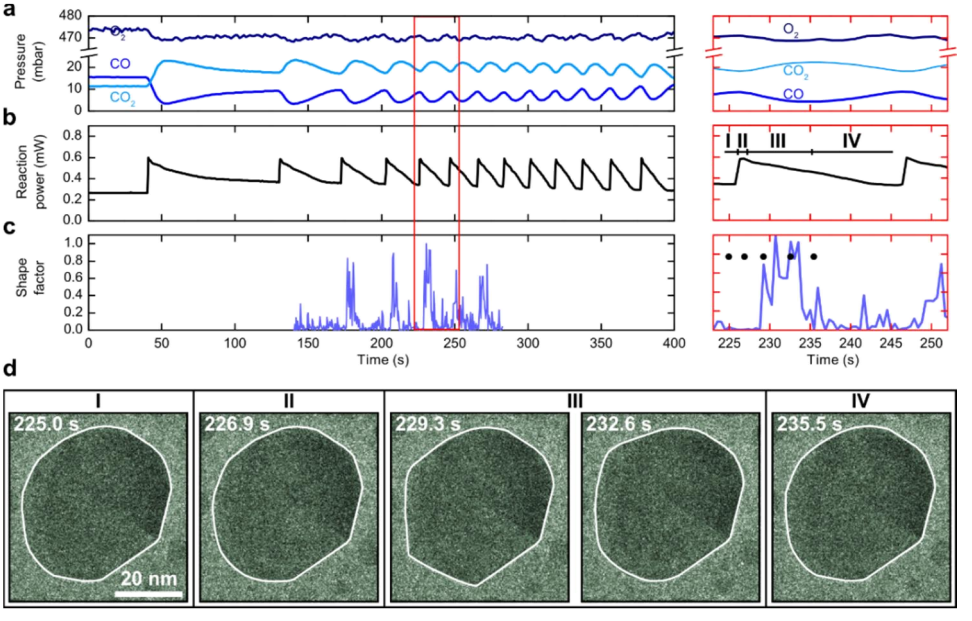

Figure 7.6. (a) Mass spectrometry of the CO, O_2 and CO_2 pressures; (b) The heat of reaction; (c) The shape factor α for the Pt nanoparticles as a function of time; (d) Time-resolved TEM images of a Pt nanoparticle at the reaction zone exit. The gas entering the reaction zone is 1 bar of gas mixture B.

The particles near the reaction zone entrance had a stationary and more spherical projected morphology during the oscillatory reaction. In contrast, the particles near the reaction zone exit switched between a more spherical and a more faceted projected morphology (Fig. 7.6d and movie 1[*]). The sequential images (Fig. 7.6d) show that particle shape I, II and IV are more spherical, while shape III is more faceted.

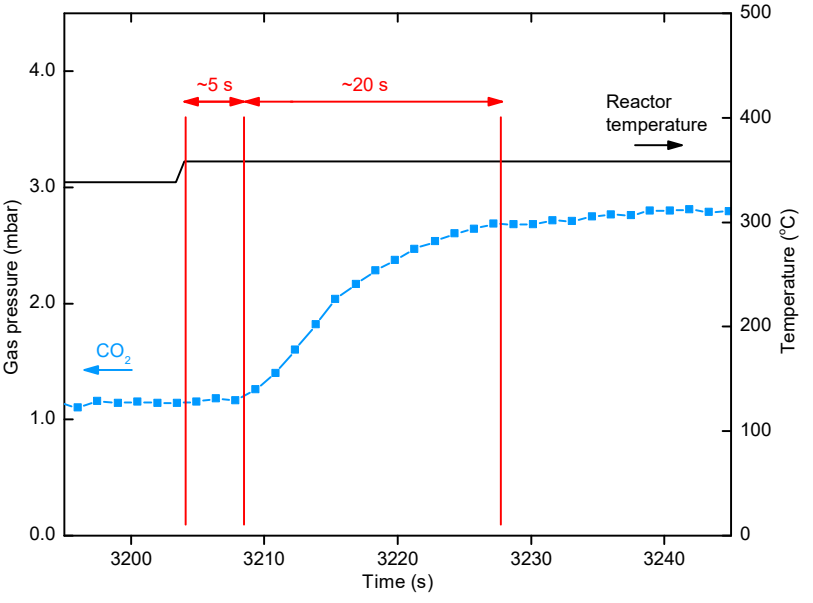

Figure 7.7. The delay of the concentration profiles between leaving the nanoreactor and reaching the MS, and their broadening. The CO_2 pressure increase is delayed by 5 s and broadened over a 20 s period before a constant value is established. As a result, the MS and heater power data are synchronised by subtracting 5 s from the MS computer clock time in order for the MS data to display the gas composition at the time when it exits the nanoreactor (and not when it enters the MS).

[*] http://www.nature.com/nmat/journal/v13/n9/abs/nmat4033.html

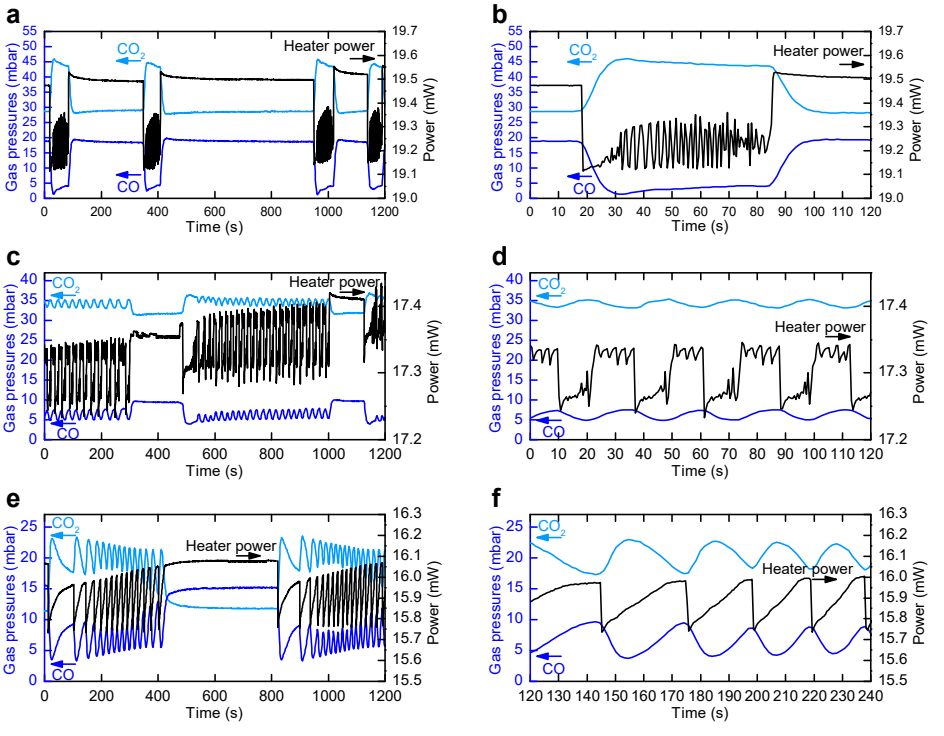

Figure 7.8. (a, b, e, f) The time-resolved partial pressure (*left axis*) and heater power data (*right axis*) during the oscillatory oxidation of CO from the first nanoreactor and (c, d) the second nanoreactor. (a, b) The first nanoreactor reaction zone was fed with 1 bar of gas mixture A at 455 °C. (c, d) The second nanoreactor was fed with the same gas mixture at 410 °C. (e, f) The first nanoreactor was also fed with 1 bar of gas mixture B at 386 °C.

In order to determine the temperature increase which induces the oscillation cycle, two different nanoreactors were exposed to three different reaction conditions. Fig. 7.8a, c, e show the time-resolved partial pressures and Fig. 7.8b, d, f show the heater power data from the experiments. The nanoreactor shown in Fig. 7.8a and b was exposed to 1 bar of gas mixture A at 455 °C. At t = 19 s and 951 s, the temperature was increased by 0.5 °C to induce an oscillatory cycle. At t = 342 s and 1142 s the oscillatory cycles initiated spontaneously. The nanoreactor shown in Fig. 7.8c and d was also exposed to 1 bar of gas mixture A, but at 410 °C. At t = 487 s and 746 s the temperature was increased by 0.5 °C to induce the oscillatory cycle. However, for this nanoreactor the spontaneous oscillation cycle was not

observed after this increase. Then at t = 1126 s, the temperature was increased by 1 ^{o}C. The oscillatory cycle was observed again. Fig. 7.8e and f show the results from the first nanoreactor exposed to 1 bar of gas mixture B at 386 ^{o}C. At t = 12 s and 822 s, the temperature was increased by 0.5 ^{o}C, which induces the oscillatory cycle. The images of Fig. 7.7d were recorded during this experiment.

Electron illumination studies

The Pt nanoparticles during the oscillatory reaction were monitored by the time-resolved TEM. The electron transparent observation windows were chosen both at the entrance and exit of the nanoreactor to represent the variation of gas composition across the reaction zone as CO was being converted. The image acquisition rate was 1-2 frames per second, faster than the rate of the oscillation reaction. This visualizes the state of the nanoparticles at this time-scale. The TEM images were acquired at electron-dose rates sufficiently low to avoid effects induced by the electron beam.

To study the effect of the electron beam on the dynamic behaviour of the Pt nanoparticles, a nanoreactor was exposed to different gas compositions. The first nanoreactor was exposed to 1 bar of gas mixture A while the second nanoreactor was exposed to 1 bar of gas mixture B and to pure O_2 at 500 ^{o}C.

The Pt particles in the nanoreactor exposed to the gas mixture A were imaged at electron dose-rates of 20, 50, 100, 200, 300 and 500 $e^{-}/Å^{2}s$. The TEM image series of the particles were acquired with 1s exposure time at a frame rate of 0.1 Hz over 10 minutes. At dose-rates of >100 $e^{-}/Å^{2}s$, the images reveal that a few nanoparticles are displaced in the projected image plane and retain the contrast at their edges. This indicates that the particles moved along the plane of the electron transparent window (Fig. 7.9 yellow and purple circles). Some particles disappeared or coalesced with larger nanoparticles (Fig. 7.9 blue circles). The number of displaced nanoparticles appeared to increase with the electron dose-rates in the interval 100-500 $e^{-}/Å^{2}s$. This indicates that the displacement of nanoparticles is an electron-beam induced phenomenon.

The TEM images of a Pt nanoparticle in the nanoreactor that was exposed to gas mixture B are presented in Fig. 7.6d and 7.10. The relation between CO conversion level and particle morphology during the CO oscillatory reaction is presented in Fig. 7.10. The images were taken at electron dose-rates of 5-200 $e^{-}/Å^{2}s$. The images reveal that the Pt nanoparticle has a more rounded shape (morphology 1) at low CO conversion level, and a more facetted shape (morphology 2) at high CO conversion level. Independent of the applied electron

dose-rates, these shape changes occur in a repeated and reversible fashion and synchronised with the global oscillatory reaction conditions.

Moreover, the Pt nanoparticle changes were only observed when the CO conversion exhibited the temporal oscillatory behaviour. The changes were absent in the periods with a constant CO conversion. The oscillatory reaction was observed regardless of whether the nanoreactor was being exposed to the electron beam. These observations suggest that the shape changes are linked to the oscillatory reaction conditions and are insensitive to the variations in the electron beam illumination conditions.

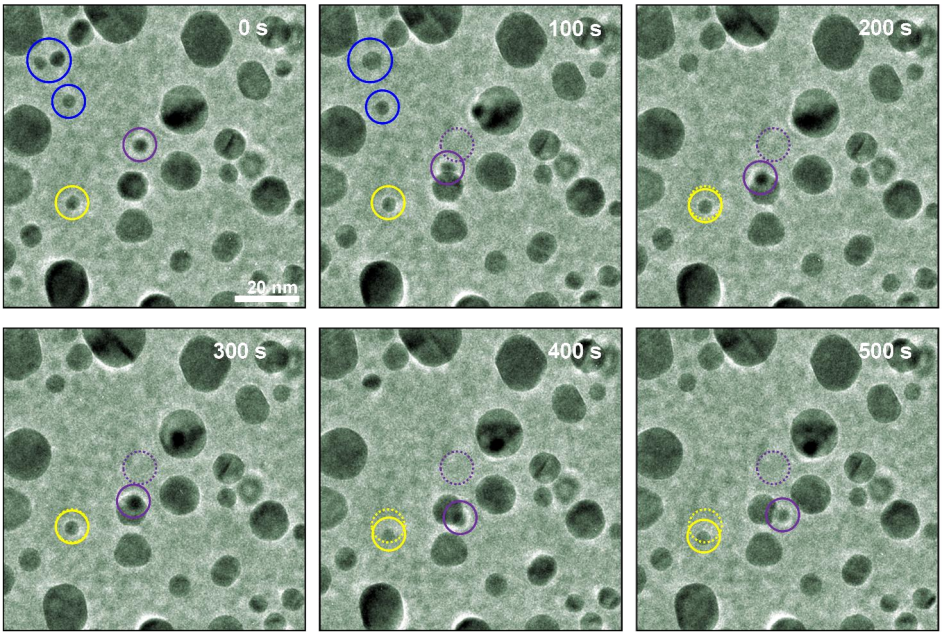

Figure 7.9. Time-resolved image series of a group of Pt nanoparticles. *Blue* circles show Pt nanoparticles that coalesce or disappear in time. *Yellow* circles (full) show a Pt nanoparticle that displaced from its original position (dashed). Purple circles indicate the displacement of a Pt nanoparticle positioned on the opposing window (having a strong bright Fresnel edge contrast). The images were obtained with an electron dose-rate of 500 $e^-/Å^2s$ and exposure time of 1 s during exposure of the reaction zone to 1 bar of gas mixture A at 415 ^oC.

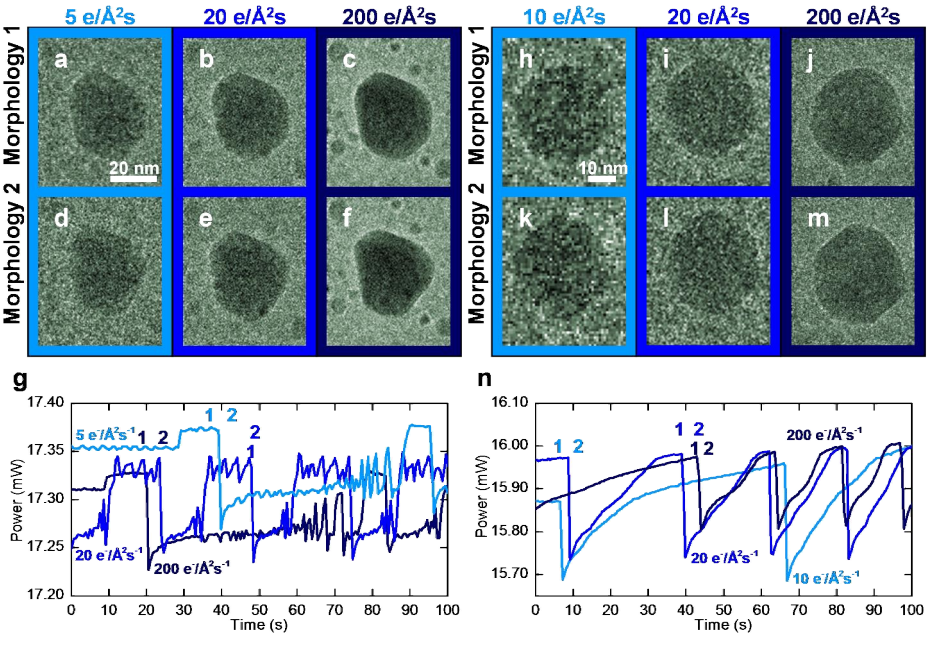

Figure 7.10. (a-c) TEM images of a Pt nanoparticle with a more rounded shape (morphology 1) at heater power (1) in the oscillatory regimes (g); (d-f) The same particle has a more facetted shape (morphology 2) at heater power (2) in the oscillatory regimes (g). These observations were performed using 1 bar of gas mixture A at 411 ^{o}C; (h-j) TEM images of a Pt nanoparticle with morphology 1 at heater power (1) in the oscillatory regimes (n) and (k-m) morphology 2 at heater power (2) in the oscillatory regimes (n). Images (h-n) were obtained with the nanoreactor exposed to 1 bar of gas mixture B.

The Pt nanoparticle shape changes apparently happened in a reversible way without an electron beam dependency. This suggests that the Pt transport involved in the shape change was also unaffected by the electron beam. Thus, the dynamic shape changes of the Pt nanoparticles appear to be coupled to the oscillatory CO oxidation reaction with the electron beam having a negligible effect on the oscillatory shape change for the applied illumination conditions (5-200 $e^{-}/Å^{2}s$). Even though low dose-rate electron beams can be used to study the Pt nanoparticle reaction-induced shape changes, these dose-rates resulted in an inferior image signal-to-noise ratio. Therefore the TEM images presented in this chapter were obtained at higher dose-rates in the range of 200-300 $e^{-}/Å^{2}s$.

Relation of the CO conversion and Pt nanoparticle shape changes

The Pt nanoparticle shape also changes at different CO conversion levels as shown in Fig. 7.11. 25 Pt nanoparticles were quantified to analyse the relation. The nanoparticle periphery from the low conversion state is compared with the periphery of the same nanoparticle from the high conversion state. Then the maximum edge distance between the actual periphery and the outlined periphery is identified (by the blue circle) and used as a simple descriptor (maximum edge deviation) for the shape change between the two states. Each measurement has an error bar ±2 pixels (1 pixel = 0.22 nm). The linear fit is included to mark the size-dependent trend of the shape changes. The changes are not detectable for nanoparticles below 10 nm. Large scattering in the maximum edge deviation appears for the bigger nanoparticles. This is likely due to the orientation and polycrystallinity of the nanoparticles.

The evaluation of the maximum edge distance shows that all the Pt nanoparticles with a diameter above 10 nm undergo dynamic shape changes during the oscillatory CO oxidation. Smaller diameter particles might undergo similar shape changes, but due to the low signal-to-noise ratio and the reduced pixel size used for the TEM image acquisition, the smaller nanoparticles appear stationary during the reaction.

As the CO conversion rate increases, the Pt nanoparticle starts to change shape from the more spherical shape to the more facetted shape within 3 s after the CO peak conversion (Fig. 7.7b-d, III). The time associated with the shape changes reflects both the mass transport of the Pt and the particular nanoparticle size and orientation, as the shape change appeared faster for the other nanoparticles at higher temperatures (Fig. 7.11 and 7.12). When the CO conversion rate decreases, the Pt nanoparticle transforms back to a more spherical shape (Fig. 7.2 b-d, IV) and retains that shape until the CO conversion rises steeply again. Thus, the nanoparticles near the reaction zone exit can undergo oscillatory and reversible shape changes with a temporal frequency matching the oscillations in heat of reaction (Fig. 7.12). This indicates that the oscillatory conversion of CO and the dynamic shape change of the Pt nanoparticles are, indeed, coupled.

To study the mechanism of the oscillatory reaction, the Pt nanoparticles are examined at the atomic scale (Fig. 7.12c-e and Fig. 7.13). The Pt nanoparticle shows crystalline lattice fringes with spacings corresponding to metallic Pt(111). But the presence of a surface oxide at the surface of the nanoparticle cannot be excluded[38]. The speckled contrast is due to electron scattering on the amorphous window material and the low electron-dose images.

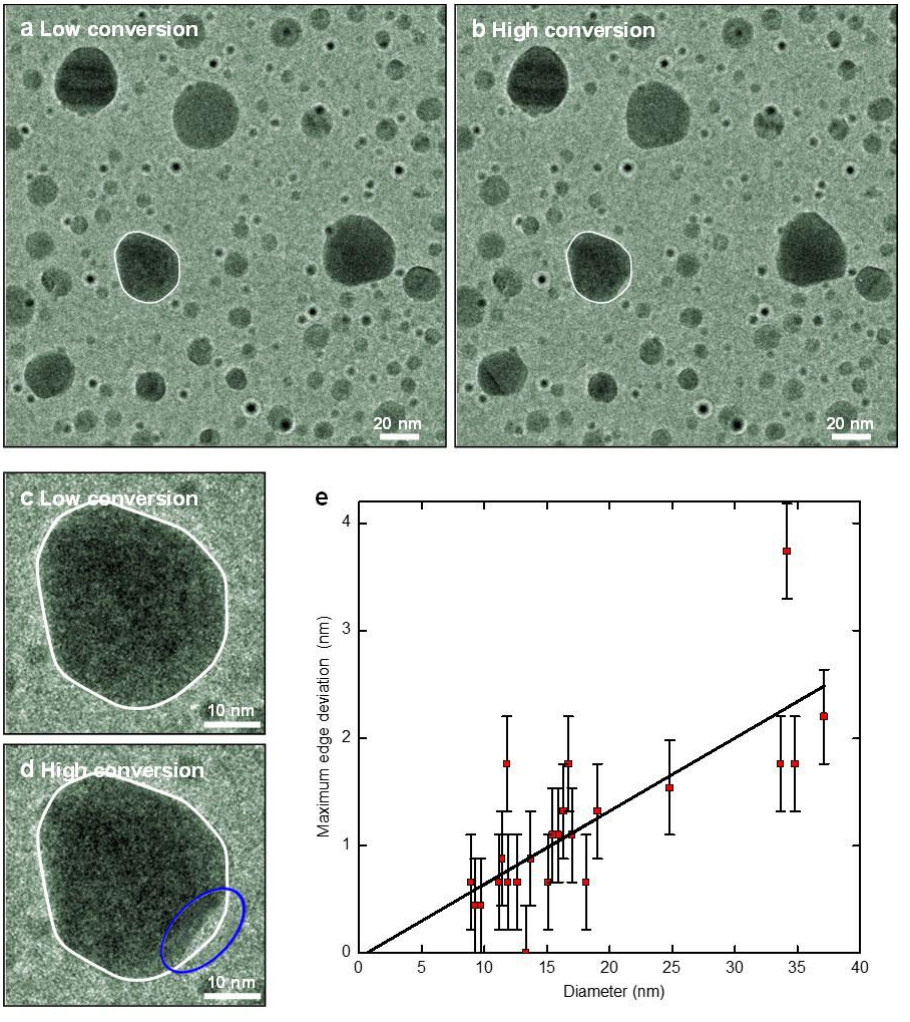

Figure 7.11. TEM images of Pt nanoparticles at (a) low and (b) high CO conversion of the reaction oscillation. For 25 nanoparticles, the shape change was quantified in the following way: (c) The periphery of the nanoparticle in the low conversion condition is outlined; (d) The line is used to outline the nanoparticles at high conversion. The maximum edge deviation of the line, highlighted by the blue circle, shows the shape change between the two states; (e) Maximum edge deviation versus the nanoparticle diameter. The nanoreactor reaction zone was exposed to 1 bar of gas mixture A at 411 ^{o}C.

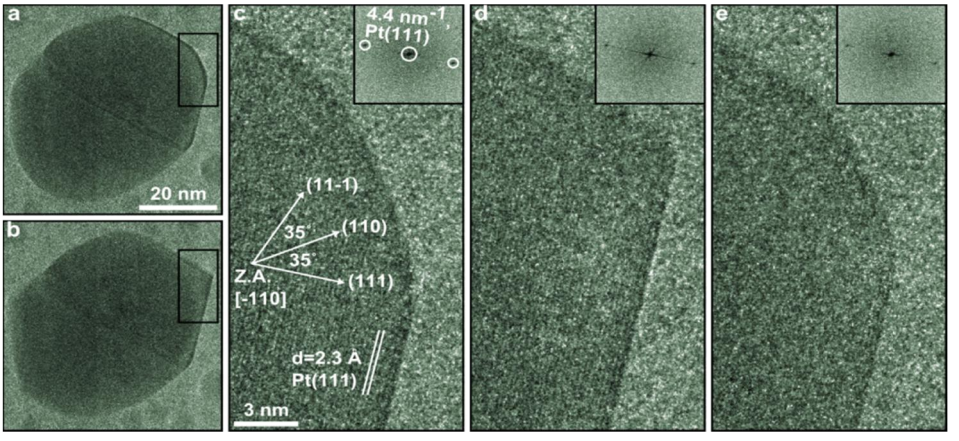

Figure 7.12. Time-resolved, high-resolution TEM images of a Pt nanoparticle at the gas exit of the reaction zone. The reaction zone was exposed to 1 bar of gas mixture A at 454 °C. The TEM images (a, c, e) show the more spherical shape and (b and d) the more facetted shape during the oscillatory reaction; (insets in c, d, e) Fast Fourier Transforms (FFT) reveal a lattice spacing corresponding to the Pt(111) lattice planes (movie 2[†])

[†] http://www.nature.com/nmat/journal/v13/n9/abs/nmat4033.html

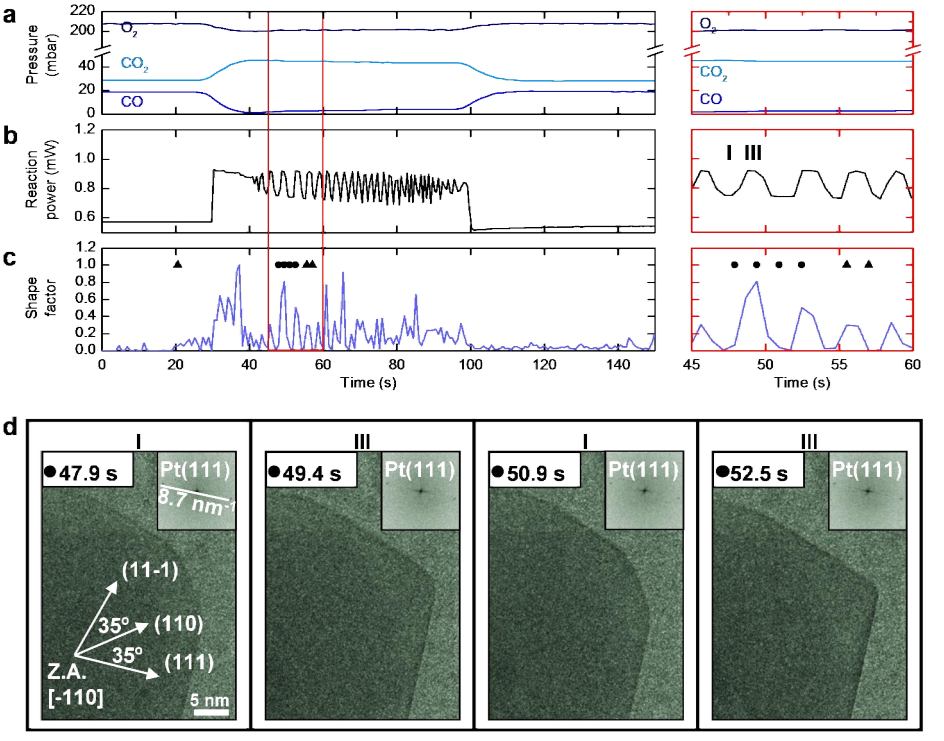

Figure 7.13. (a) MS data, (b) heat of reaction and (c) shape factor of the Pt nanoparticle of Fig. 7.12 and 7.14d during the reaction oscillation. The nanoreactor reaction zone was exposed to 1 bar of gas mixture A at 454 °C. High-resolution TEM images in Fig. 7.12 c, d and e were recorded during this sequence and the exact time for recording is indicated by triangles (▲) in (c); (d) Additional high-resolution TEM images taken at acquisition times marked with ● in (c).

The DFT calculations show that the close-packed facet α-PtO_2(0001) is unstable under these reaction conditions (T = 420 °C, P_{O2} = 0.21 bar, maximum oxygen chemical potential of $\Delta\mu$(O)=-0.83 eV[39]). Thus, the combination of DFT calculation and high-resolution TEM images indicates that the Pt nanoparticle remains in the metallic state under the reaction conditions. In a nanoreactor fed with 1 bar of O_2 at 300 °C ($\Delta\mu$(O) = -0.62 eV), the FFT of a Pt nanoparticle image shows that all of the nanoparticle lattice spots are consistent with metallic Pt and no indication of bulk platinum oxide was found (Fig. 7.14). Formation of surface oxide, however, cannot be excluded, as this technique does not visualise such a state[12,15,38].

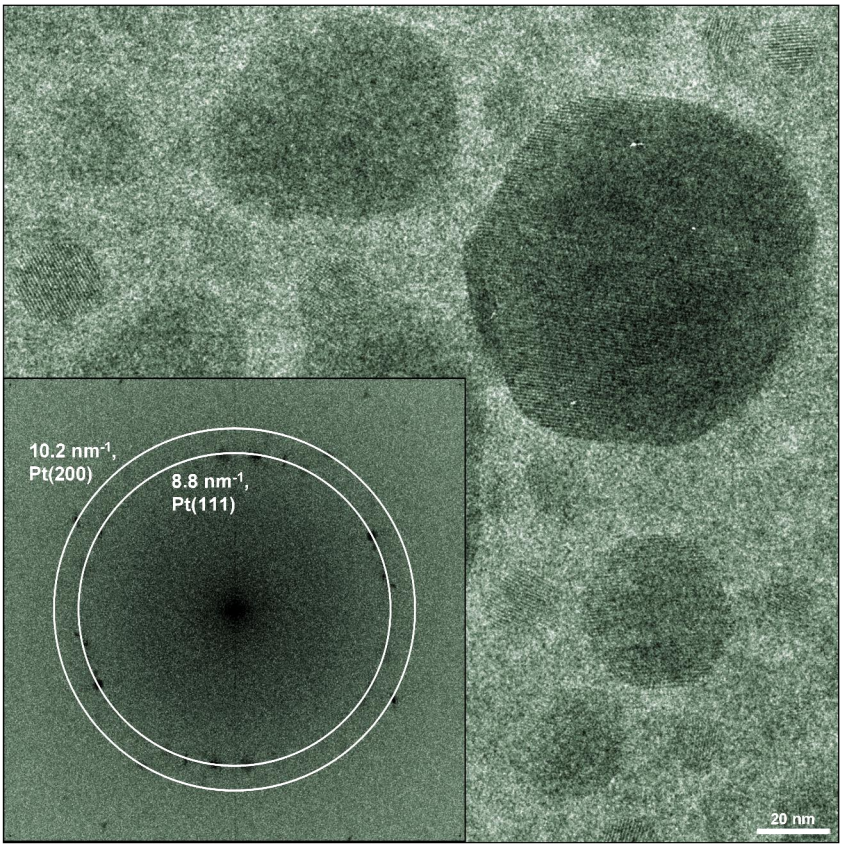

Figure 7.14. High-resolution TEM image of Pt nanoparticles during exposure to oxygen. The reaction zone was exposed to 1 bar of O_2 at 300 °C. The inset is a FFT of the image with white circles superimposed to indicate the lattice spacing of metallic Pt(111) and Pt(200) lattice planes. All lattice spots are consistent with metallic Pt and no indication of platinum oxide was found.

To analyse the response of the Pt nanoparticles to the CO-O_2 gas mixture, the presented micro-kinetic model based on ab initio DFT calculations of adsorption and transition state energy was used[33]. The more facetted nanoparticles are modelled by the Pt(111) facet and the more spherical nanoparticles are modelled by the Pt(211) facet. Each model describes the CO and O coverage (Fig. 7.15a) as well as the reaction rate for each site (Fig. 7.15b). The dependency on the CO pressure is emphasized, because O_2 is in excess in the gas phase and the CO pressure changes across the reaction zone (Fig. 7.1d and e). At high CO pressure

(P_{CO} > 1 mbar), the model shows that the (211) facet is almost fullly covered by CO whereas the (111) facet is only sparsely covered (Fig. 7.15a). The Pt surface sites are depleted in O. The (211) facet is therefore more stabilized than the (111) facet, because the CO adsorption is stronger at the (211) facet than at the (111) surface[33,40,41]. Therefore the more spherical shape of the Pt nanoparticle is expected at high CO pressure. At lower CO pressure (P_{CO} < 1 mbar), the (111) and (211) facets obtain a significant O coverage. As O binds more equally to both sites, the (111) facet is more stabilized. Therefore the more facetted shape is expected. Thus, the Pt nanoparticle shape change is attributed to the CO pressure variation in the presence of an O_2-rich CO-O_2 gas mixture.

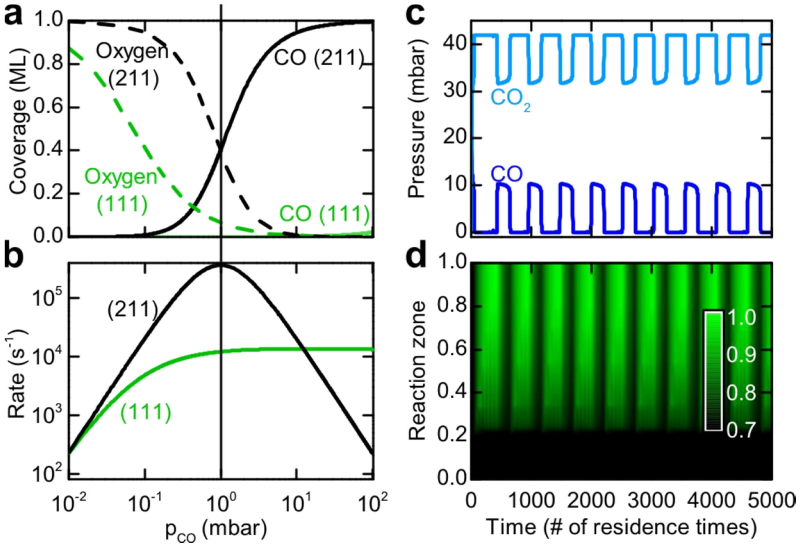

Figure 7.15. (a) CO and O coverage versus CO pressure at Pt(111) and Pt(211); (b) CO oxidation rate versus CO pressure at Pt(111) and Pt(211). T = 520 °C and P_{O2}= 210 mbar; (c) Time dependency of CO and CO_2 pressure at the reaction zone exit; (d) Time-dependency of the shape factor α along the entire reaction zone. (c) And (d) are both simulated using the one-dimensional convection-diffusion equation for the nanoreactor and the reaction rates from (b).

The gas-dependent shape of the Pt nanoparticles affects the CO conversion because the CO oxidation rate is site-dependent[42] and also depends on the position of the nanoparticles in the reaction zone (due to the CO conversion gradient along the gas flow). Thus, a time-dependent model is established based on a two-site micro-kinetic model and the description of mass-transport in the nanoreactor. The

model will allow to address whether the dynamic shape of the Pt nanoparticles represents a sufficient explanation for the reaction oscillations. Based on the model, the step site is more active at the lower CO pressure. The activity decreases at higher temperatures. The (111) facet site activity remains constant over the whole CO pressure range (Fig. 7.15b). The calculation of the shape factor (α) from the reaction rate data of both sites results in $\alpha = 1$ for the facetted morphology (at $P_{CO} < 1$ mbar) and $\alpha = 0.7$ for the rounded morphology (at $P_{CO} > 1$ mbar). Combining the two-site model for the Pt morphology and reaction rate with a convection-diffusion equation, which approximates the nanoreactor by a one-dimensional gas environment (Eqs. 7.4 and 7.5), allows the time-dependent simulation of the partial pressure and shape factor throughout the nanoreactor channel at conditions similar to those of Fig. 7.12.

The simulation results are presented in Figs. 7.15c and d. The time-dependency of the CO and CO_2 pressure at the reaction zone exit shows a periodic variation in time (Fig. 7.15c). The shape factor across the reaction zone remains constant in time at the reaction zone entrance ($P_{CO} > 1$ mbar, $\alpha = 0.7$). The nanoparticles in this area have a spherical shape. Towards the reaction zone exit, the shape descriptor gradually follows a temporal variation between a more facetted and a spherical shape (Fig. 7.15d). The temporal variation in the shape factor matches the variation in CO pressure.

The solution for the CO pressure with a fixed α always approaches the steady-state condition. Fig. 7.16a shows the time-dependent model of CO pressure under steady-state conditions. The steady-state is reached within 30-100 residence times. The black line corresponds to the CO pressure at the reaction zone exit during one oscillation period for the reaction condition and reactor geometry described in Fig. 7.15c. The blue triangles correspond to the steady-state condition for an initial CO pressure of 42 mbar (the boundary condition used). The steady-state condition is obtained with the lowest CO conversion. The red circles correspond to the steady-state for an initial CO pressure of 4.2×10^{-5} mbar. The steady-state condition is obtained with the highest CO conversion. The black crosses correspond to the initial CO pressure in Fig. 7.15c. Based on the steady-state point arrangement on the black line, the steady-state conditions deviate from the bistable situation at times $t = 3420$ s and 3794 s. The results deviate from Fig. 7.15c (black line) in such a way that the steep decrease in the CO pressure ($t = 3420$) and the steep rise in the CO pressure ($t = 3790$) follow the deviation. The steep rise and fall in the CO pressure can thus be explained as the nanoreactor shifting from a high to a low conversion state and vice versa.

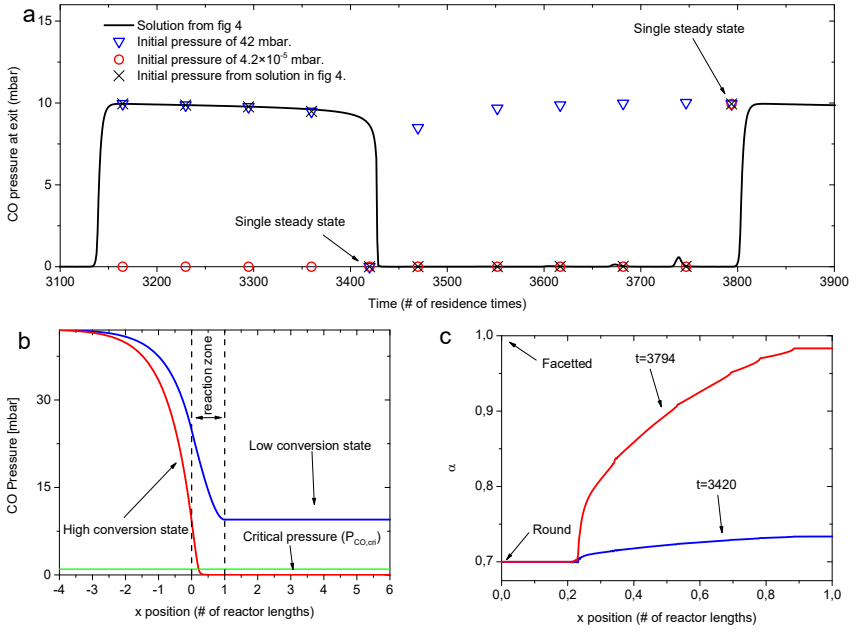

Figure 7.16. (a) The time-dependent model solution of CO pressure at the reaction zone exit during one oscillation period for the reaction conditions and reaction geometry described in Fig. 7.15. The *black* line denotes the CO pressure. By freezing the α distribution in time (corresponding to t = 3360), the following steady-states are obtained: *Blue* triangles correspond to an initial CO pressure of 42 mbar, *red* circles correspond to an initial CO pressure of 4.2×10^{-5} mbar, and the *black* crosses correspond to the initial CO pressure of Fig. 7.15; (b) Two steady-state CO pressure profiles through the nanoreactor obtained from the steady-states in (a). The *blue* line corresponds to a low conversion state and the *red* line corresponds to a high conversion state. The CO pressure corresponding to a change in the equilibrium shape of the particles is 1 mbar (*green* line). The reaction zone is located within the *black* dashed vertical lines; (c) The α distribution in the nanoreactor, taken from Fig. 7.15d, at the times for a steep fall in CO pressure (t = 3420, *blue* line) and a rise in CO pressure (t = 3794, *red* line). At t = 3420, the nanoparticles are almost round along the entire nanoreactor. At t = 3794, the nanoparticle shape goes from rounded to facetted along the nanoreactor.

7.4 Conclusions

The presented results show that in-situ TEM is a very useful method to study a catalytic reaction under reaction conditions. The in-situ TEM experiments were performed using the latest development of an in-situ TEM nanoreactor, which has a higher channel height to simplify the catalyst loading but does not compromise much the image resolution since the presence of pillars suppress bulging effects of the membrane windows.

Combined with the MS analysis of the products, the experiments showed that during catalytic reaction the Pt nanoparticles undergo dynamic shape changes up to several nanometers, much more than earlier reported surface reconstruction[12]. These shape changes oscillate following the CO conversion oscillation in the nanoreactor. Even though the observation is only focused on the larger particles (>~10 nm), the oscillation might also happen on the smaller particles. The reaction oscillations may also be associated with additional complexity under some reaction conditions. For example, in-plane restructuring[12] or oxide formation[15,38] could contribute to the oscillatory CO conversion as well. In the presence of a CO-O_2 gas mixture, at the high CO pressure the Pt surface is in the form of (211) facets rather than (111) facets.

The time-dependent microkinetic model captures the observations of the Pt nanoparticles during the oscillatory reaction at the reaction zone entrance and exit. This also demonstrates that a dynamic and reversible refacetting of Pt nanoparticles represents a mechanism that causes periodic transitions in the CO conversion in a bistable reaction.

Although such in-plane dynamical effects remain unresolved in the present high-resolution TEM images, they are not required to obtain a consistent explanation of the observed reaction oscillations. Moreover, the nanoreactor approach is a beneficial complement to the multitude of in-situ and operando techniques[6-10] used for uncovering gas-surface phenomena under meaningful conditions in heterogeneous catalysis and nanoparticle research, because it helps to extend the description of dynamic properties and functions with information specific to the exposed surface sites.

7.5 References

1 Nørskov, J. K., Bligaard, T., Rossmeisl, J. & Christensen, C. H. Towards the computational design of solid catalysts. *Nat. Chem.* **1**, 37-46 (2009).

2 Newton, M. A., Belver-Coldeira, C., Martínez-Arias, A. & Fernández-García, M. Dynamic in situ observation of rapid size and shape change of

supported Pd nanoparticles during CO/NO cycling. *Nat. Mater.* **6**, 528-532 (2007).

3 Tao, F., Grass, M. E., Zhang, Y., Butcher, D. R., Renzas, J. R., Liu, Z., Chung, J. Y., Mun, B. S., Salmeron, M. & Somorjai, G. A. Reaction-driven restructuring of Rh-Pd and Pt-Pd core-shell nanoparticles. *Science* **322**, 932-934 (2008).

4 Yoshida, H., Matsuura, K., Kuwauchi, Y., Kohno, H., Shimada, S., Haruta, M. & Takeda, S. Temperature-dependent change in shape of platinum nanoparticles supported on CeO_2 during catalytic reactions. *Appl. Phys. Exp.* **4** (2011).

5 Hansen, P. L., Wagner, J. B., Helveg, S., Rostrup-Nielsen, J. R., Clausen, B. S. & Topsoe, H. Atom-resolved imaging of dynamic shape changes in supported copper nanocrystals. *Science* **295**, 2053-2055 (2002).

6 Boyes, E. D. & Gai, P. L. Environmental high resolution electron microscopy and applications to chemical science. *Ultramicroscopy* **67**, 219-232 (1997).

7 Thomas, J. M. & Somorjai, G. A. *Top. Catal.* **8**, 1-140 (1999).

8 Campbell, C. T. Catalysts under pressure. *Science* **294**, 1471-1472 (2001).

9 Buurmans, I. L. C. & Weckhuysen, B. M. Heterogeneities of individual catalyst particles in space and time as monitored by spectroscopy. *Nat. Chem.* **4**, 873-886 (2012).

10 Topsøe, H. Developments in operando studies and in situ characterization of heterogeneous catalysts. *J. Catal.* **216**, 155-164 (2003).

11 Freund, H. J., Meijer, G., Scheffler, M., Schlögl, R. & Wolf, M. CO oxidation as a prototypical reaction for heterogeneous processes. *Angew. Chem. Int. Ed.* **50**, 10064-10094 (2011).

12 Imbihl, R. & Ertl, G. Oscillatory kinetics in heterogeneous catalysis. *Chem. Rev.* **95**, 697-733 (1995).

13 Liauw, M. A., Plath, P. J. & Jaeger, N. I. Complex oscillations and global coupling during the catalytic oxidation of CO. *J. Chem. Phys.* **104**, 6375-6386 (1996).

14 Matera, S. & Reuter, K. Transport limitations and bistability for in situ CO oxidation at RuO_2 (110): First-principles based multiscale modeling. *Phys. Rev. B* **82** (2010).

15 Turner, J. E., Sales, B. C. & Maple, M. B. Oscillatory oxidation of Co over a Pt catalyst. *Surf. Sci.* **103**, 54-74 (1981).

16 Hendriksen, B. L. M., Bobaru, S. C. & Frenken, J. W. M. Bistability and oscillations in CO oxidation studied with scanning tunnelling microscopy inside a reactor. *Catal. Today* **105**, 234-243 (2005).

17 Harris, P. J. F. Sulphur-induced faceting of platinum catalyst particles. *Nature* **323**, 792-794 (1986).
18 Gontard, L. C., Chang, L. Y., Hetherington, C. J. D., Kirkland, A. I., Ozkaya, D. & Dunin-Borkowski, R. E. Aberration-Corrected Imaging of Active Sites on Industrial Catalyst Nanoparticles. *Angew. Chem. Int. Ed.* **46**, 3683-3685 (2007).
19 Hansen, L. P., Ramasse, Q. M., Kisielowski, C., Brorson, M., Johnson, E., Topsøe, H. & Helveg, S. Atomic-scale edge structures on industrial-style MoS_2 nanocatalysts. *Angew. Chem. Int. Ed.* **50**, 10153-10156 (2011).
20 Giorgio, S., Sao Joao, S., Nitsche, S., Chaudanson, D., Sitja, G. & Henry, C. R. Environmental electron microscopy (ETEM) for catalysts with a closed E-cell with carbon windows. *Ultramicroscopy* **106**, 503-507 (2006).
21 Creemer, J. F., Helveg, S., Hoveling, G. H., Ullmann, S., Molenbroek, A. M., Sarro, P. M. & Zandbergen, H. W. Atomic-scale electron microscopy at ambient pressure. *Ultramicroscopy* **108**, 993-998 (2008).
22 Creemer, J. F., Santagata, F., Morana, B., Mele, L., Alan, T., Iervolino, E., Pandraud, G. & Sarro, P. M. An all-in-one nanoreactor for high-resolution microscopy on nanomaterials at high pressures. *Proc. IEEE Micr. Elect.*, (2011), 1103-1106, ISBN: 978-1-4244-9632-7.
23 Allard, L. F., Overbury, S. H., Bigelow, W. C., Katz, M. B., Nackashi, D. P. & Damiano, J. Novel MEMS-based gas-cell/heating specimen holder provides advanced imaging capabilities for in situ reaction studies. *Microsc. Microanal.* **18**, 656-666 (2012).
24 Baker, R. T. K. In Situ Electron Microscopy Studies of Catalyst Particle Behavior. *Catal. Rev.* **19**, 161-209 (1979).
25 Sharma, R. & Crozier, P. A. Handbook of microscopy for nanotechnology (Kluwer Academic Publisher, 2005), 531, ISBN: 1-4020-8003-4.
26 Chenna, S. & Crozier, P. A. In situ environmental transmission electron microscopy to determine transformation pathways in supported Ni nanoparticles. *Micron* **43**, 1188-1194 (2012).
27 Williamson, M. J., Tromp, R. M., Vereecken, P. M., Hull, R. & Ross, F. M. Dynamic microscopy of nanoscale cluster growth at the solid-liquid interface. *Nat. Mater.* **2**, 532-536 (2003).
28 Robertson, J. K. Modeling a microfluidic system using Knudsen's empirical equation for flow in the transition regime. *J. Vac. Sci. Tech. A* **19**, 358-364 (2001).
29 Vendelbo, S. B., Kooyman, P. J., Creemer, J. F., Morana, B., Mele, L., Dona, P., Nelissen, B. J. & Helveg, S. Method for local temperature measurement in a nanoreactor for in situ high-resolution electron microscopy. *Ultramicroscopy* **133**, 72-79 (2013).

30 Jinschek, J. R. & Helveg, S. Image resolution and sensitivity in an environmental transmission electron microscope. *Micron* **43**, 1156-1168 (2012).
31 http://www.mathworks.se/help/pde/ug/pdenonlin.html (consulted 15-1-2016).
32 Danckwerts, P. V. Continuous Flow Systems - Distribution of Residence Times. *Chem. Eng. Sci.* **2**, 1-13 (1953).
33 Jiang, T., Mowbray, D. J., Dobrin, S., Falsig, H., Hvolbœk, B., Bligaard, T. & Nørskov, J. K. Trends in CO oxidation rates for metal nanoparticles and close-packed, stepped, and kinked surfaces. *J. Phys. Chem. C* **113**, 10548-10553 (2009).
34 http://webbook.nist.gov/chemistry/ (consulted 15-1-2016).
35 Schmidt, L. D. *The engineering of chemical reactions*. (Oxford University Press, USA, 2004), ISBN: 0195169255.
36 http://mathworks.se (consulted 15-1-2016).
37 Jensen, R., Andersen, T., Nierhoff, A., Pedersen, T., Hansen, O., Dahl, S. & Chorkendorff, I. Self-sustained carbon monoxide oxidation oscillations on size-selected platinum nanoparticles at atmospheric pressure. *Phys. Chem. Chem. Phys.* **15**, 2698-2702 (2013).
38 Ackermann, M. D., Pedersen, T. M., Hendriksen, B. L. M., Robach, O., Bobaru, S. C., Popa, I., Quiros, C., Kim, H., Hammer, B., Ferrer, S. & Frenken, J. W. M. Structure and reactivity of surface oxides on Pt(110) during catalytic CO oxidation. *Phys. Rev. Lett.* **95**, 1-4 (2005).
39 Li, W. X., Österlund, L., Vestergaard, E. K., Vang, R. T., Matthiesen, J., Pedersen, T. M., Lægsgaard, E., Hammer, B. & Besenbacher, F. Oxidation of Pt(110). *Phys. Rev. Lett.* **93**, 146104-1 - 146104-4, (2004).
40 Thostrup, P., Christoffersen, E., Lorensen, H. T., Jacobsen, K. W., Besenbacher, F. & Nørskov, J. K. Adsorption-induced step formation. *Phys. Rev. Lett.* **87**, 126102/1 - 126102/4, (2001).
41 Tao, F., Dag, S., Wang, L. W., Liu, Z., Butcher, D. R., Bluhm, H., Salmeron, M. & Somorjai, G. A. Break-up of stepped platinum catalyst surfaces by high CO coverage. *Science* **327**, 850-853 (2010).
42 Vogel, D., Spiel, C., Suchorski, Y., Trinchero, A., Schlögl, R., Grönbeck, H. & Rupprechter, G. Local catalytic ignition during CO oxidation on low-index Pt and Pd surfaces: A combined PEEM, MS, and DFT study. *Angew. Chem. Int. Ed.* **51**, 10041-10044 (2012).

Summary

Towards in-situ TEM

The objectives of this PhD project are to address the challenges of in-situ TEM and introduce a new generation of in-situ TEM equipment. In Chapter 2 the in-situ TEM facilities are introduced, focusing on the nanoreactor that has gone through quite some development stages during this project. Several types of in-situ TEM nanoreactors were fabricated using Microelectromechanical Systems (MEMS) technology, which enables miniaturisation of the complete catalytic reactor (reactor column, heating system and gas system). The different generations of nanoreactors are the glued nanoreactor (GNR), the wafer bonded nanoreactor (WBNR) and the surface micromachined nanoreactor (SMNR).

The various development stages of the nanoreactor are based on the effort to solve problems occurring during the in-situ experiments. Some of these problems are addressed in Chapter 3 and 4. The first problem is the hydrocarbon contamination, which has been one of the major issues during imaging under the TEM (Chapter 3). Contamination in the TEM is a deposition of carbon, from the cracking of hydrocarbons under the electron beam, on the surface of the sample that thickens the sample area, leading to loss of contrast and masking of the fine details. The origin of the contamination can be the sample or the equipment used during the experiment. Recent TEM technology provides good vacuum systems, which decreases the possibility of contamination from the TEM equipment. Therefore, precautions should be taken during preparation and handling of the sample to minimise the introduction of contamination. The hydrocarbon contamination can be described as a result of hydrocarbon surface diffusion from the high concentration area (surrounding the illumination area) to the lower concentration area (inside the illumination area). The contamination usually forms a ring-like or a more uniform circular shape, depending on the electron beam intensity.

During fabrication of the GNR, an epoxy resin is used to glue together two silicon wafers to form a complete nanoreactor. The epoxy resin turns out to be an origin of contamination during in-situ TEM experiments. These results led to the development of the WBNR, for which silicon fusion bonding is used instead of epoxy resin to bind the two silicon wafers. The hydrocarbon contamination is no longer observed. The WBNR has a 2 μm channel height. The higher the nanoreactor channel height, the higher the probability of electron beam scattering and the danger of membrane bulging, which disturb the imaging process. Therefore, a nanoreactor fabricated using surface micromachining (SMNR) is developed to replace the WBNR. This technique does not induce contamination and enables decreasing the nanoreactor channel height down to 0.5 μm.

The second challenge for realising an in-situ TEM experiment is loading the nanoreactor. The challenging goal of the loading process is to get the sample in the TEM observation area, in the centre of the nanoreactor and in the narrow channels (2 μm for WBNR and 0.5 μm for SMNR). Even though the catalyst sample is usually introduced in the form of a suspension, channel clogging due to catalyst particle agglomeration can happen. Flow imaging techniques are used to visualise the flow of polystyrene suspensions (as a model for the catalyst suspension) during loading into the nanoreactor (Chapter 4). Information about particle velocity, distribution, channel defects and blocking can be obtained. Evidently, the flow of the suspension into the nanoreactor depends on the particle size and concentration. The 0.25, 0.5 and 1 μm particles flow relatively smoothly into the 2 μm WBNR channel. 10% (v/v) of 0.25 μm particles causes blockage near the inlet of the 0.5 μm channel of the SMNR. This is due to the presence of pillars and plugs along the channel. The pillars are present to increase the stiffness of the channel and to reduce membrane bulging when gas is introduced into the channel. The placement of the pillars hampers the flow of the suspension. The plugs are small holes formed during the SMNR fabrication that trap the polystyrene particles. Loading the system with a lower suspension concentration (2% v/v) solves the blockage problem. Results from the loading experiments lead to the fabrication of a new generation of SMNR. The new SMNR design has a larger channel height (4.5 μm). This simplifies the suspension loading without decreasing the image resolution because the arrays of pillars along the channel still reduce the bulging effect.

The ex-situ, quasi in-situ and in-situ TEM methods

TEM is one of the most important techniques for catalyst characterization. TEM is normally used in the ex-situ mode. For ex-situ TEM, the catalytic reaction is performed outside the TEM, then a small amount of the sample is taken out from the reactor for observation under the TEM. In Chapter 5, capping agent removal from gold nanoparticles is studied using this method. Gold nanoparticles are synthesised via a colloidal method using dodecylamine (DDA) as the capping agent. Then the catalyst nanoparticles are immobilized on an Al_2O_3 support using impregnation to form Au-DDA/Al_2O_3 catalysts. Ozone treatment at room temperature for 8 h is proven to be the optimal condition to remove the capping agent. The FTIR data confirm that DDA has been removed from the Au surface. After capping agent removal, the Au/Al_2O_3 particles undergo a slight sintering but the Au nanoparticle crystallinity is retained. The stability of the nanoparticles is tested during selected catalytic reactions: CO oxidation and benzyl alcohol oxidation. The TEM images show that both capped and un-capped nanoparticles sinter during high temperature CO oxidation. But the activity of both nanoparticle

types is similar due to their similar particle size. The advantage of the ex-situ TEM method is that it is easy to perform. A disadvantage is, however, that the sample observation is only performed before and after reaction, so the information during the catalytic reaction is missing. Furthermore, the sample is also directly exposed to ambient air during transport to the TEM for imaging, which (for some sensitive catalysts) can really affect the nature of the catalysts.

The quasi in-situ method can be an option to overcome this problem. Similar to the ex-situ method, in the quasi in-situ method, the catalytic reaction is performed outside the TEM, then a small amount of sample is taken out from the reactor for observation. The difference is that the sample is being kept in a specially developed protective atmosphere transfer specimen holder during transfer to the TEM, which prevents the sample to have contact with air. As an example in Chapter 6, the reduction of Pt/Al_2O_3 and Pd/Al_2O_3 catalysts is studied using quasi in-situ TEM. In order to capture the whole reduction process observed by the TEM, the reduction experiments are divided into several temperature increase steps. The sample is taken out of the reactor after every step and is then transferred to the TEM for imaging using the protective atmosphere transfer holder. The Quantifoil® microgrid carbon film on a mixed mesh Au TEM grid enables us to observe the same observation area and particles after each step. Therefore, we can get the sequential images from each step, which represent the changes of the nanoparticles during the reduction process. The particle size of Pt in Pt/Al_2O_3 increases after introduction of H_2 at room temperature and with increasing reduction temperature. The Pd particle size in Pd/Al_2O_3 also increases when the reduction temperature is increased from room temperature to 50 ^{o}C. However, the particle size remains the same when the reduction temperature is increased further. One of the advantages of this method is the ability to monitor the particle changes during e.g. the catalyst activation, while the disadvantage is that the method is quite laborious.

In Chapter 7, the in-situ TEM method is finally demonstrated to overcome the disadvantages of quasi in-situ TEM. In in-situ TEM, the catalytic reaction is performed inside the TEM equipped with a gas supply system, the last generation of the nanoreactor (SMNR) and a mass spectrometer. The TEM imaging enables us to visualise the catalytic reaction at reaction conditions, and at the same time, the reaction product mixture can be analysed. Reaction calorimetry is also measured from the changes in the supplied power to the Mo-heater. The reaction studied is the oscillatory oxidation of CO on the Pt nanoparticles. Several sets of experiments are performed to study the platinum nanoparticle changes during the reaction. The oscillations in O_2 and CO atmospheres were observed at temperatures in the range of 386-456 ^{o}C. During the oscillations, TEM imaging shows that the particles near the reaction zone entrance had a stationary and more

spherical morphology while the particles near the reaction zone exit switched between a more spherical (Pt 211) and a more faceted (Pt 111) projected morphology. The possible effect of the electron beam is analysed by imaging the nanoreactor at constant temperature under variations of beam exposure. Regardless of whether the nanoreactor is being exposed to the electron beam or not, the oscillatory reaction is still observed. These observations suggest that the platinum shape changes are linked to the oscillatory reaction conditions and are insensitive to the variations in the electron beam illumination conditions. The relation between CO conversion and shape changes of the Pt nanoparticles is also studied. When the CO conversion increases during the oscillatory reaction the nanoparticle shape is more faceted, while when the conversion rate decreases the Pt nanoparticle shape is more spherical. The results indicate that the oscillatory conversion of CO relates to the platinum nanoparticle morphology changes.

These significant results obtained using in-situ TEM show the importance and power of using in-situ TEM to obtain a better understanding of the catalytic process.

Samenvatting

Op weg naar in-situ TEM

Dit proefschrift behandelt de uitdagingen van in-situ TEM en introduceert een nieuwe generatie in-situ TEM-apparatuur. Deze apparatuur wordt in Hoofdstuk 2 beschreven, met de nadruk op de nanoreactor die in de loop van dit project een lang ontwikkelingstraject heeft doorlopen. Verschillende in-situ nanoreactoren zijn gefabriceerd door middel van MicroElectroMechanische Systeem (MEMS) technologie. Hiermee kan de complete reactor (reactor kolom, verwarming en gassysteem) geminiaturiseerd worden. De verschillende generaties nanoreactoren zijn de gelijmde nanoreactor (GNR), de 'wafer bonded' nanoreactor (WBNR) en de nanoreactor gemaakt met oppervlakte microfabricage (SMNR).

De verschillende ontwikkelingsfasen van de nanoreactor zijn gebaseerd op het oplossen van de problemen die tijdens de in-situ experimenten optraden. Enkele van deze problemen worden besproken in Hoofdstuk 3 en 4. Het eerste probleem is koolstofcontaminatie, wat een van de grootste problemen is bij het gebruik van de TEM (Hoofdstuk 3). Contaminatie in de TEM is de afzetting van koolstof op het oppervlak van het monster door het kraken van koolwaterstoffen in de elektronenbundel. Dit leidt tot verlies van contrast en details in de afbeeldingen, doordat het monster steeds dikker wordt. De oorsprong van de contaminatie kan in het monster of in de apparatuur liggen. Huidige TEMs zijn voorzien van goede vacuümsystemen, wat de contaminatie vanuit de apparatuur doet afnemen. Derhalve moeten tijdens het voorbereiden en manipuleren van het monster maatregelen genomen worden om zo min mogelijk contaminatie te introduceren. De contaminatie ontstaan door koolwaterstoffen kan worden beschreven als het resultaat van diffusie van gebieden met een hogere concentratie koolwaterstof (buiten het bestraalde gebied) naar het gebied met een lage concentratie (het bestraalde gebied). De contaminatie vormt meestal een ring of een meer uniforme cirkel, afhankelijk van de intensiteit van de elektronenbundel.

Voor de fabricage van de GNR wordt een epoxyhars gebruikt om twee silicium wafers aan elkaar te lijmen zodat een complete nanoreactor ontstaat. De epoxyhars blijkt een bron van contaminatie te zijn tijdens in-situ TEM experimenten. Deze constatering heeft geleid tot de ontwikkeling van de WBNR, waarvoor silicium fusie technologie gebruikt wordt in plaats van epoxyhars om de beide silicium wafers aan elkaar te verbinden. Hiermee is de koolwaterstof contaminatie verdwenen. De kanaalhoogte van de WBNR is 2 μm. Hoe hoger het kanaal in de nanoreactor is, hoe groter de kans op elektronenbundel verstrooiing en het gevaar van opbolling zijn. Deze fenomenen verstoren het afbeeldingsproces. Daarom is

de WBNR vervangen door de SMNR. Oppervlakte microfabricage introduceert geen contaminatie en kan een kanaalhoogte van 0.5 μm opleveren.

De tweede uitdaging voor het uitvoeren van in-situ TEM experimenten is het laden van de nanoreactor. De uitdaging van het laadproces is om het monster in het observatiegebied te plaatsen, in het midden van de nanoreactor en in de nauwe kanalen (2 μm voor de WBNR en 0.5 μm voor de SMNR).

Ook al wordt de katalysator meestal geladen als een suspensie, toch kan het kanaal verstopt raken door agglomeratie van katalysatordeeltjes. Als model voor de katalysatorsuspensie is de stroming van polystyreen suspensies in beeld gebracht tijdens het laden van de nanoreactor (Hoofdstuk 4). De snelheid en de verdeling van de deeltjes, en defecten en blokkades in het kanaal kunnen zo bestudeerd worden. Uiteraard hangt de stroming van de suspensie in de nanoreactor af van de deeltjesgrootte en -concentratie. De polystyreendeeltjes van 0.25, 0.5 en 1 μm stromen redelijk makkelijk het 2 μm kanaal van de WBNR in. Een 10% (v/v) suspensie van 0.25 μm deeltjes veroorzaakt ophoping bij de ingang van het 0.5 μm kanaal van de SMNR. Dit komt door de aanwezigheid van pilaren en holtes langs het kanaal. De pilaren verhogen de stijfheid van het kanaal en verminderen opbolling wanneer gas wordt toegelaten. De pilaren verhinderen vrije stroming van de suspensie. De kleine holtes in de wand van het kanaal zijn gevormd gedurende het fabricageproces. Hier blijven polystyreendeeltjes in hangen. Het gebruik van een lagere concentratie (2% v/v) van de suspensie lost het probleem van ophoping bij de ingang op. De resultaten van de experimenten rond het laden hebben geleid tot een nieuwe generatie SMNR, met een kanaalhoogte van 4.5 μm. Dit maakt het laden van een suspensie makkelijker zonder de afbeeldingsscherpte te beïnvloeden omdat de pilaren in het kanaal de opbolling nog steeds flink reduceren.

De ex-situ, quasi in-situ en in-situ TEM technieken

TEM is een van de belangrijkste katalysatorkarakteriseringstechnieken. TEM wordt normaliter ex-situ gebruikt. Voor ex-situ TEM wordt de katalytische reactie buiten de TEM uitgevoerd, waarna een klein monster uit de reactor gehaald wordt om met TEM te worden bestudeerd. In Hoofdstuk 5 wordt het verwijderen van beschermende groepen rondom goud nanodeeltjes bestudeerd met deze methodiek. Goud nanodeeltjes worden gemaakt via een colloïdaal proces waarbij dodecylamine (DDA) gebruikt wordt als reducerend en beschermend molecuul. De katalysatornanodeeltjes worden dan via impregnatie op een Al_2O_3 drager gezet om Au-DDA/Al_2O_3 katalysatoren te verkrijgen. De beschermende moleculen blijken het best verwijderd te kunnen worden door 8 uur bij kamertemperatuur met ozon te behandelen. FTIR laat zien dat het DDA dan helemaal verdwenen is.

Hierbij sinteren de Au/Al_2O_3 deeltjes een klein beetje, maar ze behouden hun kristalliniteit. De stabiliteit van de nanodeeltjes wordt bestudeerd in twee katalytische reacties: CO oxidatie en benzyl alcohol oxidatie. De TEM opnames laten zien dat zowel de beschermde als de onbeschermde nanodeeltjes sinteren tijdens CO oxidatie bij hoge temperatuur. Maar de activiteit is gelijk voor beide katalysatoren omdat hun deeltjesgrootte hetzelfde is. Het voordeel van ex-situ TEM is dat het makkelijk uitvoerbaar is. Een nadeel is echter dat het monster alleen vóór en ná de reactie wordt bestudeerd, en dus geen informatie tijdens de katalytische reactie verkregen wordt. Voorts wordt het monster aan de lucht blootgesteld tijdens het transport naar de TEM, wat voor sommige gevoelige katalysatoren kan leiden tot veranderingen.

Quasi in-situ TEM kan dit probleem voorkomen. Net als bij ex-situ TEM wordt hierbij de katalytische reactie buiten de TEM uitgevoerd, waarna een monster wordt genomen om met TEM te bestuderen. Het verschil is dat het monster in een speciaal ontwikkelde transporthouder naar de TEM wordt vervoerd, waardoor contact met lucht voorkomen wordt. In Hoofdstuk 6 wordt de reductie van Pt/Al_2O_3 en Pd/Al_2O_3 katalysatoren bestudeerd met quasi in-situ TEM. Om toch het hele reductieproces te kunnen bestuderen worden de experimenten met stapsgewijze verwarming uitgevoerd. Na iedere stap wordt het monster uit de reactor gehaald en in de TEM bestudeerd met behulp van de speciale transporthouder. Een Quantifoil® geperforeerde koolstoffilm op een gouden TEM-gaasje met verschillende draaddichtheden zorgt er voor dat we hetzelfde gebied weer terug kunnen vinden. Hierdoor kunnen we één gebied en dus dezelfde nanodeeltjes volgen na de verschillende reductie stappen. De deeltjesgrootte van Pt in Pt/Al_2O_3 neemt toe nadat het bij kamertemperatuur aan H_2 is blootgesteld, en met toenemende reductietemperatuur. De deeltjesgrootte van Pd in Pd/Al_2O_3 neemt ook toe wanneer de temperatuur wordt verhoogd van kamertemperatuur tot 50 ^{o}C, maar bij hogere reductie temperatuur blijft de deeltjesgrootte gelijk. Een van de voordelen van deze methode is de mogelijkheid om veranderingen in de deeltjes te volgen, bijvoorbeeld tijdens katalysatoractivering. Het nadeel is dat deze methode erg tijdrovend is.

Hoofdstuk 7 laat zien dat in-situ TEM de nadelen van quasi in-situ TEM elimineert. Bij in-situ TEM wordt de katalytische reactie uitgevoerd binnenin de TEM in de nieuwste generatie SMNR die gekoppeld is aan een gas voedingssysteem en een massaspectrometer. Hierdoor kunnen we de katalysator tijdens reactie bekijken bij reactietemperatuur en tegelijkertijd de reactieproducten analyseren. Door de veranderingen in de benodigde voedingsspanning voor de Mo verwarmingsspiraal te analyseren wordt ook de reactiewarmte bepaald. De reactie die bestudeerd wordt is de oscillerende oxidatie van CO op Pt nanodeeltjes.

Verschillende experimenten zijn uitgevoerd om de veranderingen in de platinadeeltjes tijdens de reactie te bestuderen. De oscillaties in O_2 en CO gasmengels zijn bestudeerd tussen 386 en 456 ^oC. TEM opnames laten zien dat de deeltjes bij de ingang van de reactiezone een stabiele afgeronde vorm hadden, terwijl deeltjes bij de uitgang van de reactiezone afwisselend een meer afgeronde (Pt 211) en een meer gefacetteerde (Pt 111) vorm hadden. De mogelijke invloed van de elektronenbundel is onderzocht door de nanoreactor af te beelden bij constante temperatuur en verschillende intensiteiten van de elektronenbundel.

De oscillerende reactie wordt waargenomen onafhankelijk van blootstelling aan de elektronenbundel. Deze waarnemingen suggereren dat de veranderingen in vorm van de platina nanodeeltjes samenhangen met de oscillaties en ongevoelig zijn voor veranderingen in de intensiteit van de elektronenbundel. De relatie tussen de CO conversie en de vormverandering van de platinadeeltjes is ook bestudeerd. Als de CO conversie toeneemt is de vorm van de nanodeeltjes meer gefacetteerd, terwijl de vorm meer afgerond is als de CO conversie afneemt. Dit wijst erop dat de oscillerende reactie en de vormverandering van de platinadeeltjes met elkaar samenhangen.

Deze belangrijke resultaten verkregen met in-situ TEM demonstreren de kracht van de techniek om meer inzicht te verkrijgen in hoe katalytische processen verlopen.

List of publications

Publications related to this thesis

1. Vendelbo S. B., Elkjær C. F., Puspitasari I., Creemer J. F.. Dona P., Mele L., Morana B., Nelissen B. J., Roobol S., van Rijn R., Helveg S. and Kooyman P. J., Atomic-scale imaging of Pt and Pd nanoparticle catalysts during CO oxidation at 1 bar reaction conditions, *Micros. Microanal*. **20**, 1570-1571 (2014).
2. Vendelbo S. B., Elkjær C. F., Falsig H., Puspitasari I., Dona P., Mele L., Morana B., Nelissen B. J., van Rijn R., Creemer J. F., Helveg S. and Kooyman P. J., Vizualisation of oscillatory behaviour of Pt nanoparticles catalysing CO oxidation, *Nat. Mater*. **13**, 884-890, (2014).
3. Elkjaer, C. F., Vendelbo, S. B., Falsig, H., Puspitasari, I., Dona, P., Mele, L., Morana, B., vam Rijn, R., Nelissen, B. J., Creemer, J. F., Chorkendorff, I. B., Kooyman, P. J. and Helveg, S. Electron microscopy advances for studies of catalysis at atomic-resolution and at ambient pressure levels. *Micros. Microanal.,* **21** (Supplement S3), 419-420, (2015).

Poster presentations

1. Puspitasari, I and Kooyman, P. J., Noble metal catalyst reduction in hydrogen, a quasi in-situ TEM study, *XIth Netherlands Catalysis and Chemistry Conference: Noordwijkerhout* (2010, March 1 - 2010, March 3)
2. Puspitasari, I and Kooyman, P. J., Pd/γ-Al_2O_3 catalyst reduction in hydrogen, a quasi-in-situ TEM study, *XIIth Netherlands Catalysis and Chemistry Conference: Noordwijkerhout*, (2011, February 28 - 2011, March 2).
3. Puspitasari, I., Morana, B., Mele, L., Santagata, F., Vendelbo, S. B., Creemer, J. F. and Kooyman, P. J., Noble metal catalyst reduction in hydrogen, a quasi and in-situ TEM study. *2nd International symposium on advanced electron microscopy for catalysis and energy storage materials: Berlin, Germany* (2012, February 5 - 2012, February 8).
4. Puspitasari, I., Vendelbo, S. B., Morana, B., Mele, L., Santagata, F., Creemer, J. F. and Kooyman, P. J., In-situ TEM nanoreactor loading: a flow imaging study. *NVvM Materials Science Meeting: Eindhoven, The Netherlands* (2012, October 25 - 2012, October 25).

Acknowledgments

At the end of this thesis I would like to acknowledge all the people without whom this project would never have been possible. First of all, I would like to express my sincere thanks to my promotores, Prof. dr. F. Kapteijn, and Prof. dr. P.J. Kooyman, for their meticulous guidance and advice in my research. I will always be grateful for their patience, support and kindness during and after my stay at TU Delft.

My greatest thanks go to all staff and colleagues in the Catalysis Engineering team. Thank you to Els, Elly, Harry, Bart, Kevin, Willy and Oscar for their administrative and technical support. Also to Edwin Uytenbroek who became my laptop doctor until it “died” right after my PhD contract finished. Thank you to Prof. dr. ir. M. Makkee and Prof. dr. J. Gascon for allowing me to use their setups in the laboratory. Many thanks to our group members for their warm friendship, to Christa, Loli, Joana, Pedro, Jianrong, Chieh-Chao, Bandar, Ana Rita, Nathalie, Dirk, Jasper, Asun, Canan, Jana, Pablo, Sina, Vera, Abrar and many other group members. Special thanks to Emmanuel and Canan for your collaboration and assistance in the research on gold nanoparticles, to Dr. X. Xu for providing me some samples for quasi in-situ TEM experiments and to Dr. M. Rao (Malles) for useful discussions.

Throughout my research, I used the TEMs in the TU Delft HRTEM group under the supervision of Prof. dr. H. W. Zandbergen. Therefore I would like to send my greatest thanks to them. During my first year of research, I received trainings from Prof. dr. P.J. Kooyman, Valerie Butselaar and Dr. Ugo Lafont regarding TEM operation. After that, Dr. ir. F. Tichelaar, Tom, Vasili, Ulrike and Jouk have always been there to help me solving many problems in my experiments. I also enjoyed the discussions and warm friendship from the group members Maria, Bo, Ganesh, Sairam, Marijn, Qian and many more. I also would like to thanks Prof. dr. ir. J. Westerweel to allow me to use the fluorescence microscope in his laboratory.

My research is part of the 'Nano IMaging under Industrial Conditions' (NIMIC) project. Therefore I acknowledge NIMIC for the financial support with special thanks to Prof. dr. J. Frenken, Dr. B. Nelissen, Dr. S. Helveg, Dr. C. F. Elkjær, Dr. L. Mele and P. Dona. I highly appreciated the collaboration with Dr. B. Morana from TU Delft DIMES group under the supervision of Dr. J.F. Creemer. My greatest thanks go to Dr. S. Vendelbo, without whom I think I wouldn’t have been able to finish this project. His skills, work ethics and mature personality were very inspiring. All the NIMIC related travels, experiments and meetings have special memories for me. I still remember my first NIMIC meeting where I accidentally

made Fredrik's head bleed and my round trip from the Netherlands to Denmark for a one hour project meeting there.

My stay in Delft would have been sad and boring without my Indonesian community. Thanks to the Zaldi family, Ferdiansyah family, Habib family, Luis family, Rizli, Zayan, Puspa, Velly and Credo for brightening my days with chats, jokes and fun gatherings. Playing cards, movie dates and a trip to Spain are our sweet memories. I hope our Plurk family will last forever (maybe until our second generation). Special thanks to Mr. A. Purniawan family for their friendship and support to my family during our stay in Delft. We will never forget your love and care to my son. Until now, he always considers your daughters as his big sisters. Thank you to all PPI Delft and KMD members for their friendship.

I would like to mention especially some people who become my inspirations in life, both academically and personally. To Mas Archi and Mbak Siska, Kak Anton and Kak Jelli, Mbak Nanda, Boya and Baud, also Mbak Hayuda and Kak Adnan. Thank you for the encouragement, attention and support you gave me. I will always treasure our friendship. Special thanks to Ruth Lie for her help and friendship so I could settle down in Eindhoven easily. Also to Jet v.d. Toorn who patiently tried to fix my English. I hope this thesis pays my promise to you.

Last but not least, my greatest thanks go to my family. Thank you to my husband (Saputra) and son (Sena) for their infinite love, support and understanding. Despite many problems and disappointments I faced, they always gave the warmest kisses and hugs to ease my pain. Thank you to my (late) father, mother, brothers and sister. Also to my in-laws family, especially Mas Riyanto who helped me to design the thesis cover. In the couple of years in The Netherlands I missed many things in their life, but they never stopped to love, trust and support me from afar.

It has been a long, adventurous and complicated journey for me, but I am glad I finally reached this point. Along the way, I received many lessons and experiences from all the people I mentioned above. Sometimes I might have hurt and disappointed them also, but I hope it won't stain our relationship. I realise that without all of them I wouldn't be here and only God can repay their support and kindness. Thank you.

Eindhoven, 2016

Indra Puspitasari

About the Author

Indra Puspitasari (Pita) was born on November 22, 1981 at Blitar (East Java), Indonesia. She finished her high school from SMUN 1 Blitar in 1999. After that she went to Depok (West Java) to obtain bachelor degree in Science from University of Indonesia (UI). She was graduated in 2004. In 2006 she received research-based Master degree scholarship from Korea Institute of Science and Technology (KIST). Her project focused on the deposition of thin film solar cell using chemical deposition method. In August 2008, she started her PhD program under supervision of Prof. dr. F. Kapteijn and Prof. dr. P.J. Kooyman in the Catalysis Engineering group at Delft University of Technology (TU Delft).